

ONLINE SYSTEM IDENTIFICATION AND
CONTROL OF AN AUTONOMOUS
UNDERWATER VEHICLE

ENG YOU HONG

*(B. ENG.), (M.ENG.), Nanyang Technological University,
Singapore*

A THESIS SUBMITTED

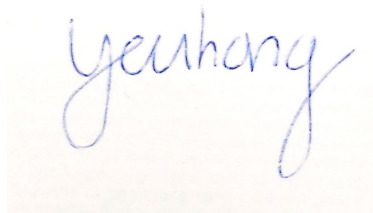
FOR THE DEGREE OF DOCTOR OF PHILOSOPHY
DEPARTMENT OF INDUSTRIAL & SYSTEMS
ENGINEERING
NATIONAL UNIVERSITY OF SINGAPORE

2015

DECLARATION

I hereby declare that this thesis is my original work and it has been written by me in its entirety. I have duly acknowledged all the sources of information which have been used in the thesis.

This thesis has also not been submitted for any degree in any university previously.

A handwritten signature in blue ink that reads "yeuhong". The signature is written in a cursive style with a large, looping 'y' and 'h'.

Eng You Hong
8 June 2015

Summary

More and more autonomous underwater vehicles (AUVs) are designed to be modular, where their payload configuration can be changed frequently depending on the mission requirements. When an AUV is reconfigured with different payloads, its dynamic characteristic is affected. Since the dynamic model underlies the design of its navigation, guidance and control systems, any deviation from the nominal model would potentially degrade the performance or in the worst case, cause critical safety issues.

In this thesis, an online method is developed to identify and validate the dynamics of a newly configured AUV. The AUV is programmed to perform a compact set of maneuvers where the vehicle's response is measured under known excitation. The method is composed of two stages. In the training stage, a State Variable Filter and Recursive Least Square (SVF-RLS) estimator is used to estimate the model parameters. In the validation stage, the prediction capability of the identified model is checked using a fresh data set. Compared to the conventional offline identification method, the SVF-RLS estimator is better in terms of prediction accuracy, computational cost, and training duration. We illustrate how the identified model can be used to estimate the turning radius of an AUV at different speeds and to design a gain-scheduled controller.

In order to meet the decoupling assumption, the roll angle of an AUV has to be kept small. To tackle this problem, we develop an internal rolling mass mechanism to actively stabilize the roll motion. We rotate a custom-made electronics tray, which has an off-centric center of gravity, to produce the required torque to stabilize the roll motion. The mechanical design of such a mechanism and its dynamic model and control are discussed in detail. The effectiveness of the mechanism in regulating the roll motion is shown in both tank tests and field experiments.

As the dynamic model is scheduled according to the vehicle's forward speed, the operating range of the speed need to be known. The minimum speed is

not zero, but a certain speed at which the AUV must travel for depth keeping. When the fins lose their effectiveness at low speed, the extra buoyancy will bring the AUV up to the surface. To understand the mechanism behind the occurrence of the minimum speed, we start by analyzing a nonlinear depth dynamic model of an AUV. First, we give formal definition to the minimum speed and then derive the solution together with its condition of existence. Through the solution, we gain insight on how the minimum speed of an AUV could be altered in practice. Next, a minimum speed seeking algorithm is developed under the framework of extremum seeking. We extend the framework by introducing a new definition of steady-state mapping which imposes a new structure on the seeking algorithm. The proposed algorithm employs a fuzzy inference system, which is driven by the real-time measurements of pitch error and elevator deflection. Finally, the effectiveness of the algorithm in seeking the minimum speed is validated in both simulations and field experiments.

Acknowledgements

This dissertation includes years of research on the STARFISH AUV, an in-house built autonomous underwater vehicle in the Acoustic Research Laboratory, Tropical Marine Science Institute, National University of Singapore.

First of all, I would like to thank my supervisor Dr. Ng Kien Ming for his time and effort in giving comments and suggestions to my research problems. He taught me to pay attention to the detail and also be rigorous in the scientific analysis. I would like to thank my ex-supervisor, Dr. Teo Kwong Meng who had challenged my existing thought constantly and requested me to think hard on my analysis. Through the numerous question and answer sessions, I learnt how to approach a problem and defend my own thinking.

A special thank goes to the principle investigator of the STARFISH project, Dr. Mandar Chitre, who also serves as my co-supervisor. Thank you for providing me with the opportunity to develop myself as a researcher in the environment of academic excellence, where he himself serves as a great role model.

I would also like to extend my gratitude to my current and past colleagues and friends at the ARL. I am grateful for the opportunity to work, surrounded by great individuals and for being part of an outstanding team.

Finally, my deepest gratitude goes to my family, especially to my wife, Shu Lien. This journey would not have been possible without her support and encouragement. I shall also mention my daughter, Yon Ning as she is always the source of joy and happiness.

Contents

List of Tables	iv
List of Figures	v
1 Introduction	1
1.1 Motivation	1
1.2 Objectives	5
1.3 Main Contributions	6
1.4 Research Platform: The STARFISH AUV	6
1.5 Organization	8
2 Literature Review	10
2.1 System Identification	10
2.2 Control Methodology	12
2.2.1 Robust Control	12
2.2.2 Adaptive Control	14
2.2.3 Intelligent Control	14
2.3 Roll Control	15
2.4 Moving Mass Mechanism	16
2.5 Minimum Speed Seeking Control	17
3 Online System Identification and its Applications	19
3.1 Modeling of Yaw Dynamics	20
3.2 Identification Method	23
3.2.1 Problem Formulation	23
3.2.2 State Variable Filter	24
3.2.3 Recursive Least Square (RLS)	27
3.2.4 Validation Method	28
3.3 Field Experiments	29
3.3.1 Experimental Setup & Procedure	29
3.3.2 Experimental Results	32

CONTENTS

3.4	Comparison with Conventional Offline Method	36
3.5	Discussion	40
3.6	Applications	41
3.6.1	Turning Radius of AUV at Different Speeds	41
3.6.2	Gain-Scheduled Controller Design	46
3.7	Summary	49
4	Roll Control using an Internal Rolling Mass	51
4.1	Mechanical Design	52
4.1.1	Design Requirements	52
4.1.1.1	Space Constraint	53
4.1.1.2	Energy Consumption	53
4.1.1.3	Ease of Assembly	53
4.1.1.4	Effective change of CG	53
4.2	Modeling of Roll Dynamics	54
4.2.1	Hydrostatic Righting Moment	55
4.2.2	Rolling Drag	55
4.2.3	Rolling Added Mass	56
4.2.4	Propeller Induced Torque	56
4.3	System Identification	58
4.4	Controller Design	61
4.5	Result and Discussion	63
4.6	Summary	65
5	Minimum Speed Seeking Control	66
5.1	Dynamic Model - Dive Plane	67
5.1.1	Kinematics	68
5.1.2	Equations of motion	68
5.1.3	Maximum elevator deflection, δ_{\max}	70
5.1.4	Thruster model	72
5.1.5	Depth closed-loop system	73
5.2	Minimum Speed and its Characteristics	73
5.2.1	The minimum speed	74
5.2.2	Characteristic of losing pitch-controllability	85
5.3	Minimum Speed Seeking Algorithm	86
5.3.1	Extremum Seeking	86
5.3.2	Seeking Algorithm	90
5.3.2.1	Fuzzy inference system (FIS)	92
5.3.2.2	Filtering	96
5.4	Simulation Results	97
5.5	Experiment Results	103

CONTENTS

5.5.1	Lake Experiments	103
5.5.2	Open Sea Experiments	109
5.6	Discussion	114
5.6.1	Effect of δ_{\max}	114
5.6.2	Choice of input parameter: thrust or speed	115
5.7	Summary	116
6	Conclusions and Future Research	117
6.1	Conclusions	117
6.2	Future Research	120
A	Publications arising from this thesis	122
B	Online Identification Result for Pitch Dynamics	123
B.1	Pitch Dynamics	123
B.2	Identification Results and Discussion	126
B.2.1	Experimental Procedure	126
B.2.2	Identification Result	126
	References	131

List of Tables

1.1	Sensors	8
3.1	Parameters Identified Through the SVF-RLS Estimator at Five Different Thrust Settings with AUV Configuration: (Base + DVL + Side-Scan).	34
3.2	Parameters Identified Through the Conventional Offline Method at Five Different Thrust Settings with AUV Configuration: (Base + DVL + Side-Scan).	37
3.3	Turning Radius for AUV: A Case Study with AUV Configuration: (Base + DVL).	45
3.4	Parameters identified through the SVF-RLS estimator at different thrust settings with AUV configuration: (Base + DVL + TLA).	48
4.1	Model parameters	59
4.2	Open and Closed Loop Plants	63
4.3	Open and Closed Loop Performance	64
5.1	Simulation parameters	98
5.2	Summary of experiment results during steady state for different δ_{\max}	108
B.1	Parameters identified for Pitch dynamics at different thrust . .	128

List of Figures

1.1	STARFISH AUV equipped with DVL and LEDIF payload at the Pandan Reservoir.	7
1.2	The STARFISH AUV is highly modular in design which allows easy reconfiguration of vehicle's payloads according to mission requirement.	8
3.1	Reference frame of STARFISH AUV.	21
3.2	Data flow in SVF-RLS estimator.	23
3.3	Input and Output of the SVF filter for $\lambda = 1$	27
3.4	Experimental run for identification of yaw dynamics at 100% thrust. Plot of roll, pitch, yaw and rudder.	30
3.5	Online parameter estimation of yaw dynamics at 100% thrust. Unknown parameters a_{22} , b_2 and C_0 have initial values of zero.	31
3.6	Experimental run for identification of yaw dynamics at 100% thrust. Plot of depth, x-y position, velocity and thrust settings.	32
3.7	Online parameter estimation of yaw dynamics for different thrusts.	33
3.8	Rudder control authority b_2 as a function of speed ²	35
3.9	Validation plots for experiments on five different thrust settings. Identified models are able to explain 78% to 92% of the yaw output variation.	35
3.10	Fitting of identified and measured yaw angle at 100% thrust for both online and offline methods.	38
3.11	Norm of the step change of the parameters Θ . All step changes are smaller than 0.001 after 12 s.	39
3.12	(a) Turning Radius R of an AUV traveling at speed, V and (b) Trapezoidal Profile for Yaw Angular velocity.	42
3.13	Turning radius of AUV at different speeds.	44
3.14	(a) Turning radius of AUV during the case study (b) Measured yaw rate and modeled yaw rate during the U-turn.	46
3.15	Block Diagram for Heading Control.	47

LIST OF FIGURES

3.16	Experimental results for heading control under constant gain controller and gain-scheduled controller.	49
4.1	Mechanical design of the Internal Rolling Mass (IRM) mechanism. Pictures on the right show the tail electronic tray which has a battery tray that attached to its bottom half.	52
4.2	(a) Coordinate Reference Frame (b) Free Body Diagram.	54
4.3	Propeller induced torque versus propeller revolution	57
4.4	Simulated and measured roll response under step input. The simulated roll response matched closely with the measured roll response despite small differences in amplitude and phase	60
4.5	Simulated and measured roll response under random input.	61
4.6	Root locus plot for compensated system.	62
4.7	Tank Test Result. The result shows that despite actuator saturation, the IRM mechanism manages to damp down the oscillation faster.	64
4.8	Field Experiment Result.	65
5.1	Free body diagram in dive-plane.	67
5.2	Typical lift coefficient versus fin deflection for NACA-0012 fin profile at Reynolds number 500 k. (Source: Airfoil tool generator at http://airfoiltools.com/airfoil/details?airfoil=n0012-il)	71
5.3	Relationship between thrust ratio T_R and thrust force F_t for Tecnydyne Model 520 underwater thruster.	72
5.4	Depth Subsystem with dual closed-loop control: inner pitch control and outer depth control.	73
5.5	The maximum required pitch curve.	77
5.6	The achievable pitch curve.	78
5.7	The minimum speed. Minimum speed is found at the intersection of the required pitch curve and achievable pitch curve.	79
5.8	Non-existence of the minimum speed.	81
5.9	Effect of buoyancy on minimum speed.	83
5.10	Effect of meta-centric height on the minimum speed.	84
5.11	Effect of fin's effectiveness on the minimum speed.	84
5.12	Characteristic of losing pitch-controllability. From 40 s onwards, the pitch response deviated from the desired pitch and the elevator became saturated.	85
5.13	Input-output system with a steady state map.	87
5.14	Readout map for $g(T_R)$. The <i>readout</i> map is not well defined for inputs less than T_R^*	88

LIST OF FIGURES

5.15	Readout map for $\dot{g}(T_R)$. A change in the definition of $g(\cdot)$ results in a well defined <i>readout</i> map.	89
5.16	Problem formulation. The block diagram shows the interaction between the AUV Depth Subsystem and Minimum Speed Seeking Subsystem. The minimum speed seeking subsystem sends thrust command to the AUV depth subsystem and receives pitch error θ_e and elevator deflection δ_s in return.	91
5.17	Block diagram of seeking loop. Fuzzy Inference System determines whether to maintain, decrease or increase T_R by a constant step gain Δ_T based on two inputs, θ_e and δ_s at every seeking interval.	91
5.18	Fuzzy Rules and the <i>readout</i> map.	94
5.19	Membership functions of the two inputs and one output. The membership functions of the two inputs, θ_e and δ are characterized by θ_e^{TS} and δ_{FB} respectively. We use triangular or trapezoidal shapes as the type of membership function because they are simple to implement and fast for computation	95
5.20	A snapshot of steady state elevator and pitch error when the AUV is operating under nominal thrust. This figure is the zoom-in of the first 10 s of Figure 5.12. The top figure shows the elevator operating within the range of 0.07-0.12 rad which leads to the assignment of $\delta_{FB} = 0.05$ rad. The bottom graph shows the corresponding pitch error which leads to the assignment of $\theta_e^{TS} = 0.01$ rad. The figure also shows how the filter smooths θ_e and removes the spikes in δ_s	96
5.21	Output surface map of the Fuzzy Inference System. The plot displays the dependency of the output Δ_T on the two inputs: pitch error θ_e , and elevator deflection δ	97
5.22	Simulated thrust ratio and speed.	99
5.23	Simulated elevator and pitch error and the corresponding FIS output.	100
5.24	Simulated pitch and depth responses.	101
5.25	Attainable minimum speed versus allocated fin budget.	101
5.26	Convergence of thrust ratio for different seeking periods T_s	102
5.27	Lake experiment: thrust ratio and speed.	104
5.28	Lake experiment: elevator and pitch error.	105
5.29	Lake experiment: pitch and depth responses.	106
5.30	Thrust and speed response for two repeated experiments with $\delta_{max} = 0.35$	107
5.31	Thrust and speed response for two repeated experiments with $\delta_{max} = 0.40$	108

LIST OF FIGURES

5.32	<i>STARFISH</i> AUV was towing a float during the open sea experiment. The picture was taken when the AUV was breaching the surface after completing a dive at 1.5 m depth.	109
5.33	Sea experiments: thrust ratio and speed.	110
5.34	Sea experiments: elevator and pitch error.	111
5.35	Sea experiments: pitch and depth responses.	112
5.36	Trajectory of the AUV. The AUV was facing west throughout the experiment.	112
5.37	Thrust and speed response for two repeated open sea experiments.	113
5.38	Thrust ratio and speed for different δ_{\max}	114
5.39	Effective fin angles δ_{se}	114
B.1	Experiment run for identification for pitch dynamics at thrust ratio 70%. Plot of depth, x-y position, velocity and thrust ratio	127
B.2	Experiment run for identification for pitch dynamics at thrust ratio 70%. Plot of roll, pitch, yaw and elevator	128
B.3	Online parameters estimation of pitch dynamics for different thrusts	129
B.4	Plot of elevator control authority d_2 against speed ²	129
B.5	Validation plots for experiments on five different thrust settings.	130

Chapter 1

Introduction

1.1 Motivation

The oceans cover 71% of the earth's surface and play an important role in the earth's climate and weather systems. However, many scientific investigations of the oceans are hindered by the lack of samples in both space and time. Unmanned underwater vehicle (UUV) is one of the emerging technologies that is believed to be able to change the landscape of the decade-long problem of under-sampled oceans [1].

There are two classes of UUVs: remotely operated vehicles (ROVs) and autonomous underwater vehicles (AUVs). ROVs are tethered vehicles with umbilical cables that transfer power, sensor data and control commands between the surface ship and the vehicles. They are tele-operated by human pilots and hence able to perform complicated tasks such as underwater structure installations and underwater sample collections. As they enjoy an unlimited power source from a surface ship, ROVs usually have an open-frame design and are equipped with multi-thrusters for greater maneuvering capability.

On the other hand, AUVs are *tether-less* vehicles and have to carry their own on-board energy source. Due to the limited energy supply, AUVs are usually designed to have a streamlined shape (torpedo-like) in order to reduce drag. They are often propelled by a single thruster and maneuver via the

1.1 Motivation

control of multiple fins. As the number of actuators is less than the degrees of freedom (DoF), AUVs are under-actuated. In contrast to ROVs, AUVs are more mobile and can be used to survey a large area in a shorter time frame. Hence, they are the main workhorses for oceanographic surveys, sampling and monitoring [2].

In order to perform any useful work, the AUVs must be able to follow an instructed trajectory or motion precisely. This capability relies on the dynamic control of the vehicle. The dynamic control of an underwater vehicle is difficult due to the following reasons:

- Hydrodynamic forces and moments are highly nonlinear and coupled between degrees of freedom.
- Unpredictable external disturbance such as wave and current.
- Time-varying model (hydrodynamic coefficients) which vary depending on the operating conditions.
- No access to fine-tune the controller gains during the autonomous cruise underwater.

Most of the AUV controllers are model-based. So its performance depends highly on the accuracy of the model parameters. Traditionally, those parameters are obtained through tow-tank experiments using a planar motion mechanism (PMM) or by employing computational fluid dynamics (CFD) analysis. Both methods are time-consuming and expensive to be carried out. In the current trend, AUV is designed to be modular where its payload configuration could be changed frequently depending on the mission requirement. So, it is practically infeasible to employ these two methods every time there is a change in the payload configuration.

The task of designing a controller is becoming more challenging when an AUV is reconfigurable with different payloads. Changing payload configuration affects the length, weight, shape of an AUV, and thus its dynamic characteristics. As the dynamic model underlies the design of its navigation, guidance and control systems, any deviation from its nominal model would

1.1 Motivation

potentially degrade its performance [3] or in the worst case, cause critical safety issues.

There are two approaches to tackle the uncertainty in the dynamic model of an AUV. The first approach is to design a controller that takes the uncertainty into consideration. The second approach is to reduce the uncertainty via system identification by conducting experiments on the AUV. Under the first approach, the problem has been widely studied by the control engineering community and the solution could be classified into robust control [4], adaptive control [5] and intelligent control [6]. Each of these control methodologies has their strengths and limitations, which we will discuss in detail in the literature review chapter. But, by and large, this approach focuses on the controller design to mitigate the negative effect of the uncertainty on the control performance.

In this thesis, we opt for the second approach, which aims to obtain the updated model via field experiments of the actual AUV. Before running an actual mission, the newly configured AUV is programmed to perform a compact set of maneuvers. The vehicle's response is then measured using the on-board sensors. Based on the vehicle's response under the known excitation, the unknown parameters of the dynamic model are determined. Such an approach, which allows the AUV dynamics to be identified, is called on-board system identification by Caccia *et al.* [7], or in-field identification by Mišković *et al.* [8].

The second approach is chosen because of a number of reasons. Firstly, when the updated model is obtained, it can be used not only for controller design, but also on the design of guidance law and the health monitoring of the AUV. For example, we could estimate the turning radius of the AUV under different operating speeds based on the model. The understanding of such performance limit enables us to plan the AUV path that is achievable in practice. The model could also be used to monitor the health status of the AUV, allowing early fault detection prior to running an actual mission [9]. Secondly, a simple controller design methodology, such as the linear control, can be employed because once the accurate dynamic model becomes available, the controller gains can be adjusted on-the-fly. Thirdly, there is nothing that

1.1 Motivation

stops us from employing a more advanced control techniques such as those developed in the first approach, and the resulting controller will perform better since the uncertainty in the model has been reduced.

Most of the on-board system identification methods reported for unmanned underwater vehicles are offline operated. The current state of the art of the system identification process requires inputs from a control engineer in data selection and solving of the unknown parameters via optimization [10]. Hence, in this thesis, we aim to develop an online method to automate the whole system identification procedures. By automating the process, we hope to save expensive ship-time and resources and also improve the system performance of the AUV.

In order for the system identification to work in practice, the structure of the dynamic model should be sufficiently simple such that the parameters of the model can be uniquely determined from the experimental data. Otherwise, one will suffer from the identifiability issue [11]. The dynamic model of a six degrees of freedom underwater vehicle, as described in [12] consists of more than a hundred unknown parameters. However, for a slender shape AUV, the dynamic model is usually divided into three subsystems (steering, diving and speed) by assuming the dynamics of different axes can be decoupled from one another [13, 14], and thus reducing the unknown parameters to a reasonable size. Furthermore, the dynamic model is a function of the vehicle's speed. We handle this non-linearity by adopting a multiple-model approach in which the model parameters are scheduled based on the vehicle's forward speed. In short, we use a simplified model based on the decoupling assumption, and the model parameters are a function of the vehicle's forward speed.

In order to meet the decoupling assumption, the roll angle of an AUV has to be kept close to zero [15], otherwise the dynamics between yaw and pitch will be coupled. In addition, it is desirable to keep the roll angle small without using the existing control fins. Because the control fins will be used during the open-loop identification, any overloading of the control fins with roll control task will complicate the identification result. To tackle this problem, we have proposed the use of an internal rolling mass (IRM) mechanism to actively stabilize the roll motion of an AUV. Such a mechanism is useful in

1.2 Objectives

stabilizing the AUV for underwater survey activities like bathymetry survey and side-scan imaging.

As the dynamic model is scheduled according to the vehicle's forward speed, the operating range of the speed needs to be known. The maximum speed is the speed when the maximum thrust is given, whereas the minimum speed is not zero, but a certain speed at which the AUV must travel for stable depth control. Otherwise, the extra buoyancy will bring the AUV up to the surface when the control fins lose their effectiveness at low speeds. Hence, in this thesis, we also develop an online algorithm such that the AUV is automatically controlled to travel at its minimum speed while maintaining a constant depth. Such capability is important in a number of practical scenarios, such as underwater loitering with minimum energy consumption, underwater docking with minimum impact, and high-resolution sensing at minimum speed.

1.2 Objectives

The objectives of this thesis can be summarized as follows:

- To develop an online system identification system that produces an updated dynamic model of an AUV, such that it can be used in the design of control, navigation and guidance system.
- To develop a solution that stabilizes the AUV's roll dynamics without using the control fins. This is to meet the decoupling assumption made in simplifying the dynamic model.
- To understand the mechanism behind the minimum speed, and to develop an online algorithm such that the AUV is automatically controlled to travel at its minimum speed while maintaining a constant depth. As the dynamic model is scheduled according to the vehicle forward speed, the minimum achievable speed needs to be known.

1.3 Main Contributions

The principal contributions of this dissertation are:

1. We have proposed an economic and feasible method to obtain a reasonably accurate dynamic model of an AUV via in-field experiments. Compared with the previous works, the proposed method allows identification to be done more rapidly. The identification results will be available immediately after the experiment run, and hence can be utilized in designing a controller and guidance law without human intervention. This results in considerable improvements in system performances and substantial saving in ship time.
2. We have tackled the unwanted roll motion of an AUV through active roll stabilization by using an internal rolling mass mechanism. We are the first to report the use of internal moving mass to stabilize the roll of an AUV. The mechanical design of such a mechanism and its dynamic modeling are discussed in detail. The effectiveness of the mechanism in regulating the roll motion of the AUV is demonstrated in tank tests and field experiments.
3. We have posted a new problem of minimum speed seeking for non-hovering AUV, which is of practical relevance to a number of operational scenarios. By analyzing the dynamic depth model of a typical AUV, we explain the mechanism behind the minimum speed and derive its solution together with its condition of existence. Then, a novel minimum speed seeking algorithm is proposed. Its performance was first studied in simulation and later validated in the lake and sea experiments.

1.4 Research Platform: The STARFISH AUV

The STARFISH AUV, our in-house build AUV, serves as an ideal platform for academic research. Similar to most of the AUVs, STARFISH is propelled

1.4 Research Platform: The STARFISH AUV



Figure 1.1: STARFISH AUV equipped with DVL and LEDIF payload at the Pandan Reservoir.

by a single thruster, use elevators and rudders as control surfaces, and is torpedo in shape. It is positive buoyant to facilitate easy recovery during the case of emergency. Its nominal speed is 1.5 m/s when operating at 70% thrust and its top speed is 2.4 m/s.

The STARFISH AUV is highly modular in design which allows easy reconfiguration of vehicle's payloads according to mission requirement. In Figure 1.1, the STARFISH AUV is equipped with LED induced fluorescence (LEDIF) payload for in-situ real-time optical sensing of the water chemistry and Doppler Velocity Log (DVL) payload for enhanced navigation capability. The mass of the vehicle is 65 kg and it is 2.3 m long with a diameter of 0.2 m. Currently, we also have Side-Scan payload, Voith Schneider Propeller (VSP) payload, and Thin-Line Array (TLA) payload in our lineup (see Figure 1.2). Depending on the payload configuration, we would expect changes in vehicle geometry and its dynamics.

The base STARFISH is equipped with a number of sensors. As far as this work is concern, we use a compass module for attitudes measurement, a pressure sensor for depth measurement, and a Doppler Velocity Log (DVL)

1.5 Organization



Figure 1.2: The STARFISH AUV is highly modular in design which allows easy reconfiguration of vehicle's payloads according to mission requirement.

for speed measurement. Their details are tabulated in Table 1.1.

Table 1.1: Sensors

Sensor	Measurement	Model	Manufacturer
Compass	Roll, Pitch & Yaw	HMR3500	Honeywell
Pressure	Depth	PDCR 1830	General Electric
DVL	Speed	Explorer	Teledyne

1.5 Organization

This dissertation is organized as follows. In Chapter 2, we survey the related previous works on our targeted areas of research. In Chapter 3, we develop a method to enable a rapid identification of AUV dynamics via on-board

1.5 Organization

system identification. First, we construct the yaw dynamics model of an AUV. Then, the online system identification and the experiment procedures are described in detail. Next, experimental results are presented. We compare the proposed method with the conventional offline method and finally, discuss two applications of the identified models.

In Chapter 4, we tackle the unwanted roll motion through active roll stabilization by using the IRM mechanism. First, we illustrate the mechanical design of the IRM mechanism followed by the dynamic modeling. Next, we present the results of system identification. Then, we show how a controller was designed to regulate the roll motion. Results from tank tests and open-field tests demonstrate the effectiveness of the mechanism in regulating the roll motion of the AUV.

Minimum speed seeking control is discussed in Chapter 5. We construct a depth dynamic model to explain the existence of the minimum speed, and show how it is affected by the extra buoyancy, righting moment and fin's effectiveness. Next, we design a minimum speed seeking algorithm that is driven by online measurement of pitch error and elevator deflection. The effectiveness of the algorithm in seeking the minimum speed was illustrated in simulations and experiments in both lake and sea.

Chapter 6, we conclude the important results in this thesis, pointing out potential future works.

Chapter 2

Literature Review

In this chapter, we review the current state of the art in five areas of AUV research. They are system identification, control methodology, roll control, moving mass mechanism, and minimum speed seeking control algorithm. By understanding the current state of the art of the respective areas, we hope to identify the gaps and potential areas that advancement can be made in knowledge and technology.

2.1 System Identification

Most of the AUV controllers are model-based. So their performance highly depends on the accuracy of the nominal model. Traditionally, parameters of a nominal model are obtained through tow-tank experiments using a planner motion mechanism (PMM) or by employing computational fluid dynamics (CFD) analysis. Both methods are time-consuming and expensive to carry out. In the current trend, the AUV is designed to be modular where its payload configuration can be changed rapidly depending on the mission requirements. So, it is practically infeasible to employ these two methods every time there is a change in the payload.

For a modular AUV, one would like to have an updated dynamic model after each change in payload configuration or vehicle geometry. One effective method to obtain the dynamic model is via field experiments of the actual

2.1 System Identification

AUV. Before running an actual mission, the AUV is programmed to perform a compact set of maneuvers. Vehicle response is then measured using on-board sensors. Based on the vehicle response under known excitation, the unknown parameters of the dynamic model are determined. Such an approach, which allows AUV dynamics to be identified more rapidly, is called on-board system identification by Caccia *et al.* [7], or in-field identification by Mišković *et al.* [8].

Most of the on-board system identification methods reported for unmanned underwater vehicles (UUVs) are offline operated and mostly applied to open-frame vehicles. Caccia *et al.* [7] identified a lump parameter model of an open-frame remotely operated underwater vehicle (ROV), using the least squares method and took into consideration the propeller-hull and propeller-propeller interaction effect. Ridaou *et al.* [16] compared two identification methods using the URIS UUV: one is based on the minimization of the acceleration prediction error, and the other, on the minimization of the velocity one-step prediction error. An online adaptive identification technique had been proposed by Smallwood and Whitcomb [17] for application in their ROV. For applications on streamlined AUVs, work had been done by Rentschler *et al.* [10] where parameter estimation was performed offline using an optimization technique. Tiano *et al.* [18] proposed to use an observer Kalman filter identification method to identify yaw dynamics of the Hammerhead AUV. Both simulation and experimental results were presented, but the online implementation of their algorithm was not discussed in detail. Recently, Petrich *et al.* [19] studied the identification of the pitch axis of Virginia Tech 475 AUV. They argued that the linear second order pitch model suffices for the attitude control design purpose. Offline result was presented.

From the literature review, we see that there is a need to develop an economical and feasible method such that a reasonably accurate dynamic model of the AUV could be obtained via field experiments. Compared with previous works, the proposed method should allow identification to be done more rapidly. The identification results are available immediately after each experimental run, and hence can be utilized in the design of the controller and guidance law without human intervention. This could result in considerable

2.2 Control Methodology

improvements in system performances and substantial savings in ship time.

However, performing an identification task in practice requires a human operator to make some important decisions that are highly dependent on one's experience, intuition, and insights. Since our aim is to automate the identification process, the main challenge would be on the development of a set of procedures which can replace human operator in the decision-making, and result in a consistent estimation of the parameters.

2.2 Control Methodology

What has been discussed so far is about system identification, and the focus is on obtaining an accurate model as much as possible. There is another aspect of the problem: the controller design. Controller designer usually assumes the model at hand is only a nominal plant which is subjected to uncertainty and other modeling errors. Several advanced control techniques have been developed for AUVs, with the main concern being on the robustness of the controller. Typical techniques include sliding mode control, nonlinear control, adaptive control, neural network based control and fuzzy control and also the combinations among them.

2.2.1 Robust Control

- Robust Linear control

Besides inherent nonlinearity of the AUV dynamics, previous works had shown some success in designing control laws based on linearized models [20, 21, 13, 19]. However, due to the difficulty of deriving an accurate model of an AUV system, most of the works were restricted to a particular operating condition. In order to operate in wider regimes, a gain-scheduled trajectory-tracking controller was proposed by Silvestre and Pascoal [22]. The time-invariant plant was obtained by linearizing the system dynamics about a finite number of representative points. Then, a linear controller was designed for each linearized plant. A family of linear controllers was generated by interpolating the parameters of

2.2 Control Methodology

the linear controllers designed previously. Interpolation was performed base on external scheduling variable (vehicle's forward speed). H- ∞ robust controller methodology was applied in designing each linear controller. This approach highlights the need for identification of the AUV dynamics at the different operating points, which is what we are pursuing in this thesis.

- Sliding mode control

Sliding mode control (SMC) has been widely used in the design of AUVs' controller [23, 24, 25, 14]. The main attractive property of SMC is its robustness against parameter uncertainties. By employing a high gain feedback at the switching surface, the controller restricts the system states to stay inside a designed subspace. The states converge asymptotically to the subspace even under the presence of model uncertainties, parameter variations, and disturbances. However, high gain feedback at the switching surface results in the chattering phenomenon, which is highly undesirable. It reduces the lifespan of the actuator by increasing the wear and tear. It also consumes more energy. There are a few remedies to the chattering problem. The most common remedy is by forming a boundary layer around the switching surface, such that the controller output is continuous[26]. Yoerger *et al.* [23, 27] introduced the basic methodology of using sliding mode control for an AUV application, and later Yoerger and Slotine [28] developed an adaptive sliding mode control scheme, in which a nonlinear system model was used. When the generalized disturbance makes the system state exceed the sliding mode tolerance layer, the exceeding value is used to update the nonlinear model parameters and the control input. Others have suggested the use of sliding modes with adaptivity, as in Cristi *et al.* [29] where the sliding surface is based on the system state rather than on the output error. The chattering problem could also be solved by having a better model that describes the plant more accurately. In this sense, the controller designer could select a smaller gain feedback at the switching surface and thus reducing the chattering effect. Online

2.2 Control Methodology

system identification is one way to obtain better dynamic model of the plant rapidly.

2.2.2 Adaptive Control

Adaptive control modifies the controller gains according to the changes in the process dynamics and the disturbances. Since there are parameter uncertainties in the hydrodynamic coefficients, many researchers use adaptive control to address the AUV control issues. However, adaptive control may fail when the dynamics changes faster than the adapting capability. Cristi *et al.* [29] proposed a model-based adaptive controller. Assuming that the vehicle dynamics is linear within the range of its operating conditions, the controller uses the RLS method for system parameter estimation and pole placement technique for controller design. Yuh [30] proposed a discrete-time adaptive controller using a parameter adaptation algorithm. Yuh and Nie [31] proposed a nonregressor-based adaptive control scheme that uses parametric bound estimation, instead of system parameter estimation, to tune the controller gains. For adaptive control, dynamic feedback loop is used for generating the estimates of unknown controller parameters for compensation [32]. Although adaptive laws are effective in the control of AUVs in the presence of large parameter uncertainties, their synthesis is complicated because a large number of control parameters must be adapted in the dynamic feedback loop. Moreover, adaptive systems are extremely sensitive to unmodeled dynamics [5].

2.2.3 Intelligent Control

Neural Networks and Fuzzy Logic belong to a family of techniques known as soft computing. Both methods can achieve nonlinear mapping from the system input space to the system output space. This makes them suitable for nonlinear system control. Neural Networks controller is constructed by training the layers of neurons with the experimental data. Fuzzy Logic controller is built based on the rule of thumb and the linguistic expression of an expert who understands the process well. Thus, both methods have the advantage that the dynamics of the control system need not be

2.3 Roll Control

completely known. The downside is no formal mathematical characterization exists for the closed-loop system behavior, and the validation of the final design can only be demonstrated experimentally. It is also hard to design the controller to meet certain requirements such as response time and stability. Related works using the Neural Networks controller for AUV control are [33, 30]; and for Fuzzy Logic controller [34, 35]. In Wang and Lee [36], authors discussed a combination of both methods for control of the ODIN AUV. The major drawback of intelligent control such as the neural network is the requirement of large training data set, and thus the training speed becomes the bottleneck of the motion controller design [37].

In this study, we do not focus on control methodology, as we will show in the coming chapter that when the system identification could give us a reasonably accurate model of the AUV dynamics, then a simple controller design methodology such as linear control could be employed to control the AUV.

2.3 Roll Control

As mentioned in the previous chapter, system identification requires a simple decoupled dynamic model to be used. The decoupling assumption is only valid when the AUV's roll is small. Furthermore, as the control fins are under open-loop control during the identification process, they could not be used concurrently for the roll regulation. From the literature survey, an unwanted roll motion is also a source of other problems.

The problem is becoming more prominent as AUVs are smaller nowadays. Smaller AUVs are built to reduce manufacturing costs and ease of deployment by one or two operators. Smaller AUVs pose constraints in placement of internal components and cause reduction in the metacentric height of the AUVs. This affects the inherent self-stabilization in the roll-axis. As a result, smaller AUVs are vulnerable to oscillatory roll motion.

A stable autonomous underwater vehicle (AUV) is essential for the underwater surveys such as the seafloor imaging using a side-scan sonar, bathymetric

2.4 Moving Mass Mechanism

mapping using a multi-beam sonar, and photo mosaicking using an underwater camera. As compared with yaw and pitch, the roll of a torpedo-shape AUV has a smaller moment of inertia and drag. So, the roll dynamics is oscillatory when the AUV is subjected to induced propeller torque, unknown disturbances and banking motion during turns. Without roll stabilization, the unwanted roll motion of an AUV can be problematic [38].

Singh, *et al.* [39], stated in their bathymetry paper, the roll bias is the most dominant error source as it directly affects the slope of the area being surveyed. Kirkwood, *et al.* [40] stated that the roll stability is critical to the multibeam mapping, and it is of high priority. For a side-scan sonar application, the AUV roll motion may cause layover to occur [41]; the affected samples are hard to interpret and need to be discarded. The unwanted roll motion can also affect both diving and steering performance of the AUV. This is because most feedback controllers are designed on the assumption that yaw and pitch motion are decoupled. When the roll of the AUV is non-zero, the assumption is violated and thus the performance of a decoupled controller will be affected [15].

2.4 Moving Mass Mechanism

In this thesis, we investigate the use of an internal rolling mass mechanism to actively stabilize the roll motion of an AUV. Internal actuators have a few appealing features. Firstly, they can be used at low speeds when the control fins lose their effectiveness. Secondly, they can be housed completely inside the vehicle and therefore are less prone to damage due to impact or corrosion [42]. Thirdly, they do not create external drag.

The use of an internal moving mass is not new in underwater vehicle applications. It has been used in underwater gliders such as SLOCUM, the Spray glider, and the Seaglider [43]. The use of internal moving mass is also found in some AUVs. One example is the hybrid AUV – eFolaga [44] where the battery is moved along the longitudinal axis to provide pitch control. However, the use of an internal mass for roll control is challenging because of the limited lateral space available for any significant linear motion.

2.5 Minimum Speed Seeking Control

Furthermore, the use of linear motion requires a runway for the moving mass which is practically infeasible as the internal space is already crowded with the essential components.

In summary, we foresee a large potential of such a mechanism in stabilizing the roll of an AUV despite the challenges of developing one in practice.

2.5 Minimum Speed Seeking Control

Non-hovering AUVs are controlled by fins, which lose their effectiveness at low speeds. Hence, there is a minimum speed at which the AUV must travel before losing its maneuvering capability. Traveling at low speeds is desired in a number of practical scenarios. An AUV consumes less energy when it travels slowly and hence maximizing its endurance. This contributes greatly to the long-term deployment of the AUV in environmental monitoring applications. The second scenario occurs when the AUV needs to perform underwater docking for battery charging and data transmission. In this case, the AUV should travel as slowly as possible so that the mechanical impact on the docking system is minimized. As pointed out by LeBas [45], traveling slowly also improves the final homing maneuver effectiveness. The third scenario happens when the AUV is required to conduct close observations of particular areas of interest, such as mines, coral reefs, and offshore installations. For example, in the case of sidescan sonar, the slower the AUV travels, the more scanlines can be acquired from the same target, which gives a higher image resolution.

The potential benefits of operating the AUV at low speeds have attracted a number of researchers. Liu et al. [46] improved the low speed maneuverability of the *Delphin* AUV by adding four thrusters to provide hovering capability to the AUV. In his master thesis, Helgason [47] examined ways to overcome the limitation that requires the *Gavia* AUV to cruise at speeds above 1.5 m/s. He focused on deriving the equation of motion for the AUV when external thrusters are attached to excite the respective DoF (surge, sway, heave and yaw). In [48], the authors investigated the use of a moving mass actuator to augment the existing fins to achieve a lower minimum speed. In the master

2.5 Minimum Speed Seeking Control

thesis of Lebas [45], a new robust controller was proposed to handle the change of the hydrodynamic characteristic when the speed is varied. Furthermore, a speed-dependent pitch limit was introduced so that the stall condition at low speed could be avoided.

In [49], the author derived the minimum speed based on the mass, the equilibrium angle of attack and some other hydrodynamic coefficients of the AUV. However, it is not easy to find the exact minimum speed as the hydrodynamic coefficients are not known to high accuracy. In fact, the minimum speed attainable by an AUV is also affected by its surroundings such as the water density and other disturbances. Therefore, an algorithm that automatically tracks the minimum speed in real-time is desirable. Adding thrusters or actuators might not always be a feasible option for existing AUVs, but implementing a minimum speed seeking algorithm is possible without any change in the hardware.

In the system identification process, we model the non-linearity of the dynamics by having the model parameters scheduled according to the vehicle speed. This motivates us to figure out the minimum speed of the AUV, without which our description of the dynamic model would not be complete. From the literature survey, it was understood that the ability to travel at the minimum speed has many practical advantages and an automatic algorithm that enables such behavior has not been developed. Hence, in this thesis, we aim to introduce a new behavior to the class of non-hovering AUVs: while the AUV maintains a certain depth and heading, its cruising speed is continuously regulated in real-time to its minimum.

Chapter 3

Online System Identification and its Applications

The dynamic characteristic of an autonomous underwater vehicle (AUV) is affected when it is reconfigured with different payloads. It is desirable to have an updated model, such that the control and guidance law can be redesigned to obtain better performance. We have developed an economical and feasible method to obtain a reasonably accurate dynamic model of the AUV via in-field experiments. Compared with previous works, the proposed method allows identification to be done more rapidly. The identification results are available immediately after each experimental run, and hence can be utilized in the design of the controller and guidance law without human intervention. This results in considerable improvements in system performances and substantial savings in ship-time.

The identification process has two stages. In the training stage, a State Variable Filter and Recursive Least Square (SVF-RLS) estimator is used to estimate the unknown parameters. In the validation stage, the prediction capability of the model is checked using a fresh data set. The parameters converged within 12 s in the experiments using five different thrusts. Validation results show that the identified models can explain 78% to 92% of the output variation. Next, we compare the SVF-RLS estimator with the conventional offline identification method. The comparison shows that the

3.1 Modeling of Yaw Dynamics

SVF-RLS estimator is better in terms of prediction accuracy, computational cost and training time. The usefulness of the identified models is highlighted in two applications. We use it to estimate the turning radius of the AUV at different speeds and to design a gain-scheduled controller.

3.1 Modeling of Yaw Dynamics

Generally, the motion of an AUV can be described using six degrees of freedom differential equations of motion [20]. These equations are developed using two coordinate frames shown in Fig. 3.1. Six positions and attitudes components $[x, y, z, \phi, \theta, \psi]$ (surge, sway, heave, roll, pitch, yaw) are defined in the earth-fixed frame, while the corresponding velocity and angular rate components $[u, v, w, p, q, r]$ are defined in the body-fixed frame.

When designing a controller for the AUV, we follow the conventional control philosophy which divides the AUV into three subsystems [13]. They are the:

1. steering subsystem, which controls the heading by using the rudder;
2. diving subsystem, which controls the depth and pitch by using the elevator;
3. speed subsystem, which controls the vehicle speed by varying the propeller speed.

The divide-and-conquer methodology works well in practice for streamlined AUVs when the coupling between subsystems is weak.

From [13], the yaw dynamics has the following state-space representation using state variables $v(t)$, $r(t)$, $\psi(t)$:

$$\begin{bmatrix} \dot{v} \\ \dot{r} \\ \dot{\psi} \end{bmatrix} = \begin{bmatrix} a_{11} & a_{12} & 0 \\ a_{21} & a_{22} & 0 \\ 0 & 1 & 0 \end{bmatrix} \begin{bmatrix} v \\ r \\ \psi \end{bmatrix} + \begin{bmatrix} b_1 \\ b_2 \\ 0 \end{bmatrix} \delta_r, \quad (3.1)$$

where a_{ij} and b_i are hydrodynamic coefficients, and δ_r is rudder deflection.

3.1 Modeling of Yaw Dynamics

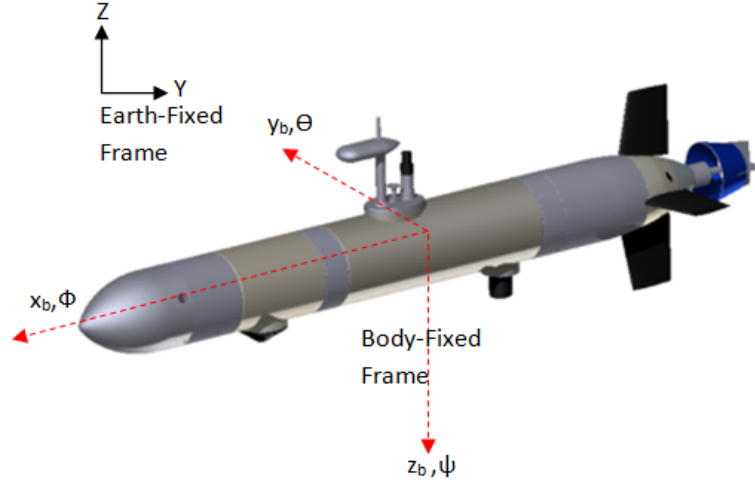


Figure 3.1: Reference frame of STARFISH AUV.

Specifically, yaw dynamics is described by the following equation:

$$\dot{r} = a_{21}v + a_{22}r + b_2\delta_r. \quad (3.2)$$

Sway velocity v is small during maneuvering of the AUV. This is due to the large body drag that resist any motion in the y -axis. So, the sway motion is considered to be insignificant and neglected from subsequent analysis. In addition, the coefficient a_{21} is also small for torpedo-shaped AUV since it is almost symmetrical in the y - z plane (bow and stern). Thus, the yaw dynamics can be further simplified to:

$$\dot{\psi} = r, \quad (3.3)$$

$$\dot{r} = a_{22}r + b_2\delta_r. \quad (3.4)$$

We extend the model by adding an extra term, called the steady state rudder deflection δ_0 as shown below:

$$\dot{\psi} = r, \quad (3.5)$$

$$\dot{r} = a_{22}r + b_2(\delta_r - \delta_0). \quad (3.6)$$

In particular, δ_0 is the rudder deflection when the yaw angle is constant.

3.1 Modeling of Yaw Dynamics

Under normal condition, δ_0 should be equal to zero. However, it can be non-zero under the following circumstances.

1. When there is some misalignment between the rudder zero position and vehicle vertical plane. This misalignment can be due to calibration error or accidental impact on the rudder.
2. When there is strong cross-current. In this case, sway velocity v is not small, such that δ_0 will capture the ignored term a_{21} in (3.1).
3. When there is asymmetry in x - z plane (port and starboard) of the AUV. The asymmetry causes higher drag on one side of the AUV, resulting in a yaw moment that needs to be compensated by rudder deflection.

Rewriting (3.6), we have linear-in-parameters model with three unknowns:

$$\dot{r} = \begin{bmatrix} r & \delta_r & -1 \end{bmatrix} \begin{bmatrix} a_{22} \\ b_2 \\ C_0 \end{bmatrix} \quad (3.7)$$

where $C_0 = b_2\delta_0$.

The three unknown parameters are: rotational drag coefficient a_{22} , rudder control authority b_2 , and steady state rudder deflection δ_0 . For easy reference, hereafter, we denote the unknown parameters as the following parameter vector

$$\Theta = [a_{22}, b_2, C_0]^\top. \quad (3.8)$$

Applying Laplace Transform and a change of variable to (3.6), we have:

$$\frac{\Psi(s)}{\Delta'(s)} = \frac{b_2}{s^2 - a_{22}s}, \quad \Psi(s) = \mathcal{L}\{\psi(t)\}, \quad \Delta'(s) = \mathcal{L}\{\delta_r(t) - \delta_0\}. \quad (3.9)$$

We address the non-linearity of the AUV dynamics by approximating the nonlinear model via parameter scheduling technique. The AUV speed is used to characterize the scheduling: a local linear time-invariant (LTI) model (3.7) is identified at a particular speed, then several LTI models are identified across speeds of interest, resulting in a global model. In other words, for each

3.2 Identification Method

particular speed u , we have a set of three parameters:

$$\Theta_u = [a_{22}, b_2, C_0]^\top. \quad (3.10)$$

3.2 Identification Method

Fig. 3.2 gives an overview on how $\Theta(t_k)$ is generated at every sampling instant, t_k by feeding rudder deflection $\delta_r(t_k)$ and yaw measurement $\psi(t_k)$ into the SVF-RLS estimator. A state variable filter (SVF) is used to produce filtered signals, $\ddot{\psi}_f(t_k)$, $\dot{\psi}_f(t_k)$ and $\delta_f(t_k)$. The filtered signals are later used in a recursive least square (RLS) estimator to produce $\Theta(t_k)$.

3.2.1 Problem Formulation

Equation (3.7) can be written in the following form:

$$\frac{d^2\psi}{dt^2} - a_{22}\frac{d\psi}{dt} = b_2\delta_r(t) + C_0. \quad (3.11)$$

The equation describes a single-input, single-output, linear, time-invariant, continuous-time system having noise-free input $\delta_r(t)$ and output $\psi(t)$. The system is proper. It is assumed that the input and output signals are sampled at time instants $\{t_k\}_{k=1}^N$. The sampled input and output signals at instant k are denoted by $\delta_r(t_k)$ and $\psi(t_k)$ respectively.

The identification problem consists of using input/output discrete data $\{\delta_r(t_k); \psi(t_k)\}$, $k = 1 \dots N$, to determine the values of parameters a_{22} , b_2 , and C_0 while satisfying certain goodness-of-fit constraints between predicted data and measurement. N is the total number of samples available. Then Θ^\top

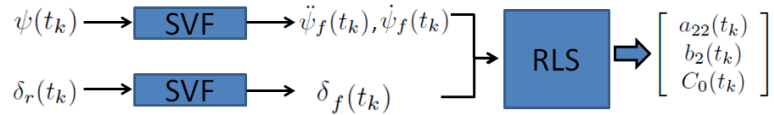


Figure 3.2: Data flow in SVF-RLS estimator.

3.2 Identification Method

could be solved as:

$$\begin{aligned} \arg \min_{\Theta^\top=[a_{22}, b_2, C_0]} J(\Theta) &= \sqrt{\frac{1}{N} \sum_{k=1}^{k=N} [\ddot{\psi}(t_k) - \Theta^\top \Phi(t_k)]^2} \\ \text{subject to} \quad a_{22}, b_2, C_0 &\in \mathfrak{R} \end{aligned} \quad (3.12)$$

where

$$\Phi(t_k) = [\dot{\psi}(t_k) \quad \delta_r(t_k) \quad -1]^\top. \quad (3.13)$$

For the cost function $J(\Theta)$ defined in (3.12), we have two time derivatives: $\ddot{\psi}(t_k)$ and $\dot{\psi}(t_k)$, which are not available from any instrument. We employ a state variable filter to reconstruct the two time derivatives from ψ . So, Θ^\top could be solved as:

$$\begin{aligned} \arg \min_{\Theta^\top=[a_{22}, b_2, C_0]} J(\Theta) &= \sqrt{\frac{1}{N} \sum_{k=1}^{k=N} [\ddot{\psi}_f(t_k) - \Theta^\top \Phi_f(t_k)]^2} \\ \text{subject to} \quad a_{22}, b_2, C_0 &\in \mathfrak{R} \end{aligned} \quad (3.14)$$

where

$$\Phi_f(t_k) = [\dot{\psi}_f(t_k) \quad \delta_f(t_k) \quad -1]^\top. \quad (3.15)$$

3.2.2 State Variable Filter

Reconstructing the time derivative from sampled data is an important step in direct continuous-time model identification. It is well known that numerical computation of the derivative via finite difference method is very sensitive to measurement noise. The problem is overcome by traditional SVF approach by passing both input/output signals through an all-pole filter $F(s)$ of minimum order n . It is preferable to choose $F(s)$ such that it has n similar poles [50]:

$$F(s) = \frac{\lambda^n}{(s + \lambda)^n}. \quad (3.16)$$

3.2 Identification Method

The numerator is chosen to be λ^n instead of 1 such that the filter has a unity dc gain. λ has to be chosen to match the bandwidth of the system dynamics. In particular, λ has to be chosen large enough, such that the filtered signal contains useful information of the dynamics, and small enough to filter out the measurement noise. According to [51], state variable filter serves as a pre-filter, and selection of λ allows one to emphasize certain frequency regions where model mismatch should be small.

Let

$$\boldsymbol{\psi}_{\mathbf{f}}(t) = \begin{bmatrix} \ddot{\psi}_{\mathbf{f}}(t) & \dot{\psi}_{\mathbf{f}}(t) & \psi_{\mathbf{f}}(t) \end{bmatrix}^{\top}. \quad (3.17)$$

$$(3.18)$$

Denote the Laplace transforms of $\psi(t)$ and $\delta_{\mathbf{r}}(t)$ as

$$\boldsymbol{\Psi}(s) = \mathcal{L}\{\psi(t)\}, \quad (3.19)$$

$$\boldsymbol{\Delta}(s) = \mathcal{L}\{\delta_{\mathbf{r}}(t)\}. \quad (3.20)$$

Then:

$$\begin{aligned} \boldsymbol{\Psi}_{\mathbf{f}}(s) &= \mathcal{L}\{\boldsymbol{\psi}_{\mathbf{f}}(t)\} \\ &= \frac{\lambda^2}{(s + \lambda)^2} \begin{bmatrix} s^2 & s & 1 \end{bmatrix}^{\top} \boldsymbol{\Psi}(s). \end{aligned} \quad (3.21)$$

$$\begin{aligned} \boldsymbol{\Delta}_{\mathbf{f}}(s) &= \mathcal{L}\{\delta_{\mathbf{f}}(t)\} \\ &= \frac{\lambda^2}{(s + \lambda)^2} \boldsymbol{\Delta}(s). \end{aligned} \quad (3.22)$$

Note that the above filters are causally implementable. Here, we give a specific example on numerical implementation of the filter. The implementation is adopted from [50]. To obtain time-derivative of order two, we need the following filter:

$$\mathbf{F}(\mathbf{s}) = \begin{bmatrix} \frac{\lambda^2 s^2}{(s+\lambda)^2} & \frac{\lambda^2 s}{(s+\lambda)^2} & \frac{\lambda^2}{(s+\lambda)^2} \end{bmatrix}^{\top}. \quad (3.23)$$

Let us denote the input signal to the filter as $w(t)$. The following state-space

3.2 Identification Method

equations written in controllable canonical form can be used to obtain the filter output:

$$\mathbf{y}(t) = \begin{bmatrix} w_f^{(2)} & w_f^{(1)} & w_f^{(0)} \end{bmatrix}^\top. \quad (3.24)$$

$$\mathbf{x}(t) = \begin{bmatrix} w_f^{(1)} & w_f^{(0)} \end{bmatrix}^\top. \quad (3.25)$$

where $w_f^{(2)}$, $w_f^{(1)}$ and $w_f^{(0)}$ are the second, first and zeroth derivative of the filter input $w(t)$ respectively:

$$\dot{\mathbf{x}}(t) = \mathbf{A}\mathbf{x}(t) + \mathbf{B}w(t), \quad (3.26)$$

$$\mathbf{y}(t) = \mathbf{C}\mathbf{x}(t) + \mathbf{D}w(t), \quad (3.27)$$

with

$$\mathbf{A} = \begin{bmatrix} -2\lambda & -\lambda^2 \\ 1 & 0 \end{bmatrix}, \mathbf{B} = \begin{bmatrix} 1 \\ 0 \end{bmatrix}, \quad (3.28)$$

$$\mathbf{C} = \lambda^2 \begin{bmatrix} -2\lambda & -\lambda^2 \\ 1 & 0 \\ 0 & 1 \end{bmatrix}, \mathbf{D} = \lambda^2 \begin{bmatrix} 1 \\ 0 \\ 0 \end{bmatrix}.$$

Under zero order hold (ZOH) assumption and with sampling interval, $h_k = t_{k+1} - t_k$, the above state-space can be discretized into:

$$\dot{\mathbf{x}}(t_{k+1}) = \mathbf{A}_d\mathbf{x}(t_k) + \mathbf{B}_d w(t_k), \quad (3.29)$$

$$\mathbf{y}(t_k) = \mathbf{C}_d\mathbf{x}(t_k) + \mathbf{D}_d w(t_k), \quad (3.30)$$

with

$$\mathbf{A}_d = e^{\mathbf{A}h_k}, \mathbf{B}_d = [e^{\mathbf{A}h_k} - \mathbf{I}] \mathbf{A}^{-1}\mathbf{B},$$

$$\mathbf{C}_d = \mathbf{C}, \mathbf{D}_d = \mathbf{D}. \quad (3.31)$$

Fig. 3.3 illustrates the experimentally measured yaw ψ and its corresponding filtered output for $\lambda = 1$.

3.2 Identification Method

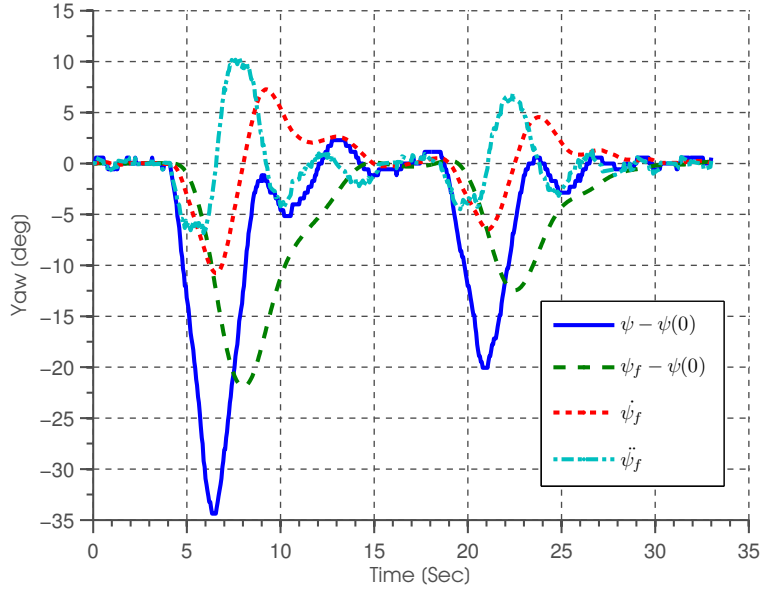


Figure 3.3: Input and Output of the SVF filter for $\lambda = 1$.

3.2.3 Recursive Least Square (RLS)

Parameters in the optimization problem of (3.14) can be identified experimentally using the standard least square method. Let N denote the total number of measurements available, and we define:

$$Q = \begin{bmatrix} \ddot{\psi}_f(t_1) & \ddot{\psi}_f(t_2) & \dots & \ddot{\psi}_f(t_N) \end{bmatrix}^\top, \quad (3.32)$$

and

$$\Phi = \begin{bmatrix} \dot{\psi}_f(t_1) & \delta_f(t_1) & -1 \\ \dot{\psi}_f(t_2) & \delta_f(t_2) & -1 \\ \vdots & \vdots & \vdots \\ \dot{\psi}_f(t_N) & \delta_f(t_N) & -1 \end{bmatrix}. \quad (3.33)$$

Thus if Φ is full rank, then the least square solution is given by the standard Moore-Penrose pseudoinverse:

$$\hat{\Theta} = (\Phi^\top \Phi)^{-1} \Phi^\top Q. \quad (3.34)$$

3.2 Identification Method

The idea behind RLS is to compute the parameters update $\hat{\Theta}(t)$ at each time instant t when measurements become available, by adding a correction term to the previous estimate $\hat{\Theta}(t-1)$. This saves a lot of computational effort as compared to the use of (3.34) with the entire measurement. It reduces the computational complexity from $O(N^3)$ to $O(N^2)$. For time-invariant system, the system parameters Θ are constant.

A typical RLS algorithm consists of the following recursive equations [52]:

$$\begin{aligned}\hat{\Theta}(t_k) &= \hat{\Theta}(t_{k-1}) + K(t_k)\epsilon(t_k), \\ \epsilon(t_k) &= \ddot{\psi}_f(t_k) - \hat{\Theta}^\top(t_{k-1})\Phi_f(t_k), \\ K(t_k) &= \frac{P(t_{k-1})\Phi_f(t_k)}{1 + \Phi_f^\top(t_k)P(t_{k-1})\Phi_f(t_k)}, \\ P(t_k) &= [1 - K^\top(t_k)\Phi_f(t_k)]P(t_{k-1}).\end{aligned}$$

The algorithm requires an initial guess of $\Theta(t)$ and the error covariance matrix P . The initial guess of $\Theta(t)$ is the zero vector and P is $100\mathbf{I}_3$, where \mathbf{I}_3 is the identity matrix of dimension 3.

3.2.4 Validation Method

Model validation is one of the important steps in any identification process. One needs to be assured that the identified model is an accurate representation of the system. One commonly seen method is to perform identification (training) on all the repeated experiments and then compare the identified parameters for consistency. In our opinion, this is not a test on the validity of the model, but rather a test on the repeatability of the experiment. In order to test the predictability of the model, one needs to test the model on fresh or untrained data set. As pointed out by [53, pg. 500],

It is not so surprising that a model will be able to reproduce the training data. The real test is whether it will be capable of also describing fresh data sets from the process.

The experiments are designed to collect two different data sets: *training data* are the data that would be used to estimate unknown parameters; *validation*

3.3 Field Experiments

data are fresh data that have not been used for parameter estimation. Using the validation data, simulated yaw responses, ψ_{sim} are generated by feeding the real rudder inputs into the identified model. Then it is possible to know how well the identified model can predict the measured yaw responses ψ_{real} by comparing ψ_{sim} to ψ_{real} . The goodness-of-fit between the two is measured using the coefficient of determination, R^2 , defined as:

$$R^2 = 1 - \frac{J_k}{\text{Var}(\psi_{\text{real}})} \quad (3.35)$$

where

$$J_k = \frac{1}{n} \sum_{i=1}^n (\psi_{\text{sim}} - \psi_{\text{real}})^2 \quad (3.36)$$

and

$$\text{Var}(\psi_{\text{real}}) = \frac{1}{n} \sum_{i=1}^n (\psi_{\text{real}} - \bar{\psi}_{\text{real}})^2. \quad (3.37)$$

Basically, R^2 indicates what fraction of the variance of the experiment data is explained by the simulated response. An R^2 value of 1 means a perfect fit and the model has captured 100% of the output variation.

3.3 Field Experiments

3.3.1 Experimental Setup & Procedure

After changing the payload, the newly configured AUV needs to be trimmed for buoyancy, static pitch and roll angle. This is normally done by resting the AUV in a water tank. Then, the AUV is trimmed to have 7 N positive buoyancy¹ and static pitch and roll angle around zero by adding or changing the weight distribution of the vehicle. The purpose is to configure the AUV to a default state, so that an initial conservative controller is capable of controlling it to the operating condition where identification can be carried out. Such an initial controller is not difficult to find heuristically, as pointed out by Rentschler *et al.* [10].

¹It is the buoyancy required to keep the AUV communication tower above water surface.

3.3 Field Experiments

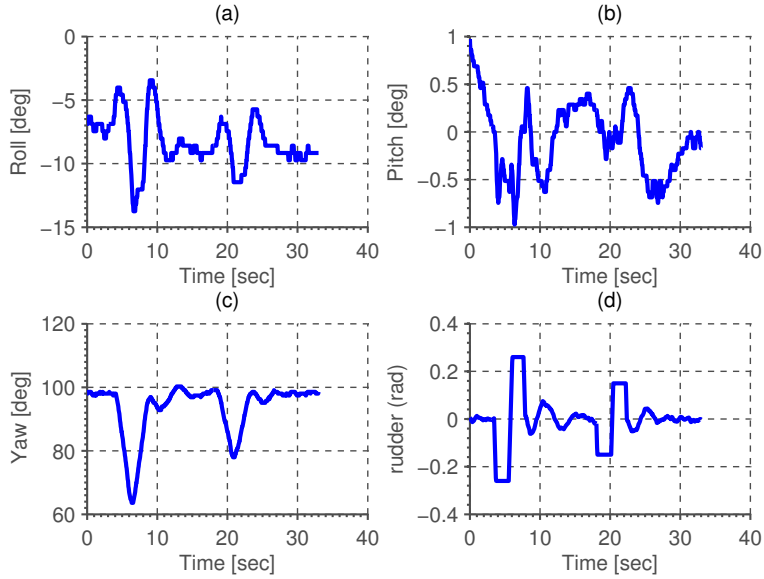


Figure 3.4: Experimental run for identification of yaw dynamics at 100% thrust. Plot of roll, pitch, yaw and rudder.

In the following, we will discuss different stages executed by the AUV during a typical identification run. In stage 1, the AUV is commanded to perform a straight run at a depth of 2 m with a constant thrust. It is allowed to settle down into the steady state (maintaining a constant heading, velocity and depth) within 40 s.

In stage 2 (training stage), the SVF-RLS estimator is turned on to start the estimation of the parameters. After 2 s, an excitation signal (doublet) of amplitude 0.26 rad for a period of 4 s is injected into the rudder deflection (Fig. 3.4d). The deflection generates a moment around the yaw axis and excites the yaw dynamics dramatically (Fig. 3.4c). After the excitation, the yaw controller is re-engaged to return the AUV to the desired heading. The SVF-RLS estimator is stopped after 10.5 s from the end of excitation. Stage 2 takes 16.5 s in total, with 330 data points processed at the rate of 20 Hz. The identification is only enabled during the resultant zig-zag maneuvering to fulfill the persistent excitation condition and to have a better signal-to-noise ratio (SNR). The unknown parameters, namely a_{22} , b_2 , C_0 are estimated on-the-fly at every sampling instant (Fig. 3.5). The unknown parameters would

3.3 Field Experiments

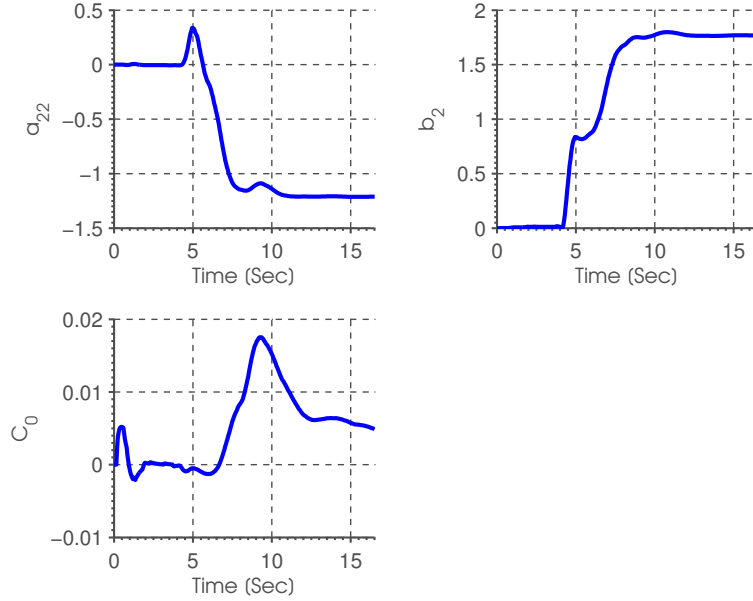


Figure 3.5: Online parameter estimation of yaw dynamics at 100% thrust. Unknown parameters a_{22} , b_2 and C_0 have initial values of zero.

converge and the last values are taken to be the final results. The results are then stored in the database for that particular thrust, and $\Theta(t)$ and $P(t)$ in RLS are reinitialized.

In stage 3 (validation stage), the second excitation signal (doublet) of amplitude² 0.15 rad for a period of 4 s is injected into the rudder deflection (Fig. 3.4d). It is important to point out that there is no parameter estimation in this stage. The whole purpose is to collect a fresh data set for cross-validation. We generate the simulated yaw response, ψ_{sim} by feeding the real rudder inputs into the model defined by the parameters estimated in stage 2. Stage 3 takes 16.5 s in total, with 330 data points recorded. Measured yaw responses, ψ_{real} , are recorded to calculate the coefficient of determination, R^2 , at the end of stage 3.

During the identification process, the depth (Fig. 3.6a) and pitch (Fig. 3.4b) are kept approximately constant, and the roll is small (Fig. 3.4a) to minimize

²Different amplitudes are used to excite the dynamics. We would like to test whether the dynamics remain the same under different excitation.

3.3 Field Experiments

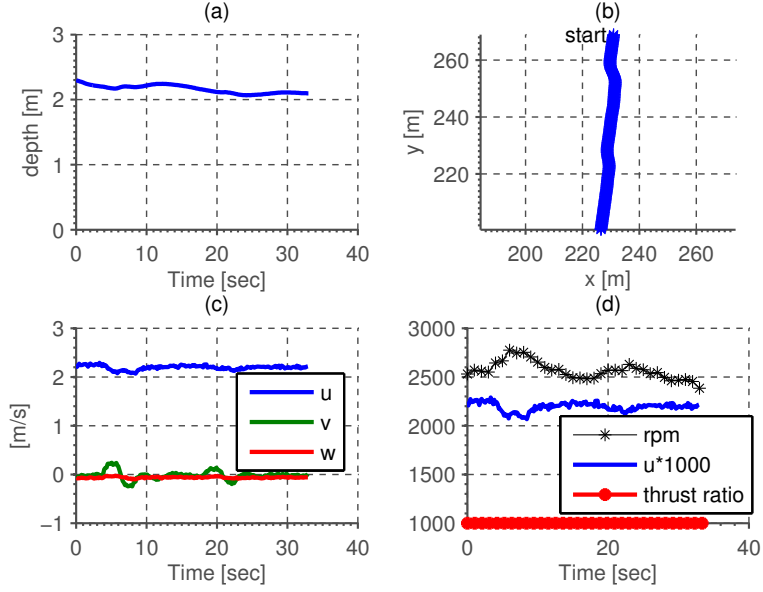


Figure 3.6: Experimental run for identification of yaw dynamics at 100% thrust. Plot of depth, x-y position, velocity and thrust settings.

the coupling effect. The AUV is moving in a straight path as shown in Fig. 3.6b except when the excitation signal is injected. The identification procedures are repeated for five different thrust values: 60%, 70%, 80%, 90% and 100% before the AUV is commanded to the pre-set home location.

3.3.2 Experimental Results

The results presented in this section were collected at Pandan Reservoir³, Singapore. The base STARFISH AUV is equipped with a DVL payload and a Side-Scan payload. Identification was done under five different thrust settings: ranging from 60% to 100%. Fig. 3.7 shows online parameter estimation of the three unknown parameters for five different thrust settings. For every thrust setting, all three parameters converged after about 12 s. The results are summarized in Table 3.1. The negative value of rotational drag coefficient a_{22} indicates that the yaw dynamics is inherently stable (poles are in the left-half plane). The a_{22} values have small variation around its mean value of

³Pandan Reservoir located in the western region of Singapore.

3.3 Field Experiments

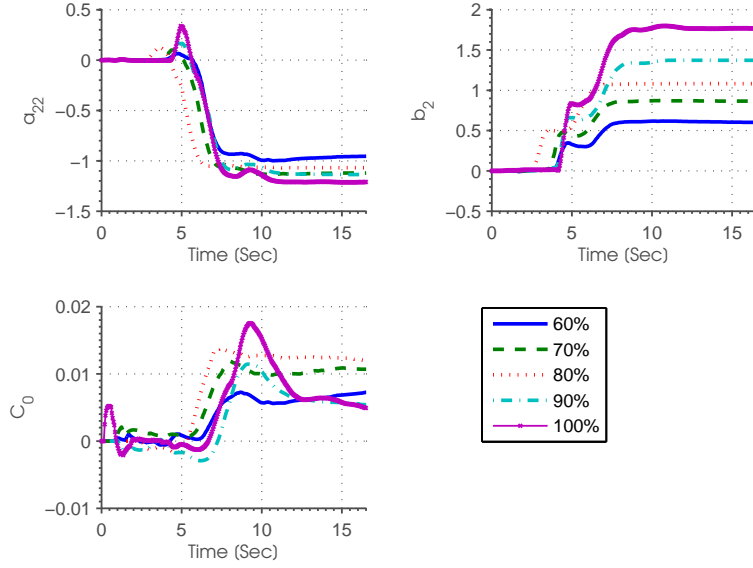


Figure 3.7: Online parameter estimation of yaw dynamics for different thrusts.

1.1 when thrust setting is varied.

The rudder control authority b_2 increases with speed due to higher dynamic pressure at the control surfaces. Theoretically, the gain b_2 should vary linearly with the square of speed, u^2 . This is verified in Fig. 3.8 which plots b_2 against u^2 . The positive value of b_2 indicates that a positive rudder input creates a positive moment in yaw and vice versa. The steady state rudder deflection δ_0 reduces with increase in speed. This is due to the increase of control authority which requires smaller fin deflection to overcome the same yaw disturbance. The value of δ_0 is almost zero. This indicates that there was no significant misalignment of fins. This corresponds with the fact that the rudder position was calibrated before the trial. In addition, there was no significant cross-current at the reservoir and the AUV is symmetrical in port and starboard.

From the last column of Table 3.1, it is observed that R^2 ranges from 0.780 to 0.916, which indicates that the models are able to explain 78% to 92% of the yaw output variation. The variation of R^2 values is expected as the experiments were conducted in unstructured real world environment,

3.3 Field Experiments

Table 3.1: Parameters Identified Through the SVF-RLS Estimator at Five Different Thrust Settings with AUV Configuration: (Base + DVL + Side-Scan).

Thrust (%)	Speed (m/s)	a_{22} (1/s)	b_2 (1/s ²)	C_0 (rad/s ²)	δ_0 (rad)	R^2
60	1.07	-0.95	0.60	0.0072	0.012	0.780
70	1.36	-1.12	0.87	0.0107	0.012	0.916
80	1.63	-1.07	1.08	0.0120	0.011	0.890
90	1.92	-1.14	1.37	0.0054	0.004	0.900
100	2.19	-1.21	1.77	0.0049	0.003	0.852

subjected to unknown disturbance and measurement noise. Nevertheless, the overall prediction capabilities are satisfactory as one can see in Fig. 3.9, which overlays both ψ_{real} and ψ_{sim} for thrust 60% to 100% and their corresponding R^2 values. The simulated response ψ_{sim} is able to describe the measured response very well for all thrust settings. From the results, we are convinced that the identified models have captured the dominant dynamic characteristic of the process.

Based on all experiments that we have conducted, the smallest R^2 obtained is 0.61, in which the corresponding identified parameters are still reasonably accurate. If the R^2 of an identification is less than 0.61, we consider it as an outlier and recommend one to repeat the experiment. In practice, the determination of this threshold is a trade off. Setting a high threshold gives us confidence in the accuracy of the parameters. However, it potentially causes one to repeat the identification unnecessary, as the parameters might be accurate, but have low R^2 due to measurement noise. On the other hand, setting the threshold too low might cause one to accept inaccurate parameters. So, we set the threshold to 0.61 to achieve balance between safeguarding of the estimation accuracy and avoiding unnecessary repetition.

3.3 Field Experiments

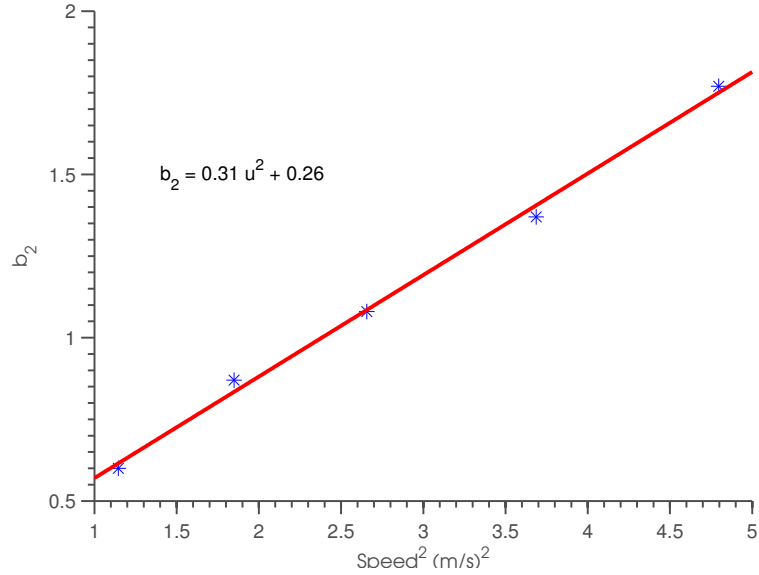


Figure 3.8: Rudder control authority b_2 as a function of speed².

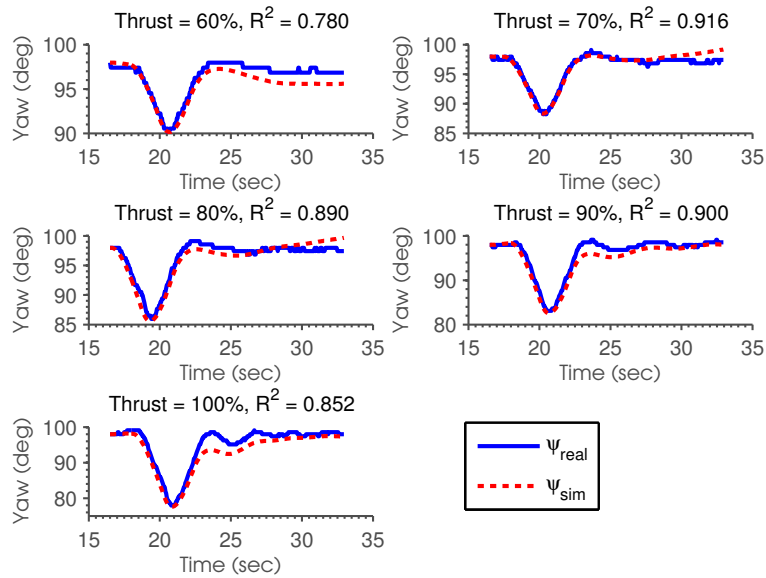


Figure 3.9: Validation plots for experiments on five different thrust settings. Identified models are able to explain 78% to 92% of the yaw output variation.

3.4 Comparison with Conventional Offline Method

From Section 3.3.2, we have validated the accuracy of the model identified by the SVF-RLS estimator based on R^2 values. However, it is interesting to study how the SVF-RLS estimator performs when compared to other identification methods. Here, we compare our online identification method against the conventional offline identification method that requires optimization via simulation.

The simulation takes in rudder input $\delta_r(t_k)$ along with the AUV initial states (yaw angle and yaw rate) and simulates the vehicle's response ψ_{sim} using (3.11), which is defined by an initial guess of Θ . At the end of every simulation, the following cost function is calculated:

$$J_{\text{offline}}(\Theta) = \sqrt{\frac{1}{N} \sum_{k=1}^{k=N} [\psi_{\text{real}}(t_k) - \psi_{\text{sim}}(t_k)]^2}. \quad (3.38)$$

It is important to note that the online identification is not the “online” version of the offline identification. They are two different methods employing two different objective functions. Online identification tries to minimize the error in term of yaw acceleration, whereas offline identification tries to minimize the error in term of yaw.

The optimization process searches iteratively for Θ that minimizes the cost function by repeating the simulation with different Θ . The optimization was conducted in Matlab/Simulink™ using the Parameters Estimation Toolbox in this study. The optimization method is a Simplex search [54]. The initial guess of the parameters Θ is the zero vector. There are two stopping criteria. The first criterion is to set the parameter tolerance to 0.01 as it is the accuracy of the parameters reported in this thesis. The second criterion is to set the function tolerance to 0.0001 to prevent the search algorithm from stopping prematurely.

The algorithm does not require the time derivative of the yaw. However, it is important to note that the simulation can only be run after the entire data

3.4 Comparison with Conventional Offline Method

set is collected. Hence, identification via simulation can only be executed offline. If the solution space is convex, the numerical optimization will produce an optimal Θ that minimizes the cost function for that particular set of training data. But, this optimality is generally not true for validation data which are not used in the optimization.

Table 3.2: Parameters Identified Through the Conventional Offline Method at Five Different Thrust Settings with AUV Configuration: (Base + DVL + Side-Scan).

Thrust (%)	a_{22} (1/s)	b_2 (1/s ²)	C_0 (rad/s ²)	δ_0 (rad)	R^2	Number Iteration
60	-0.98	0.61	0.0078	0.013	0.888	103
70	-1.20	0.88	0.0125	0.014	0.741	81
80	-1.19	1.12	0.0149	0.013	0.756	67
90	-1.32	1.48	0.0072	0.005	0.957	137
100	-1.42	1.85	0.0073	0.004	0.941	125

Table 3.2 reports the Θ obtained through the offline identification method. From Tables 3.1 and 3.2, the parameters are close to each other when comparing the coefficients. However, this is only a qualitative comparison. For quantitative comparison, we should compare the R^2 values produced by both methods. The R^2 for both methods are tabulated in the last column of Table 3.1 and Table 3.2 respectively. The offline identification method achieved on average an R^2 value of 0.857 whereas the online identification method achieved on average an R^2 value of 0.868. Hence, both methods achieve similar performance in terms of the accuracy of the prediction.

The difference in Θ estimation can be explained by the difference in cost functions used. The cost function for the offline method (3.38) is defined as the mean square error between the simulated yaw response and measured yaw response, whereas the cost function for the online method (3.14) is defined as the mean square error between the predicted yaw acceleration and measured yaw acceleration⁴. Fig. 3.10 overlays ψ_{sim} for both online and offline methods

⁴The measured yaw acceleration is generated from measured yaw via state variable filter.

3.4 Comparison with Conventional Offline Method

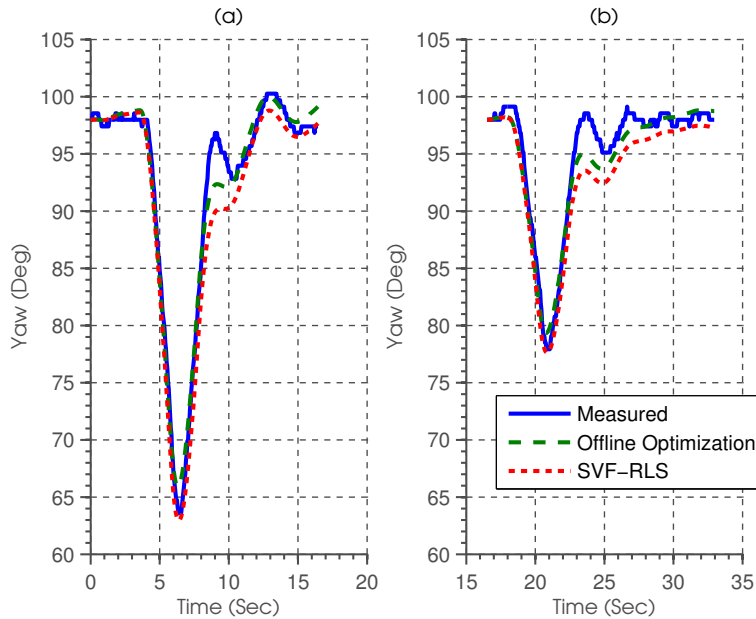


Figure 3.10: Fitting of identified and measured yaw angle at 100% thrust for both online and offline methods.

for training data and validation data respectively. The offline method achieved better overall fit but the online method had better fit when the AUV was turning. By the definition of the cost function, the online method puts more weight on the portion of data where the AUV experienced larger yaw acceleration. Since the interest is in the dynamic part of the yaw response, the online method produces better estimates in this aspect.

In terms of computational cost, the online method is much cheaper than the offline method. The offline method requires simulation of the whole data set at each search iteration. In each simulation run, the simulated yaw response ψ_{sim} is computed using the fourth-order Runge-Kutta ordinary differential equation (ODE) integrator. Table 3.2 shows that it took around 100 iterations on average for the parameters to converge.

Online identification allows one to monitor the convergence of the parameters on-the-fly. Some stopping criteria can be used to stop the parameter training once it is believed that the parameters have attained the desired accuracy. One such criterion is by monitoring the Euclidean norm of the

3.4 Comparison with Conventional Offline Method

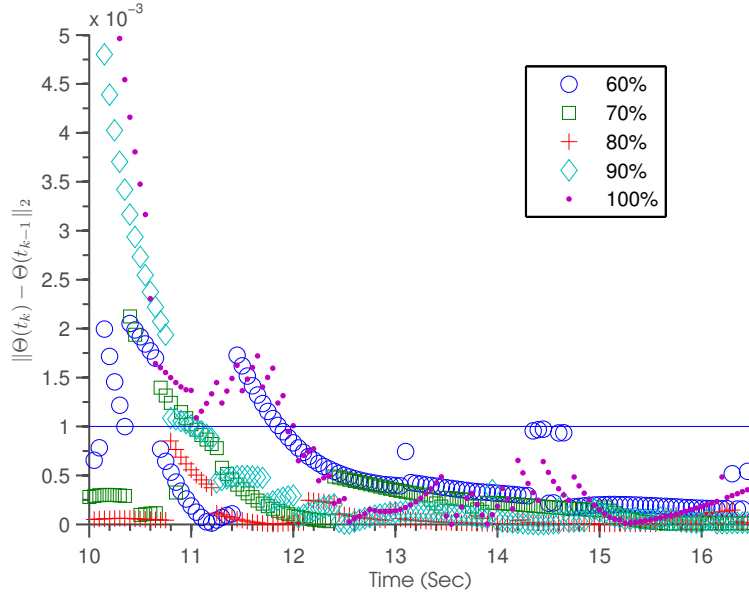


Figure 3.11: Norm of the step change of the parameters Θ . All step changes are smaller than 0.001 after 12 s.

change of the parameter estimate in every time instance to be less than a specific value, such as 0.001. In mathematical notations, the criterion is expressed as:

$$\|\Theta(t_k) - \Theta(t_{k-1})\|_2 < 0.001 \quad (3.39)$$

Fig. 3.11 shows that the criterion was first met from 12 s onward for all five thrust settings. In practice, the criterion should be met consecutively for a certain number of times before the training is stopped. This is to prevent the premature termination of the training. The ability to determine parameter convergence online allows training to be stopped early and hence saves valuable experiment time. As shown in Fig. 3.11, training could be stopped as early as 12 s instead of 16.5 s.

From the above discussions, we conclude that the online identification method compares favorably against the conventional offline method in terms of accuracy, computational cost and capability to stop training early.

3.5 Discussion

In the following, we discuss some key features of our proposed method:

- We address the non-linearity of the AUV dynamics by approximating the nonlinear model via parameter scheduling technique. The AUV speed is used to characterize the scheduling, where a local linear time-invariant (LTI) model is identified at each speed. Then, several LTI models are identified at speeds spanning the whole operating range, resulting in a global model.
- We construct the LTI model in continuous-time domain, instead of a discrete-time domain, as used in [18]. This preserves the physical meaning of the identified parameters, which turns out to be extremely useful in analysis and application. From the analysis perspective, it allows easy verification of the result by comparing it against our physical understanding of the AUV. From the application point of view, we could identify the model for two extreme speeds and obtain models for intermediate speeds via interpolation. The dynamic behavior of the AUV can be approximated beyond the identified range, assuming that the model can be extrapolated.
- While the state variable filter (SVF) and recursive least-square (RLS) estimator (SVF-RLS) approach to continuous-time model identification is well known [55], the application to AUVs and the experimental evaluation reported here are new. The proposed method is simpler to implement and requires fewer design parameters to be selected when compared to existing methods using adaptive identifier [17] and nonlinear observer [56].
- We validate the method through extensive field experiments on our in-house built STARFISH AUV [57]. Similar to many other available AUVs, the STARFISH AUV is torpedo in shape, has a single thruster and four control fins at the rear. The identification method requires limited instrumentation; in fact, it only requires a compass module,

3.6 Applications

which is a standard equipment among AUVs. Hence, we believe the proposed method is widely applicable.

- While only yaw dynamics is discussed here, the proposed method can be extended to pitch dynamics as well, as reported in [58]. Discussion of pitch dynamics is omitted here for simplicity and clarity.
- The proposed identification process has two main stages. Unknown model parameters are estimated in the training stage, and then validated in the validation stage. Prediction capability of the identified model is checked using a fresh validation data set instead of the old training data set. Such procedures, known as *cross-validation*, make sense without any probabilistic arguments and without any assumptions about the true system [53].

3.6 Applications

In this section, we discuss two applications of the identified model.

3.6.1 Turning Radius of AUV at Different Speeds

The yaw identification results can be used to estimate the turning radius of the AUV at different speeds. An understanding of the turning radius is especially important during maneuvering of the AUV for obstacle avoidance. It is also useful during path planning so that the achievable turning angle is taken into consideration (See Dubins curves in [59]).

We assume that the AUV has completed the yaw identification such that the information present in Table 3.1 is available. For each speed, we require information on travel speed V , control authority b_2 , and linear damping a_{22} . The rudder has a maximum deflection δ_{\max} of 0.26 rad to avoid stalling.

Fig. 3.12(a) illustrates an AUV making a U-turn with radius R . The perimeter of the half circle is πR . Let T_π denote the time taken to make a

3.6 Applications

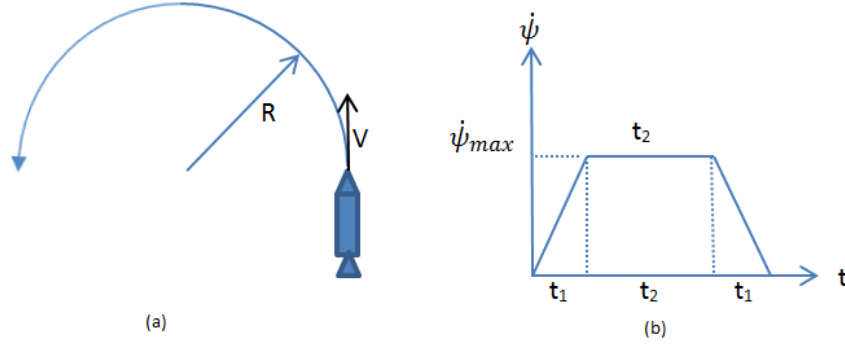


Figure 3.12: (a) Turning Radius R of an AUV traveling at speed, V and (b) Trapezoidal Profile for Yaw Angular velocity.

180 deg turn. Then, we have:

$$\pi R = VT_{\pi}. \quad (3.40)$$

Fig. 3.12(b) shows a trapezoidal profile for yaw angular velocity. In order to make a U-turn, the AUV will start turning from zero yaw angular velocity to critical yaw angular velocity, $\dot{\psi}_{max}$. The acceleration process takes t_1 s. Then, it maintains the turning rate at $\dot{\psi}_{max}$ for t_2 s before decelerating to zero. The deceleration process takes another t_1 s, and so

$$T_{\pi} = t_1 + t_2 + t_1. \quad (3.41)$$

The area under the curve is the total heading change of π rad. So,

$$\frac{1}{2}\dot{\psi}_{max}(t_2 + t_1 + t_2 + t_1) = \pi, \quad (3.42)$$

which gives

$$\dot{\psi}_{max}(t_2 + t_1) = \pi. \quad (3.43)$$

From (3.9), we know that the transfer function of yaw angular velocity to

3.6 Applications

rudder is a first-order system:

$$\frac{s\Psi(s)}{\Delta'(s)} = \frac{b_2}{s - a_{22}}. \quad (3.44)$$

Under the step input of rudder at magnitude $(\delta_{\max} - \delta_0)$, the step response is

$$C(s) = \frac{b_2}{s - a_{22}} \cdot \frac{\delta_{\max} - \delta_0}{s}. \quad (3.45)$$

Taking the inverse transform, the step response is given by

$$c(t) = \frac{b_2(\delta_{\max} - \delta_0)}{-a_{22}}(1 - e^{a_{22}t}). \quad (3.46)$$

By letting $t \rightarrow \infty$ in (3.46), $\dot{\psi}_{\max}$ is given by

$$\dot{\psi}_{\max} = \frac{b_2(\delta_{\max} - \delta_0)}{-a_{22}}. \quad (3.47)$$

The time t_1 is approximated by the time taken to reach 100% of the final value [60, pg. 180]:

$$t_1 = \frac{4}{-a_{22}}. \quad (3.48)$$

Substituting (3.43), (3.47) and (3.48) into (3.41), we have:

$$T_\pi = -\pi \left(\frac{a_{22}}{b_2(\delta_{\max} - \delta_0)} + \frac{4}{a_{22}\pi} \right), \quad (3.49)$$

and

$$R = -V \left(\frac{a_{22}}{b_2(\delta_{\max} - \delta_0)} + \frac{4}{a_{22}\pi} \right) = \frac{VT_\pi}{\pi}. \quad (3.50)$$

From Table 3.1, we assume that a_{22} stays constant at -1.1 . From Fig. 3.8, we have the following relationship between speed V and b_2 (sign of b_2 is dropped as the absolute value of b_2 is used):

$$b_2 = 0.31V^2 + 0.26. \quad (3.51)$$

3.6 Applications

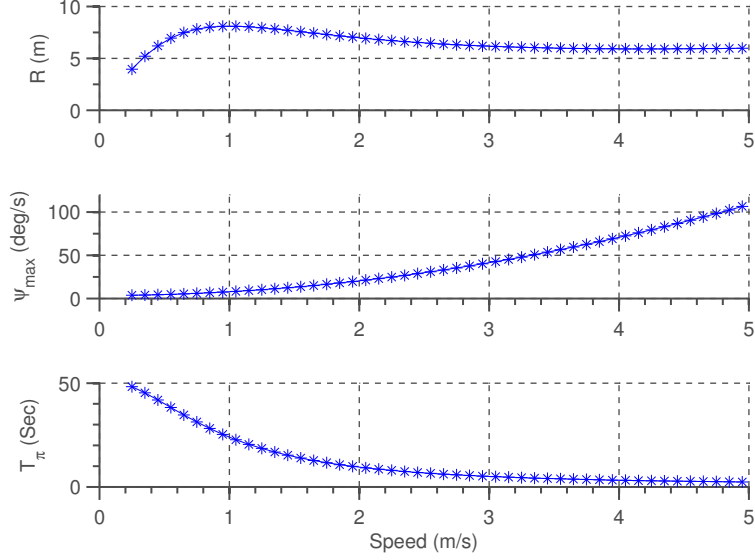


Figure 3.13: Turning radius of AUV at different speeds.

With $\delta_{\max} = 0.26$ rad and $\delta_0 = 0$, we have:

$$R = V \left(\frac{1.1}{(0.31V^2 + 0.26)(0.26)} + \frac{4}{(1.1)\pi} \right). \quad (3.52)$$

Similarly, we have $\dot{\psi}_{\max}$ and T_{π} as follows:

$$\dot{\psi}_{\max} = \frac{0.26(0.31V^2 + 0.26)}{1.1}, \quad (3.53)$$

$$T_{\pi} = \frac{1.1\pi}{0.26(0.31V^2 + 0.26)} + \frac{4}{1.1}. \quad (3.54)$$

Fig. 3.13 predicts how R , Ψ_{\max} and T_{π} change with speed. It is important to note that yaw identification was only performed for a speed range from 1 to 2.2 m/s but the plot shows the results for speeds from 0.5 to 5 m/s. The result is only valid if (3.51) and the assumption $a_{22} = -1.1$ holds also for speeds ranging from 0.5 to 5 m/s.

The critical yaw angular velocity $\dot{\psi}_{\max}$ increases with speed. From (3.47), $\dot{\psi}_{\max}$ is linearly proportional to b_2 , which in turn is linearly proportional to

3.6 Applications

Table 3.3: Turning Radius for AUV: A Case Study with AUV Configuration: (Base + DVL).

a_{22}	b_2	δ_0	$\dot{\psi}_{\max}$ (deg/s)	T_π (s)	R (m)
-1.62	1.25	0.04	9.90	20.65	9.20

the square of speed. As expected, the time taken to complete a U-turn, T_π , reduces with speed as the AUV turns at a faster rate.

The results show that in order to achieve a smaller turning radius, the AUV should travel at lower speeds. For example, at speed 0.25 m/s, the turning radius is 4 m. The trade-off is that it takes about 48 s to complete a U-turn. For the higher speed region, the minimum achievable turning radius is 5.9 m at a speed of 4.2⁵ m/s. The turning radius increases with speed after that. There is a minimum value for T_π despite an increase in speed. As $R \propto VT_\pi$, when V increases faster than the decrease in T_π , the turning radius will increase with speed.

A field experiment was carried out to compare the measured turning radius against the predicted turning radius. A base AUV with a Doppler Velocity Log (DVL) payload was used in this experiment. The AUV was commanded to a constant depth of 2 m. It was commanded to thrust at 70% with an average speed of 1.4 m/s. Yaw identification was executed to identify parameters a_{22} , b_2 and C_0 . Then the AUV was commanded to make a U-turn before returning to the surface. The turning radius of the AUV was found by fitting a circle on the x - y position plot as illustrated in Fig. 3.14(a). Table 3.3 shows the identified parameters and the predicted $\dot{\psi}_{\max}$, T_π and R . It is interesting to note that δ_0 is not equal to zero. In this case, the effective maximum rudder deflection δ_{\max} is $0.26 - 0.04 = 0.22$ rad. The predicted turning radius is 9.2 m which is close to the measured turning radius of 9.9 m. The prediction is accurate as a result of good modeling of the yaw rate⁶ as can be seen in Fig. 3.14(b).

⁵The STARFISH AUV design top speed is only about 2.5 m/s, so this speed is not achievable in practice.

⁶Measured yaw rate is derived from yaw measurement using Savitzky-Golay filter.

3.6 Applications

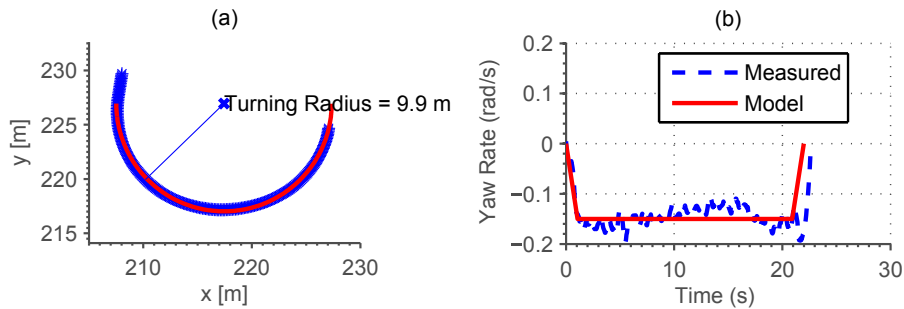


Figure 3.14: (a) Turning radius of AUV during the case study (b) Measured yaw rate and modeled yaw rate during the U-turn.

In this subsection, we have illustrated how the turning radius can be calculated from the identified parameters. By postulating that the model can be extrapolated, we study the turning radius of the AUV beyond the speed region where it was identified. The results indicate that the turning radius has a local minimum at the high speed region where we cannot reduce the turning radius by increasing the speed further. On the other hand, traveling slowly is the way to reduce the turning radius, but this is at the expense of longer turning time. Lastly, via a field experiment, we show that the turning radius can be predicted accurately based on the identified parameters.

3.6.2 Gain-Scheduled Controller Design

The main purpose of system identification is to reconfigure the controller according to the system dynamics. We next present some results on the steering control of the STARFISH AUV at different speeds. We would like to demonstrate the ease of controller synthesis after the parameters are obtained and highlight the performance improvements after reconfiguration.

Fig. 3.15 shows the block diagram of the steering control system. We close the loop using a simple proportional (P) controller with a feedforward term. There are two main problems in steering control at different speeds. The yaw dynamics changes with speed. One possible solution is to use robust control design methodology which results in selecting a constant gain, K_p that minimizes the norm of the closed-loop transfer function under

3.6 Applications

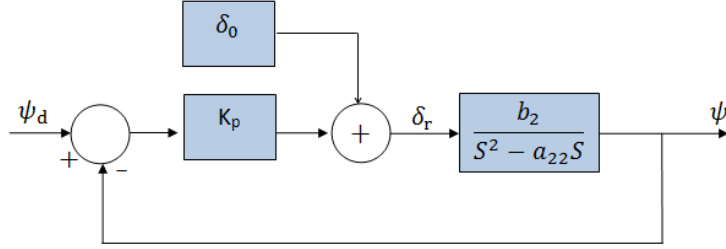


Figure 3.15: Block Diagram for Heading Control.

parametric uncertainty. However, a constant gain robust controller can be very conservative as compared to a gain-scheduled controller that can adapt itself to the change in system dynamics. Another problem in steering control is the steady state error caused by non-zero rudder offset. We handle the problem by feed-forwarding δ_0 to neutralize the offset.

From the block diagram, the closed-loop transfer function from the desired yaw ψ_d to yaw output ψ is:

$$\frac{\psi_d(s)}{\psi(s)} = \frac{K_p b_2}{s^2 - a_{22}s + K_p b_2}. \quad (3.55)$$

The closed-loop poles are:

$$p_{1,2} = \frac{a_{22}}{2} \pm \frac{\sqrt{a_{22}^2 - 4K_p b_2}}{2}. \quad (3.56)$$

We select gain K_p such that the closed-loop poles lie in the line of constant damping ratio ζ in the s -plane. For a second order system, the overshoot percentage is only a function of damping ratio. So, we choose ζ to be 0.7071 which is equivalent to approximately 5% overshoot. In the s -plane, constant damping ratio line of 0.7071 corresponds to the $y = -x$ line. Hence, we require:

$$-a_{22}^2 = a_{22}^2 - 4K_p b_2 \implies K_p = \frac{a_{22}^2}{2b_2}. \quad (3.57)$$

As shown in Table 3.4, a_{22} and b_2 which are functions of speed, were

3.6 Applications

Table 3.4: Parameters identified through the SVF-RLS estimator at different thrust settings with AUV configuration: (Base + DVL + TLA).

Thrust (%)	Speed (m/s)	a_{22} (1/s)	b_2 (1/s ²)	C_0 (rad/s ²)	δ_0 (rad)	R^2	K_p
60	1.05	-1.28	0.65	0.0129	0.016	0.614	1.26
70	1.32	-1.51	1.04	0.0169	0.020	0.977	1.09
80	1.60	-1.70	1.41	0.0274	0.019	0.973	1.02
80	1.60	-1.54	1.30	0.0273	0.021	0.848	0.91
90	1.87	-1.69	1.85	0.0163	0.009	0.911	0.77
100	2.13	-1.48	2.02	0.0312	0.016	0.911	0.54

identified prior to the design of the gain-scheduled controller. At different speeds, the gain K_p will be adjusted accordingly as tabulated in the last column of Table 3.4.

We repeated the identification experiment twice for 80% thrust to check the repeatability of the experiment. We observed a small difference in the estimation of the parameters; the first experiment estimated $\hat{\Theta}_1 = [-1.70, 1.41, 0.0274]$ and the second experiment estimated $\hat{\Theta}_2 = [-1.54, 1.30, 0.0273]$. We should set the gain, K_p to 1.02 if based on the $\hat{\Theta}_1$, and set the K_p to 0.91 if based on the $\hat{\Theta}_2$. Both experiments also give very close prediction on the turning radius (3.50), they are 9.20 m and 9.25 m for $\hat{\Theta}_1$ and $\hat{\Theta}_2$ respectively. Although there are some small variations in the identified parameters, which is expected due to measurement noise and disturbances, both $\hat{\Theta}$ give consistent suggestion on the controller gain K_p and the turning radius.

The experimental results obtained using the gain-scheduled controller with feedforward are shown in Fig. 3.16 with comparison to a constant gain controller. The AUV was first commanded to maintain a constant depth and heading. Then the AUV was commanded to turn ± 20 deg from the current heading while the thrust was increased from 60% to 100%. The constant gain controller performed satisfactorily at the lower speed as the constant gain was determined based on manual tuning when the AUV was operating at 60% thrust. In the higher speed region (90% and 100% thrust),

3.7 Summary

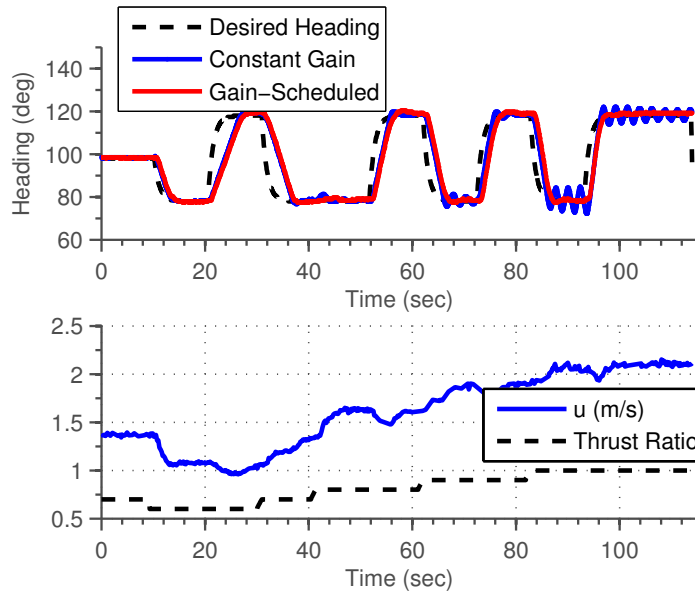


Figure 3.16: Experimental results for heading control under constant gain controller and gain-scheduled controller.

the heading response became oscillatory. In contrast, the gain-scheduled controller consistently performed well over the entire speed envelop.

3.7 Summary

In this chapter, we have developed a method to enable rapid identification of AUV dynamics via in-field experiments. Compared with previous works, the proposed method allows identification to be done more rapidly. The identification results are available immediately after each experimental run, and hence can be utilized in the design of the controller and guidance law without human intervention. This results in considerable improvements in system performances and substantial savings in ship-time.

The identification results indicate that the rotational drag coefficient a_{22} has a small variation around its mean when the speed varies. The rudder control authority b_2 varies linearly with the square of speed u^2 which matches well with our physical understanding.

We compare the SVF-RLS estimator against a conventional offline identi-

3.7 Summary

fication method that requires numerical optimization. The comparison shows that the SVF-RLS estimator outperforms the offline method in terms of the prediction accuracy, computational cost and shorter training time by detecting parameter convergence online.

The usefulness of the identified parameters is highlighted in two applications. We illustrate how the yaw identification results can be used to estimate the turning radius of the AUV at different speeds. The accuracy of the estimation is validated in a field experiment. The understanding of yaw dynamics at different speeds allows easy implementation of a gain-scheduled controller. The experimental results indicate that the gain-scheduled controller achieved better system performance compared with the existing constant-gain controller.

Chapter 4

Roll Control using an Internal Rolling Mass

When the roll angle is not small, the lift force generated by the rudder will affect the motion in the vertical plane (vehicle's diving subsystem) and vice versa, the lift force generated by the elevator will affect the motion in the horizontal plane (vehicle's steering subsystem). In order to meet the decoupling assumption, the roll angle of an AUV has to be kept small. To tackle this problem, we have developed an internal rolling mass (IRM) mechanism to actively stabilize the roll motion. To the best of our knowledge, we are the first to report the use of internal moving mass to stabilize the roll of an AUV. The use of linear motion requires a runway for the moving mass which is practically infeasible as the internal space already crowded with the essential components. We got around this limitation by designing a rolling mass mechanism that made use of the whole electronics tray (including batteries) as a moving mass. The moving mass is capable of rotating with respect to the longitudinal axis of the AUV – hence we call it as an internal rolling mass mechanism. The center of gravity (CG) of the IRM is off-centric. By rotating the IRM, we are effectively changing the CG of the AUV. By using the gravity force that is acting through the CG, we can generate the required torque to stabilize the roll dynamics.

4.1 Mechanical Design

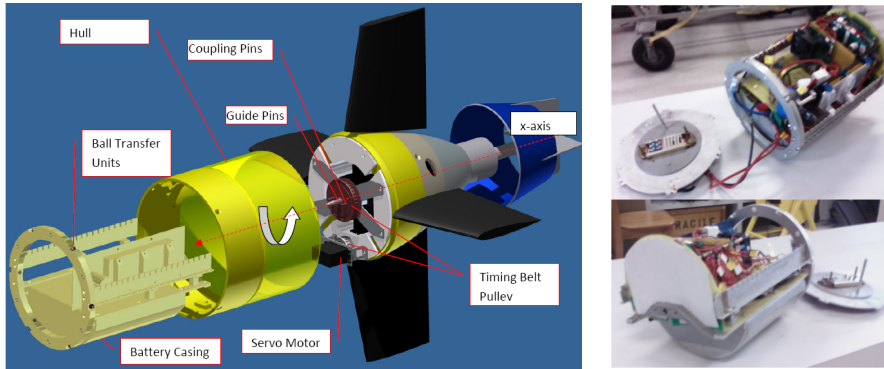


Figure 4.1: Mechanical design of the Internal Rolling Mass (IRM) mechanism. Pictures on the right show the tail electronic tray which has a battery tray that attached to its bottom half.

4.1 Mechanical Design

4.1.1 Design Requirements

We need a mechanism that is able to shift the CG of the AUV in the sway axis such that the roll equilibrium of the AUV can be changed by $\pm 5^\circ$. In order to shift the CG, we need some form of moving mass. So, it can be either a linear moving mass or a rotating mass. Our implementation using a rotating mass is illustrated in Fig. 4.1.

The actuation is provided by a servomotor mounted at the bottom end of the tail section through a bracket. It has a maximum torque of 1.92 Nm and maximum speed of 6.16 rad/s. Two timing belt pulleys are used for power transmission from the servomotor to the central axis. The drive pulley ratio is 1:2, thus increasing the output torque by a factor of two. Guide pins are used to guide the assembly of the whole tail tray (nickel bright in the figure) into the hull. Two coupling pins are used to transmit the torque from the central pulley to the tail tray. As the mass of the tail tray is contributed mainly by the battery placed in the bottom half, we are changing the CG of the AUV when the tail tray is rolling inside the hull.

This design fulfills the following requirements :

4.1 Mechanical Design

4.1.1.1 Space Constraint

Constrained by the AUV diameter of 200 mm, there is no sufficient runway for a linear moving mass to cause an effective change in CG. In addition, the existing components, such as electronics and battery, have already taken up most of the space in the tail section. So, without affecting components in other AUV's sections, we consolidate all the existing components in the tail section onto a tail tray, and make the tail tray as our moving mass. We were able to find space for a servomotor, two pulleys and a timing belt without making any change to the existing tail section (such as elongating it).

4.1.1.2 Energy Consumption

By having the mechanism at the tail section, we make use of the existing micro-controller to control the servomotor. The same micro-controller is used for thruster and fins control. Six ball transfer units are located on the outer ring of the tail tray. This effectively uses the ring as a bearing and allows low friction rotational motion. In order to provide the required torque and accuracy, we used a Futaba digital servomotor which consumes maximum 12 W. We use a timing belt drive system which has a low power transmission loss.

4.1.1.3 Ease of Assembly

Ease of assembly is one of the important design criteria. We occasionally need to disassemble the vehicle for routine maintenance and repairs. With the design, the assembly and disassembly work can all be performed by a single engineer in our laboratory within half an hour.

4.1.1.4 Effective change of CG

The servomotor has a usable range of 80°. After the pulley ratio, the range reduces to 40°. By placing the IRM at the center, we are able to roll the IRM to $\pm 20^\circ$; this translates to an effective change of CG to give a roll of $\pm 5^\circ$ ¹ at

¹Depending on the vehicle payload configuration, this range might change.

4.2 Modeling of Roll Dynamics

equilibrium.

4.2 Modeling of Roll Dynamics

In this section, we derive the dynamic model for the AUV's roll under consideration of CG shift due to the IRM. A six degree-of-freedom (DOF) dynamic model of an AUV is commonly described by a set of nonlinear equations with respect to two coordinate frames as indicated in Fig. 4.2(a). Detailed discussion on the modeling can be found in [20, 21]. However, for the purpose of this study, we restrict our analysis only on rolling motion and treat coupling torque induced by others DOFs to be disturbances.

In Fig. 4.2(a), we have the body-fixed frame at the center of buoyancy (CB) of the AUV. So the CB is located at $z_b = 0$ and $y_b = 0$ with respect to body-fixed frame. The CG is located below the CB in order to provide righting moment. So the CG location (y_g, z_g) has negative z_g with respect to body-fixed frame.

From Newton's Second Law of Motion (rotation), we can write the net total torque as the product of the moment of inertia I_{xx} and roll angular acceleration $\ddot{\phi}$.

$$\sum \tau = I_{xx} \ddot{\phi}. \quad (4.1)$$

The sum of the external torque consists of the following components:

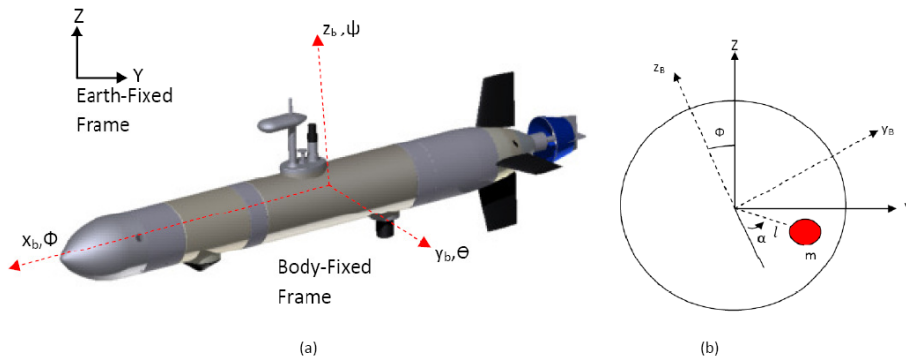


Figure 4.2: (a) Coordinate Reference Frame (b) Free Body Diagram.

4.2 Modeling of Roll Dynamics

4.2.1 Hydrostatic Righting Moment

The hydrostatic righting moment is the combined effect of the vehicle's weight W and buoyancy B . The STARFISH AUV is slightly positively buoyant but as we put the body-fixed frame at the CB, buoyancy does not play a role in the equation. The roll torque due to the hydrostatic righting moment is

$$\tau_{Hydro} = -y_g W \cos \phi + z_g W \sin \phi. \quad (4.2)$$

The IRM is treated as a point mass with effective length l from the center. The effective length l is the distance from the CB to the CG of the tail tray. Let α denote the angular position of the point mass as illustrated in Fig. 4.2(b). When the point mass is rolling in the AUV, it is effectively changing the CG of the AUV. The new CG position (y'_g, z'_g) is described in following two equations:

$$y'_g = y_g + \frac{m}{M} l \sin \alpha \quad (4.3)$$

$$z'_g = z_g - \frac{m}{M} l \cos \alpha \quad (4.4)$$

where m is the mass of tail tray and M is the mass of the whole AUV.

By substituting (4.3) and (4.4) into (4.2), the hydrostatic righting moment becomes

$$\tau_{Hydro} = -(y_g + \frac{m}{M} l \sin \alpha) W \cos \phi + (z_g - \frac{m}{M} l \cos \alpha) W \sin \phi. \quad (4.5)$$

It is useful to note that the hydrostatic moment stabilizes the roll motion as the moment always acts against any deflection in roll. So the roll dynamics are self-stabilized in this sense.

4.2.2 Rolling Drag

As a streamlined AUV, the main rolling drag of the STARFISH AUV comes from the four fins that protrude out from the center axis. We model the drag

4.2 Modeling of Roll Dynamics

as a quadratic drag:

$$\tau_{Drag} = K_{pp}p|p| \quad (4.6)$$

where K_{pp} is the rolling quadratic drag coefficient and p is the angular velocity of the roll. Since we restrict our discussion in roll axis only, we have $p = \dot{\phi}$.

4.2.3 Rolling Added Mass

Added mass is a measure of the mass of the moving water when the vehicle accelerates. For a streamlined AUV, rolling added mass due to the AUV hull is small. So the main rolling added mass is again due to the fins. We model the moment due to the added mass as follows:

$$\tau_{AM} = K_{\dot{p}}\dot{p} \quad (4.7)$$

where $K_{\dot{p}}$ is the rolling added mass coefficient and \dot{p} is the angular acceleration of roll. Similarly, we have $\dot{p} = \ddot{\phi}$.

4.2.4 Propeller Induced Torque

When the propeller rotates clockwise to provide the forward thrust, it also creates an anti-clockwise torque acting on the AUV. This is commonly known as the *torque effect*. The magnitude of the torque depends on the power output of the thruster, P and propeller revolution, ω in the following equation:

$$\tau_{prop} = \frac{P}{\omega}. \quad (4.8)$$

Power produced by the thruster is the product of thrust F , and speed of the AUV V . However during steady state (constant velocity) AUV motion, thrust is equal to the drag force, F_{drag} , and therefore

$$P = FV = F_{drag}V \quad (4.9)$$

$$F_{drag} = \frac{1}{2}\rho AC_d V^2 \quad (4.10)$$

4.2 Modeling of Roll Dynamics

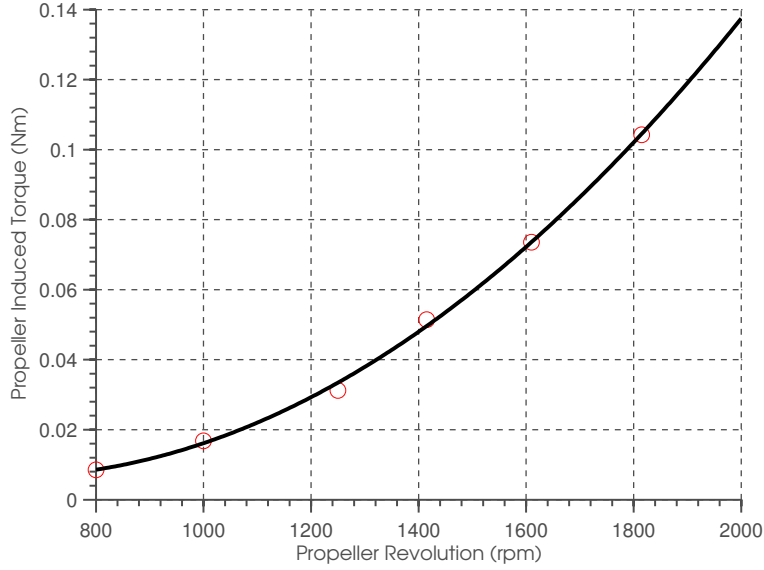


Figure 4.3: Propeller induced torque versus propeller revolution

where ρ is the sea water density; A is the frontal area; C_d is the drag coefficient. So, by running different constant thrusts experiments, we plot the induced torque against the propeller revolution in Fig. 4.3. The data best fits a quadratic equation showing $\tau_{prop} \propto \omega^2$.

In our subsequent analysis, we omit the induced torque and treat it as a disturbance to the system. However, we pre-roll the AUV to $+5^\circ$ during weight trimming to compensate for the thruster torque at nominal speed. When the AUV moves at its nominal speed of 1.4 m/s with 1400 rpm, the induced torque will roll back the AUV to zero roll position and thus leave sufficient room for IRM to compensate for the rest of the variations.

By substituting (4.5), (4.6), (4.7) and (4.8) into (4.1) and rearranging the terms, we have

$$\begin{aligned}
 (I_{xx} - K_{\dot{p}})\ddot{\phi} &= -(y_g + \frac{m}{M}l \sin \alpha)W \cos \phi \\
 &+ (z_g - \frac{m}{M}l \cos \alpha)W \sin \phi \\
 &+ K_{pp}p|p| \\
 &+ \tau_{prop}.
 \end{aligned} \tag{4.11}$$

4.3 System Identification

We obtain the transfer function of roll ϕ , as a function of α in (4.12) by first linearizing (4.11) at the operating point $\phi = 0$. At this point $\cos \phi \simeq 1$ and $\sin \phi \simeq \phi$. α can be assumed to be small. Therefore $\cos \alpha \simeq 1$ and $\sin \alpha \simeq \alpha$. Next, we approximate the quadratic drag $K_{pp}p|p|$ as linear drag $K_p p$. By trimming condition, y_g is close to zero and thus ignored. Lastly, τ_{prop} is treated as disturbance and is not included in the equation.

$$\frac{\Phi(s)}{\alpha(s)} = \frac{- \left[\frac{(\frac{m}{M})lW}{I_{xx} - K_{\dot{p}}} \right]}{s^2 - \left[\frac{K_p}{I_{xx} - K_{\dot{p}}} \right] s - \left[\frac{(z_g - (\frac{m}{M})l)W}{l_{xx} - K_{\dot{p}}} \right]}. \quad (4.12)$$

By assigning the constant parameters k , a , and b to its corresponding coefficient respectively, (12) becomes:

$$\frac{\Phi(s)}{\alpha(s)} = \frac{k}{s^2 + as + b}. \quad (4.13)$$

4.3 System Identification

In this section, we estimate the three unknown parameters a , b and k of the linear second-order roll-axis model presented in (4.13). We also identify $K_{\dot{p}}$, K_{pp} , and l for the nonlinear equation (4.11). Parameters such as I_{xx} , y_g , z_g , m , M , W can either be measured directly or calculated through computer-aided design (CAD) softwares. Numerical values for these parameters are tabulated in Table 4.1.

We need to perform open-loop testing by changing α using a step function between $\pm 20^\circ$ and then record the roll response. Ideally, the test should be carried out while the AUV is maintaining constant thrust, depth, and heading. This will minimize the coupling torque generated by those degrees of freedom. However, the open loop tests might pose a danger to the operation of the AUV as we are testing some unknown behavior of the roll dynamics. A more natural choice would be to carry out the open-loop test while AUV is at rest in a water tank. This turns out to be sufficient to obtain a nominal model

4.3 System Identification

Table 4.1: Model parameters

Calculated Parameters	Values	Identified Parameters	Values
I_{xx}	0.474 kg m ²	a	0.24
y_g	0 mm	b	5.21
z_g	-3.4 mm	k	-0.61
m	2.00 kg	$K_{\dot{p}}$	-0.08 kg m ²
M	61.41 kg	K_{pp}	-1.21 Nms ²
W	602.5 N	l	43.36 mm

for the roll dynamics for the following reasons. First, in our model, we treat the propeller induced torque as a disturbance. So, whether the thruster is running or not, it is not included in the model. Second, the roll dynamics model is derived under a decoupling assumption and therefore it is free from excitation from the other axis. Third, the tank test underestimates the drag coefficient as the conning tower and the top fin are not fully submerged in the water. However, it is better to underestimate the drag in our case as higher drag will make the roll dynamics more stable. It will also ensure that the designed controller will also work properly when the vehicle is on the surface before it starts diving.

While the AUV is static in the tank, we command three step inputs of α (-20°, 0° and 20°) and observe how the roll responds to the step change of α . Sufficient time was allowed for the roll response to decay before another step change. The results are shown in Fig. 4.4. The simulated roll response is overlaid together with the experimental measured roll response. The result shows a good match between the two. The simulated roll is generated from the nonlinear model after the unknowns are identified. The three unknown parameters were identified by numerically minimizing the root mean square error ϕ_{rms} defined as:

$$\Phi_{rms} = \sqrt{\frac{\sum_{i=1}^n (\phi_i - \hat{\phi}_i)^2}{n}}. \quad (4.14)$$

4.3 System Identification

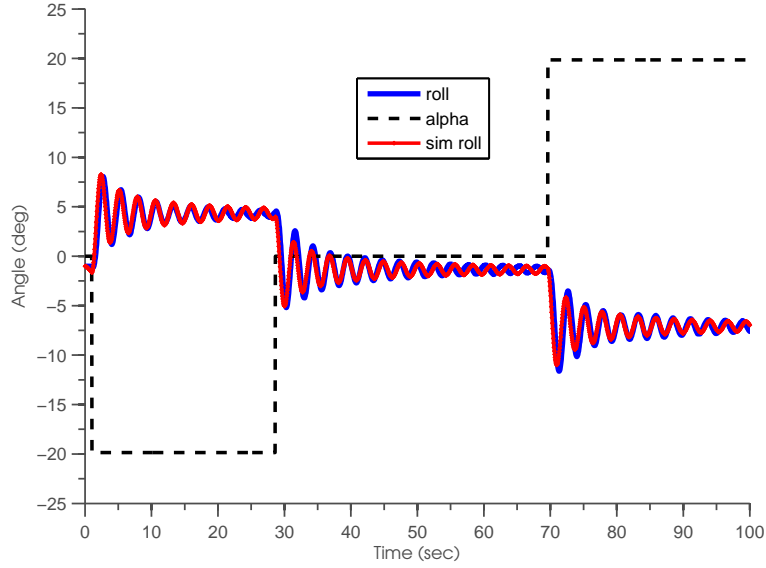


Figure 4.4: Simulated and measured roll response under step input. The simulated roll response matched closely with the measured roll response despite small differences in amplitude and phase

where $\hat{\phi}$ is the simulated roll response and n is the number of samples. The Nelder-Mead simplex method was used to search for the optimal parameters set in the sense of least squares.

It is important to note that the α is the command given to the servomotor. There is no instrument to measure the position of the rolling mass. So, some latency is expected between the commanded α and the actual α . We model the latency by a first order system with a time constant τ_{delay} . In order to identify the time constant, we perform a dynamic test by commanding α randomly between $\pm 20^\circ$ to obtain the response shown in Fig. 4.5. Similarly, the time constant is identified by minimizing ϕ_{rms} . The resultant transfer function in (4.13) becomes:

$$\frac{\Phi(s)}{\alpha(s)} = \left(\frac{1}{\tau_{delay}s + 1} \right) \left(\frac{k}{s^2 + as + b} \right) \quad (4.15)$$

with $\tau_{delay} = 0.5$ s.

4.4 Controller Design

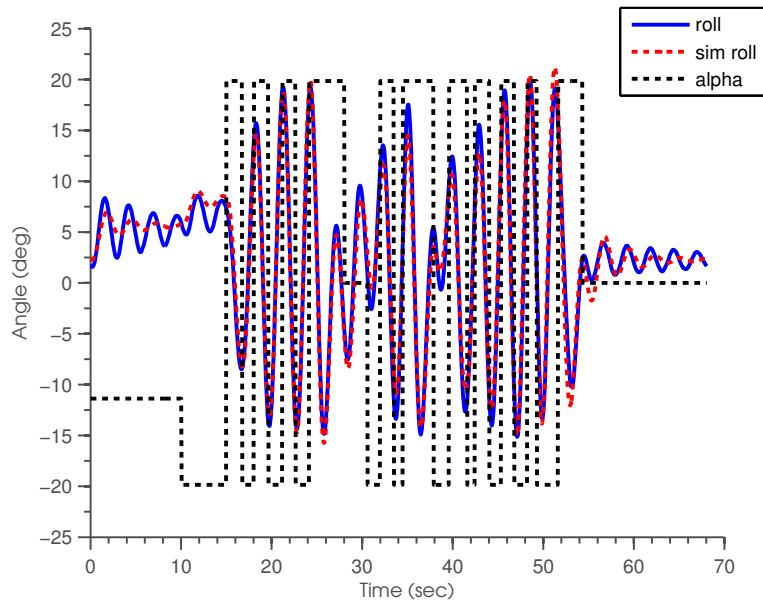


Figure 4.5: Simulated and measured roll response under random input.

4.4 Controller Design

In this section, we design a Proportional-plus-Integral (PI) controller that stabilizes the AUV's roll motion. The PI controller is used to reduce the roll oscillation by increasing the damping of the system and at the same time maintain zero steady state error. The controller was synthesized base on root locus design (Fig. 4.6). The open loop transfer function has a pair of complex-conjugate *poles* close to the imaginary axis in the *s*-plane. This indicates the system is lightly damped with a damping ratio of 0.07. Fig. 4.6 also shows that the system is only stable for a small region of the root locus; it is stable for closed-loop gain range between $(0 < Kp < 8.50)$. The region that is stable appears to be lightly damped as well. By increasing the gain, we bring the pair of complex-conjugate *poles* to a region of higher damping. However, the third *pole* moves closer to the right-half plane as the gain increases. As the *poles* are close to each other, we cannot analyze the system purely based on a second-order approximation. Instead, we simulate the nonlinear model and fine tune the controller gain using the simulation results. An ideal integral was added with a *zero* at 0.01. The fourth closed-loop *pole* is found at -0.0144,

4.4 Controller Design

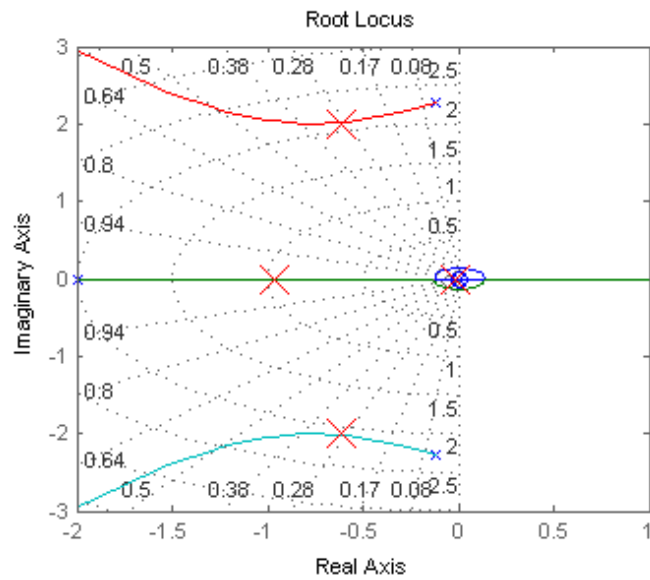


Figure 4.6: Root locus plot for compensated system.

which is close enough to the *zero* to cause *pole-zero* cancellation. All *poles* and *zero* of the open and closed-loop plant are tabulated in Table 4.2. Integrator windup is avoided by preventing the integral term from accumulating above or below 20° .

4.5 Result and Discussion

Table 4.2: Open and Closed Loop Plants

	Open loop	Closed loop
Plant	$\frac{K}{(s+2)(s^2+0.24s+5.21)}$	$\frac{K(s-0.01)}{s(s+2)(s^2+0.24s+5.21)}$
K	-1.22	-6.10
Kp	-	5
Poles	$-0.12 + 2.2794i$ $-0.12 + 2.2794i$ -2	$-0.617 + 2.0077i$ $-0.617 + 2.0077i$ -0.9609 -0.0144
Zeros	-	0.01
System Type	0	1

4.5 Result and Discussion

The performance of the internal rolling mass in controlling the roll was first studied in a tank test and later at an open-field trial. For the tank test, we gave an impulse to the AUV by pushing AUV to roll to 25° and observed how the roll decays for open-loop and closed-loop control respectively. The results are shown in Fig. 4.7. The closed-loop response settled down within 4 seconds whereas the open-loop system takes more than 10 seconds to settle down. Fig. 4.7 also shows how the α changes with time in order to damp down the roll. For the open-loop test, α was kept at a constant 0° .

Fig. 4.8 shows the AUV's roll response during a constant 2 m diving mission at the speed of 1.4 m/s when traveling on a straight path. When the IRM mechanism was turned off (open loop), the AUV's roll response was oscillatory with the standard deviation of 1.02° . On the contrary, when the IRM mechanism was turned on (closed loop), the oscillatory roll motion was damped. The moving mass rolls to negative alpha region to neutralize the induced propeller torque. The standard deviation of roll reduced to 0.393° . Table 4.3 summarizes the test results into two statistics: mean and standard deviation. The mean value of the roll response shows that the oscillation was centered at zero. In short, the result shows that the IRM mechanism suppressed the unwanted roll oscillation to a smaller amplitude with center

4.5 Result and Discussion

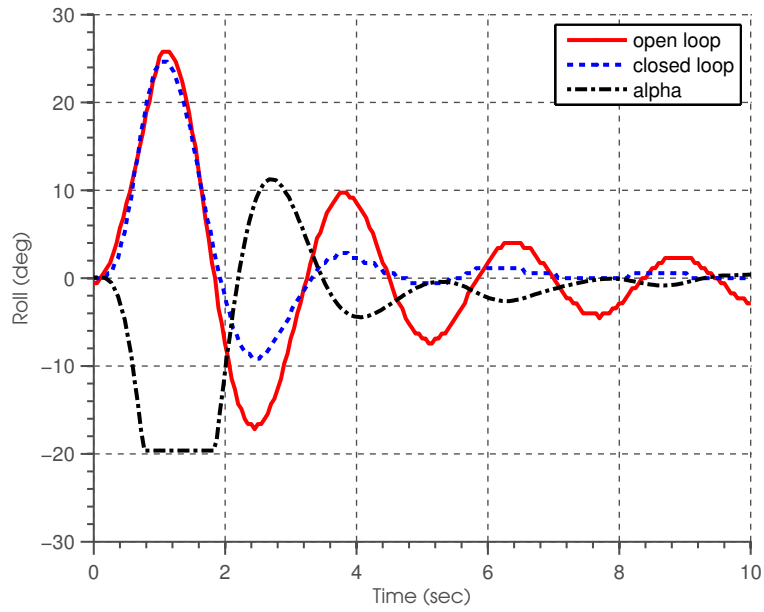


Figure 4.7: Tank Test Result. The result shows that despite actuator saturation, the IRM mechanism manages to damp down the oscillation faster.

Table 4.3: Open and Closed Loop Performance

	Open loop	Closed loop
Mean	-2.808 °	0.039 °
Standard Deviation	1.023 °	0.393 °

around zero.

4.6 Summary

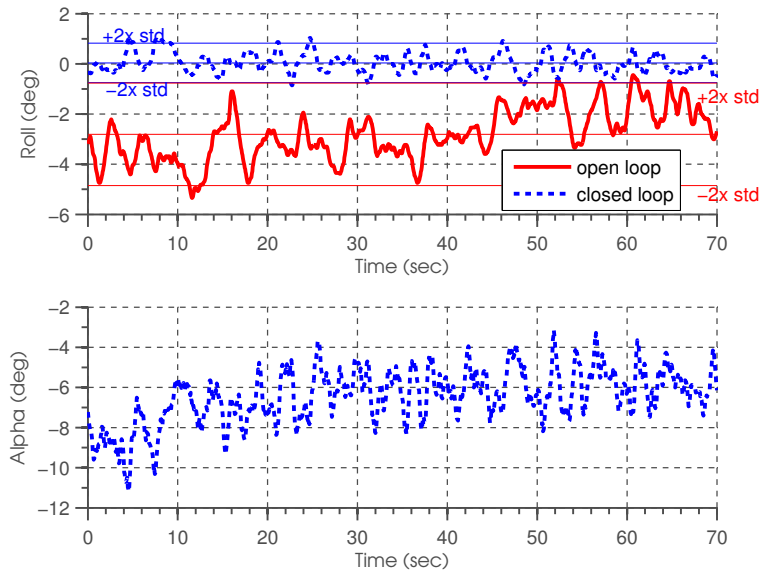


Figure 4.8: Field Experiment Result.

4.6 Summary

In this chapter, we have demonstrated the use of an internal rolling mass mechanism for active roll stabilization in the STARFISH AUV. A nonlinear model was first developed to describe the dynamics of the AUV's roll. The model was later linearized to obtain a transfer function for controller synthesis. The model parameters were identified through open-loop testing in the water tank. A PI controller was then designed to increase the damping of the overall system and to remove the steady state error. The capability of the IRM mechanism to stabilize the roll motion was demonstrated in both tank tests and field experiments.

Chapter 5

Minimum Speed Seeking Control

As the dynamic model is scheduled according to the vehicle's forward speed, the operating range of the speed needs to be known. The maximum speed is determined by the maximum thrust produced by the thruster, whereas the minimum speed is not zero, but a certain speed at which the AUV must travel for depth keeping. When the control fins lose their effectiveness at low speed, the extra buoyancy will bring the AUV up to the surface.

In this chapter, we will explain the mechanism behind the phenomenon of the minimum speed. We first define the minimum speed formally and then derive the solution together with its condition of existence. Next, we introduce a new behavior to the AUVs: while the AUV maintains a certain depth, its cruising speed is continuously regulated in real-time to its minimum. This behavior is totally new and has not been developed previously, and it is useful when we require minimum energy consumption, minimum impact when docking the AUV, and slowest passage over the target of interest.

From the simulation studies and experimental results, we find that the proposed minimum speed seeking algorithm is robust to changes in the vehicle dynamics as well as environmental disturbances. We recommend implementation of the algorithm on existing AUVs and hope that this will open up new possibilities in the operation and application of the AUVs.

5.1 Dynamic Model - Dive Plane

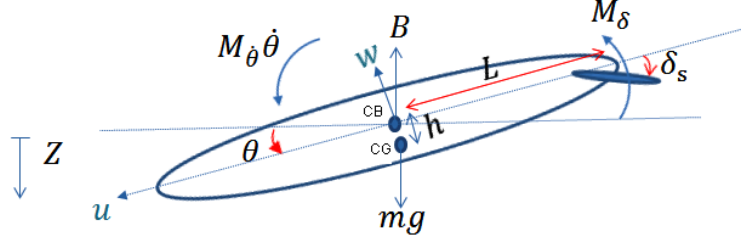


Figure 5.1: Free body diagram in dive-plane.

5.1 Dynamic Model - Dive Plane

In this section, the dynamical model of a streamline, tail-controlled AUV is constructed by restricting the motion of the AUV to the dive-plane. By deriving the dynamic model, we try to understand the underlying interaction of forces and moments, and thus the mechanism behind the existence of the minimum speed. The model is also used later in a simulation to study the performance of the proposed minimum speed seeking algorithm.

Dynamic modeling of the underwater vehicle can be found throughout the literature [61, 14, 20]. Here, we adopt the model developed by [19], in which the equation of motions are written in the stability-axis frame of the AUV. This enables the hydrodynamic forces and moments to be more conveniently expressed.

Figure 5.1 shows three reference frames that are used to describe the motion of the AUV. They are labeled in green. First, the body-axis frame is centered at the vehicle center of buoyancy (CB) and the x_b axis is running along the longitudinal axis of symmetry with positive pointing toward vehicle nose. The y_b axis is pointing at the starboard side of the AUV, and the z_b axis which is orthogonal to both x_b and y_b , is pointing toward bottom of the vehicle. Second, the inertia-axis frame is defined by pointing the Z with the gravitational force and aligning the Y with y_b . Finally, stability-axis frame has its x_v axis placed along the vehicle velocity and aligning the y_v with y_b . The body-axis and inertia-axis frame are related through a rotation about the common y axis with the pitch angle θ ; whereas the body-axis and stability-axis frame are related through the angle of attack α about the same

5.1 Dynamic Model - Dive Plane

y axis. According to the defined frames, θ is positive when AUV is upward pitching and negative when it is downward pitching. Similar sign convention apply for α as well.

We assume sway velocity v and vehicle roll ϕ to be zero. This is in alignment with the widely used decoupled assumption for streamlined AUVs [14, 13]. We are interested to model the vehicle states: depth Z , vehicle speed V , angle of attack α , pitch θ and pitch rate q , given the elevator deflection δ and thruster force F_t as the inputs.

5.1.1 Kinematics

From a kinematics analysis of Figure 5.1, the rate of change of depth, \dot{z} is

$$\dot{z} = V[-\cos \alpha \sin \theta + \sin \alpha \cos \theta] \quad (5.1)$$

The vehicle speed V is related to body-axis surge velocity u and heave velocity w as

$$u = V \cos \alpha \quad \text{and} \quad w = V \sin \alpha \quad (5.2)$$

Vehicle speed V , is the vehicle speed relative to the surrounding water, which determines the hydrodynamic forces acting on the vehicle body and fins. Thus, it is invariant under the effect of underwater current. On the other hand, the vehicle ground speed, which is the resultant of vehicle speed V and underwater current, is affected by the current.

5.1.2 Equations of motion

From [19], the equations of motion containing state vector $\mathbf{x} = [V, \alpha, q, \theta]$ and input $\mathbf{u} = [\delta, F_t]$ can be written as

$$\mathbf{E}\mathbf{T}(\mathbf{x})\dot{\mathbf{x}} = \mathbf{R}(\mathbf{x}) + \mathbf{F}(\mathbf{x}, \mathbf{u}) \quad (5.3)$$

5.1 Dynamic Model - Dive Plane

The transformation matrix $\mathbf{T}(\mathbf{x})$ is given by

$$\mathbf{T}(\mathbf{x}) = \begin{pmatrix} \cos \alpha & -V \sin \alpha & 0 & 0 \\ \sin \alpha & V \cos \alpha & 0 & 0 \\ 0 & 0 & 1 & 0 \\ 0 & 0 & 0 & 1 \end{pmatrix} \quad (5.4)$$

and the inertia matrix \mathbf{E} is given by

$$\mathbf{E} = \begin{pmatrix} m_x & 0 & mz_{cg} & 0 \\ 0 & m_z & -mx_{cg} & 0 \\ mz_{cg} & -mx_{cg} & J_y & 0 \\ 0 & 0 & 0 & 1 \end{pmatrix} \quad (5.5)$$

The right hand side terms are

$$\mathbf{R}(\mathbf{x}) = \begin{pmatrix} -m_z q V \sin \alpha - mx_{cg} q^2 \\ m_x q V \cos \alpha + mz_{cg} q^2 \\ (m_z - m_x) V^2 \cos \alpha \sin \alpha - m(x_{cg} \cos \alpha + z_{cg} \sin \alpha) q V \\ q \end{pmatrix} \quad (5.6)$$

and

$$\mathbf{F}(\mathbf{x}, \mathbf{u}) = \begin{pmatrix} F_x(\mathbf{x}, \mathbf{u}) \\ F_z(\mathbf{x}, \mathbf{u}) \\ M_y(\mathbf{x}, \mathbf{u}) \\ 0 \end{pmatrix} \quad (5.7)$$

where m is the dry mass of the vehicle. m_x and m_z denote the dry mass plus added mass in surge and heave direction respectively. The vehicle's moment of inertia around the pitch axis including added moment of inertia is J_y . The distance vector from the center of gravity to the center of buoyancy is $\mathbf{r}_{cg} = [x_{cg} \ y_{cg} \ z_{cg}]$.

5.1 Dynamic Model - Dive Plane

External forces and moments are of the form

$$F_x(\mathbf{x}, \mathbf{u}) = \cos \alpha F_D(V, \alpha, \delta) - \sin \alpha F_L(V, \alpha, \delta) - (F_W - F_B) \sin \theta + F_t \quad (5.8)$$

$$F_z(\mathbf{x}, \mathbf{u}) = \sin \alpha F_D(V, \alpha, \delta) + \cos \alpha F_L(V, \alpha, \delta) + (F_W - F_B) \cos \theta \quad (5.9)$$

$$M_y(\mathbf{x}, \mathbf{u}) = M_q(V, \alpha, q, \delta) - (x_{cg} \cos \theta + z_{cg} \sin \theta) F_w \quad (5.10)$$

F_w and F_B are vehicle's weight and buoyancy forces respectively. The extra buoyancy is calculated by finding the difference between the weight and buoyancy is $(F_w - F_B)$. The last term in (5.10), $(x_{cg} \cos \theta + z_{cg} \sin \theta) F_w$ is the hydrostatic righting moment. Thrust force is denoted as F_t . The hydrodynamic drag, lift force and pitch moment generated by the vehicle's body and fins are $F_D(V, \alpha, \delta)$, $F_L(V, \alpha, \delta)$ and $M_q(V, \alpha, q, \delta)$ respectively. They are modeled as follows:

$$F_D(V, \alpha, \delta) = \frac{1}{2} \rho V^2 A_b C_{D_0} \quad (5.11)$$

$$F_L(V, \alpha, \delta) = \frac{1}{2} \rho V^2 \{A_b C_{L_\alpha} \alpha + A_f C_{L_\delta} \delta\} \quad (5.12)$$

$$M_q(V, \alpha, q, \delta) = \frac{1}{2} \rho V^2 \{A_b L [C_{m_\alpha} \alpha + C_{m_q} q] + A_f x_f C_{L_\delta} \delta\} \quad (5.13)$$

ρ is the water density. A_b and A_f are the reference surface area for body and fins respectively. L is the reference length of the vehicle, whereas x_f is the distance between the fins and center of buoyancy (see Figure 5.1). The hydrodynamic coefficients, for drag, body lift and fins lift are C_{D_0} , C_{L_α} and C_{L_δ} respectively. As for pitch moment, the hydrodynamic coefficients C_{m_α} accounts for the body's restoring moment and C_{m_q} accounts for the viscous damping.

5.1.3 Maximum elevator deflection, δ_{\max}

A typical lift curve is shown in Figure 5.2 for the NACA-0012 fin profile. From zero deflection, the coefficient of lift increases with the elevator deflection. The trend continues up to a critical angle, also known as the fin stall angle

5.1 Dynamic Model - Dive Plane

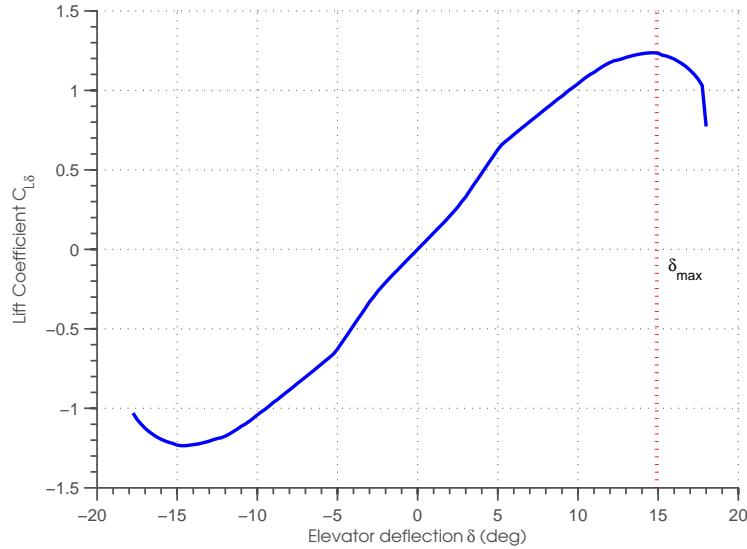


Figure 5.2: Typical lift coefficient versus fin deflection for NACA-0012 fin profile at Reynolds number 500 k. (Source: Airfoil tool generator at <http://airfoiltools.com/airfoil/details?airfoil=n0012-il>)

which produces maximum lift coefficient. Beyond this critical angle, the upper surface flow becomes more separated and the fins produce less coefficient of lift. Hence, the AUV is said to be in a stall condition when the elevator operates above the fin stall angle, δ_{Stall} .

According to the lift equation, Lift L produced by a fin is equal to the lift coefficient C_L times the density ρ times half of the velocity V squared times the wing area A_f .

$$L = \frac{1}{2} A_f C_L \rho V^2 \quad (5.14)$$

As the C_L varies linearly with the elevator deflection δ , the lift coefficient is approximated as

$$C_L = C_{L\delta} \delta, \quad (5.15)$$

where $C_{L\delta}$ is the slope of the lift curve (Figure 5.2). This gives rise to the lift force generated by fins at (5.12).

5.1 Dynamic Model - Dive Plane

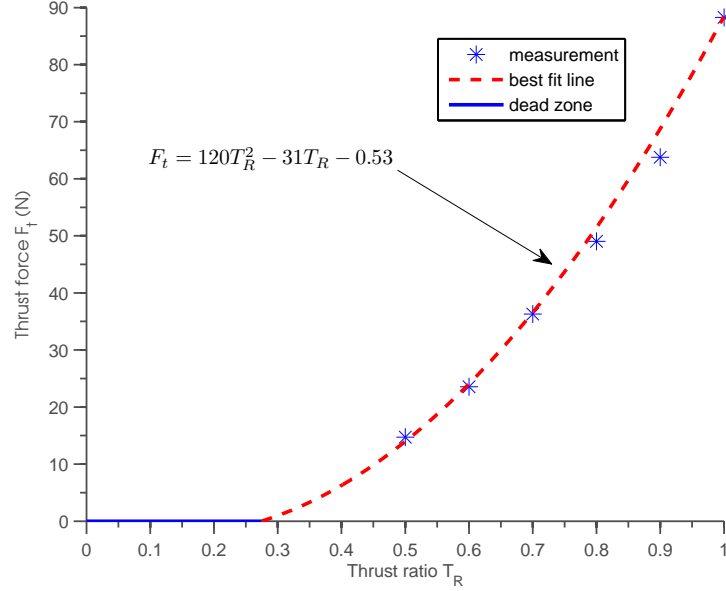


Figure 5.3: Relationship between thrust ratio T_R and thrust force F_t for Tecnadyn Model 520 underwater thruster.

Most controller designs require the fins to work within the linear region and thus fin stall has to be avoided. Hence, we introduce a saturation block which sets the maximum elevator deflection from the pitch controller to δ_{\max} . The value of δ_{\max} is normally chosen to be less than or equal to δ_{Stall} .

5.1.4 Thruster model

We normalize the thrust force F_t into a scale from 0 to 1, and it is denoted as thrust ratio T_R . The relationship between T_R and the actual thrust force produced by the thruster is shown in Figure 5.3. There is a dead zone from 0 to 0.28 where no thrust is generated. From 0.28 onward, the thrust force increase quadratically with the thrust ratio as shown by Figure 5.3.

$$F_t = 120T_R^2 - 31T_R + 0.53 \quad (5.16)$$

Equation (5.16) is obtained by best fit the quadratic equation on the measurements made by the thruster manufacturer. The value 0.28 is obtained

5.2 Minimum Speed and its Characteristics

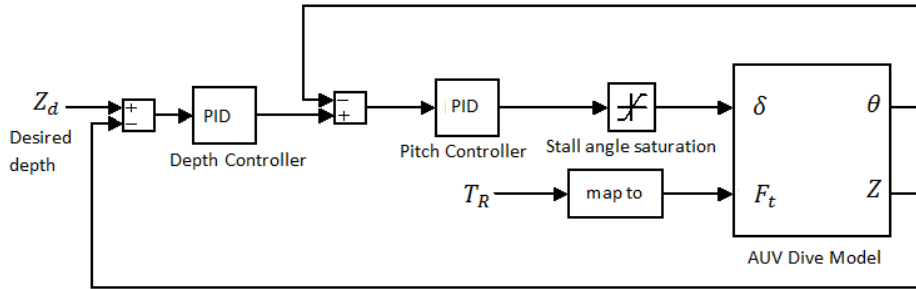


Figure 5.4: Depth Subsystem with dual closed-loop control: inner pitch control and outer depth control.

at the intersection between the best fit curve and the x-axis.

5.1.5 Depth closed-loop system

Dual loop control is implemented to regulate the AUV depth. We have pitch control in the inner-loop and depth control in the outer loop. The dual-loop implementation is widely used for depth control of the torpedo-shaped AUV [13, 21, 62]. The torpedo-shaped AUV is underactuated, such that the depth and pitch cannot be controlled independently. Hence, given a desired depth, the outer depth control loop is used to generate the desired pitch angle, which is then fed into the inner pitch control loop to generate the elevator command.

Here, the Proportional-Integral (PI) controllers are employed in both the inner and outer loops. Integral controller is needed in order to remove the steady state error when a step input is fed. We assume that the depth and pitch controllers will stabilize the plant when the AUV's operating speed is larger than the minimum speed. This is a reasonable assumption, as such controllers should already be functioning in basic AUV operations.

5.2 Minimum Speed and its Characteristics

In this section, we begin with the calculation of the minimum speed based on the model described in Section 5.1. First, the formal definition of the minimum speed is given. Next, we derive the equations for two important

5.2 Minimum Speed and its Characteristics

curves: maximum required pitch curve and achievable pitch curve. We then argue that the minimum speed occurs at the intersection of these two curves. The final solution of the minimum speed is then derived together with its condition of existence. By analyzing the maximum required pitch curve and the achievable pitch curve, we study how the buoyancy, righting moment, and the fin's effectiveness affect the minimum speed. In Section 5.2.2, we observe how the *STARFISH* AUV loses its pitch-controllability when it cruises below the minimum speed. There are two strong indications when the AUV loses its pitch-controllability: the pitch response deviates from the desired pitch, and the elevator deflection becomes saturated.

5.2.1 The minimum speed

Let first define the minimum speed of an AUV. The minimum speed is the vehicle's speed when

1. Depth rate defined by (5.1) equal to zero, $\dot{Z} = 0$
2. Elevator deflection δ is at its maximum value, $\delta = \delta_{\max}$
3. The AUV is at an equilibrium point of (5.3), $\dot{\mathbf{x}} = 0$.

To maintain depth, the depth rate should be equal to zero. So from (5.1), we solve for the relationship between α and θ :

$$\dot{z} = V[-\cos \alpha \sin \theta + \sin \alpha \cos \theta] = 0 \Rightarrow \alpha = \theta, \quad (5.17)$$

which mean for constant depth maneuver, the angle of attack is equal to pitch angle.

When the AUV is at equilibrium, we have

$$\mathbf{R}(\mathbf{x}) + \mathbf{F}(\mathbf{x}, \mathbf{u}) = \mathbf{0} \quad (5.18)$$

because $\mathbf{ET}(\mathbf{x})$ in (5.3) is nonsingular for a slender vehicle at non-zero speed as pointed out by [19].

5.2 Minimum Speed and its Characteristics

Then, (5.18) is expanded to

$$\begin{pmatrix} -m_z q V \sin \alpha - m x_{cg} q^2 \\ m_x q V \cos \alpha + m z_{cg} q^2 \\ (m_z - m_x) V^2 \cos \alpha \sin \alpha - m(x_{cg} \cos \alpha + z_{cg} \sin \alpha) q V \\ q \end{pmatrix} = - \begin{pmatrix} F_x(\mathbf{x}, \mathbf{u}) \\ F_z(\mathbf{x}, \mathbf{u}) \\ M_y(\mathbf{x}, \mathbf{u}) \\ 0 \end{pmatrix} \quad (5.19)$$

The last row requires pitch rate to be zero, $q = 0$, and (5.19) becomes

$$F_x(\mathbf{x}, \mathbf{u}) = 0 \quad (5.20)$$

$$F_z(\mathbf{x}, \mathbf{u}) = 0 \quad (5.21)$$

$$M_y(\mathbf{x}, \mathbf{u}) = -(m_z - m_x) V^2 \cos \alpha \sin \alpha \quad (5.22)$$

Calculating (5.20) $\times \cos \theta$ + (5.21) $\times \sin \theta$, and knowing $\alpha = \theta$, we have

$$F_D(V, \alpha, \delta) = -F_t \cos \theta \quad (5.23)$$

$$(5.24)$$

and substitute $F_D(V, \alpha, \delta)$ from (5.11), we obtain

$$\frac{1}{2} \rho V^2 A_b C_{D_0} = -F_t \cos \theta \quad (5.25)$$

Calculating (5.20) $\times \sin \theta$ - (5.21) $\times \cos \theta$, and knowing $\alpha = \theta$, we have

$$F_L(V, \alpha, \delta) + (F_w - F_B) = F_t \sin \theta \quad (5.26)$$

and substitute $F_L(V, \alpha, \delta)$ from (5.12), we obtain

$$\frac{1}{2} \rho V^2 \{A_b C_{L_\alpha} \alpha + A_f C_{L_\delta} \delta\} + (F_w - F_B) = F_t \sin \theta \quad (5.27)$$

By combining (5.25) and (5.27), and knowing $\alpha = \theta$, $\delta = \delta_{\max}$, and assuming θ to be a small angle ($\sin \theta \approx \theta$, $\tan \theta \approx \theta$), we solve θ as a function

5.2 Minimum Speed and its Characteristics

of V as

$$\theta_{\max.\text{req}} = \frac{F_B - F_w}{\frac{1}{2}\rho A_b(C_{L_\alpha} + C_{D_0})V^2} - \frac{A_f C_{L_\delta} \delta_{\max}}{A_b(C_{L_\alpha} + C_{D_0})} \quad (5.28)$$

We denote the pitch angle calculated from (5.28) as $\theta_{\max.\text{req}}$ because it is the pitch angle that is required to overcome the positive buoyancy of the AUV during level flight at various speeds. During level flight, the AUV needs to maintain negative pitch angle (pitch down) to overcome the positive buoyancy. As the buoyancy does not change with speed, the AUV needs more downward pitching to produce the required downward force when the speed V is low (at low thrust ratio) as shown in Figure 5.5.

In addition, $\theta_{\max.\text{req}}$ is the maximum angle because δ is set to its maximum value δ_{\max} in (5.28). Let us explain this with an example: if the AUV is traveling at 1 m/s, Figure 5.5 indicates that the $\theta_{\max.\text{req}} = -5$ deg. However, in reality, as the minimum speed is not 1 m/s and thus δ is not at its maximum value, the AUV is pitching down at a smaller¹ pitch angle during level flight. So, in this sense, the maximum required pitch curve indicates the largest pitch angle that is required to maintain level flight, which only occurs at the minimum speed.

Next, we calculate the achievable pitch angle θ_{ach} by solving pitch moment balance in (5.22) when the elevator deflection δ is set to its maximum, δ_{\max} . Substitute (5.10) and (5.13) into (5.22), we have

$$\begin{aligned} \frac{1}{2}\rho V^2 \{A_b L [C_{m_\alpha} \alpha + C_{m_q} q] + A_f x_f C_{L_\delta} \delta\} - (x_{cg} \cos \theta + z_{cg} \sin \theta) F_w \\ = -(m_z - m_x) V^2 \cos \alpha \sin \alpha \end{aligned} \quad (5.29)$$

Given $\alpha = \theta$, $q = 0$, $\delta = \delta_{\max}$, and assuming θ to be a small angle and $x_{cg} = 0$, we solve θ_{ach} as a function of V as

$$\theta_{\text{ach}} = \frac{\frac{1}{2}\rho A_f x_f C_{L_\delta} \delta_{\max} V^2}{z_{cg} F_w - [\frac{1}{2}\rho A_b L C_{m_\alpha} + (m_z - m_x)] V^2} \quad (5.30)$$

¹in term of magnitude

5.2 Minimum Speed and its Characteristics

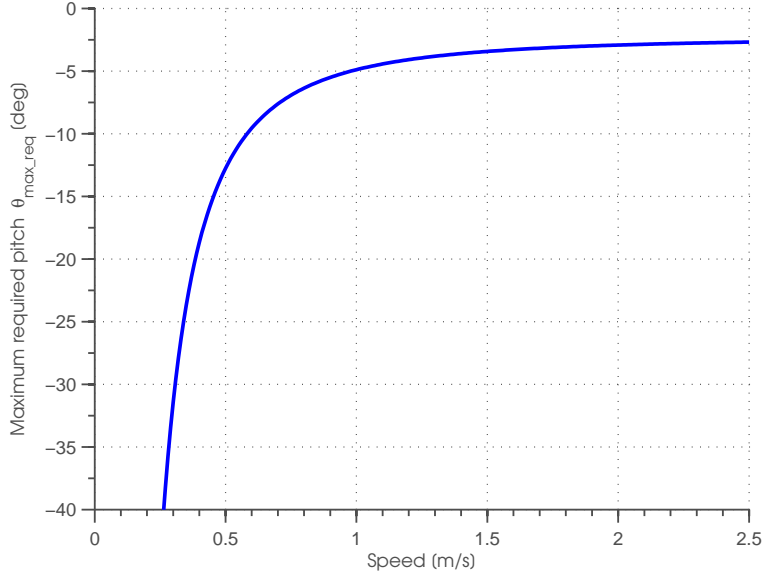


Figure 5.5: The maximum required pitch curve.

We denote the pitch angle calculated from (5.30) as θ_{ach} because it is the achievable pitch angle when elevator deflection is commanded to its maximum value. As the vehicle's speed V becomes smaller, the achievable pitch angle becomes smaller as shown in Figure 5.6. The achievable pitch angle increase with the vehicle speed due to the Munk moment [63, pg. 56]:

$$M_{\text{munk}} = (m_z - m_x)V^2 \cos \alpha \sin \alpha \quad (5.31)$$

The Munk moment is destabilizing as it acts in the opposite direction of body restoring moment and hydrostatic righting moment. At high speed and a large angle of attack, the Munk moment becomes larger than the sum of body restoring moment and hydrostatic righting moment.

The minimum speed is found by equating (5.28) and (5.30). The concept is visualized through Figure 5.7, where θ_{\max_req} and θ_{ach} are plotted against speed. The minimum speed occurs at the intersection of the two curves. It occurs at the largest θ_{\max_req} that is achievable. By equating (5.28) and (5.30),

5.2 Minimum Speed and its Characteristics

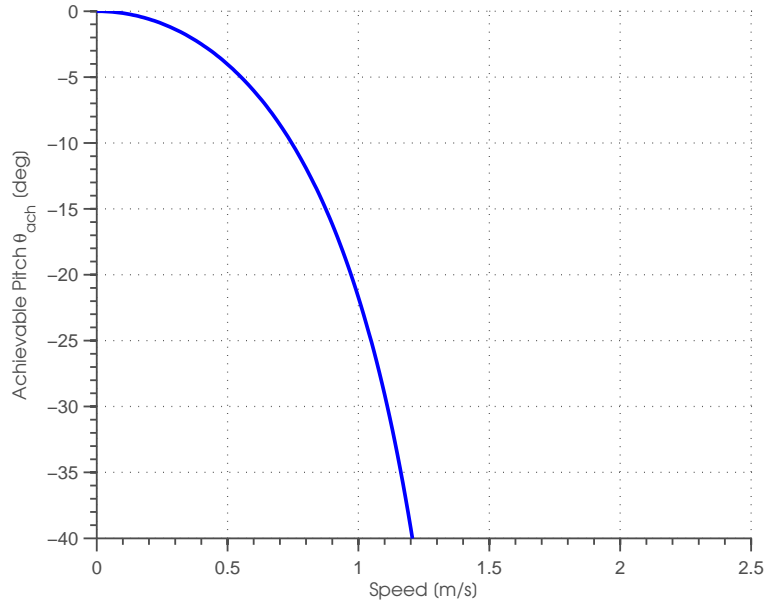


Figure 5.6: The achievable pitch curve.

we obtain

$$\frac{\frac{1}{2}\rho A_f x_f C_{L\delta} \delta_{\max} V^2}{z_{cg} F_w - [\frac{1}{2}\rho A_b L C_{m\alpha} + (m_z - m_x)] V^2} = \frac{F_B - F_w}{\frac{1}{2}\rho A_b (C_{L\alpha} + C_{D_0}) V^2} - \frac{A_f C_{L\delta} \delta_{\max}}{A_b (C_{L\alpha} + C_{D_0})} \quad (5.32)$$

Define the following variables:

$$\beta_1 = \frac{1}{2}\rho A_f x_f C_{L\delta} \delta_{\max} \quad (5.33)$$

$$\beta_2 = z_{cg} F_w \quad (5.34)$$

$$\beta_3 = \frac{1}{2}\rho A_b L C_{m\alpha} + (m_z - m_x) \quad (5.35)$$

$$\beta_4 = F_B - F_w \quad (5.36)$$

$$\beta_5 = \frac{1}{2}\rho A_b (C_{L\alpha} + C_{D_0}) \quad (5.37)$$

$$\beta_6 = \frac{A_f C_{L\delta} \delta_{\max}}{A_b (C_{L\alpha} + C_{D_0})} \quad (5.38)$$

5.2 Minimum Speed and its Characteristics

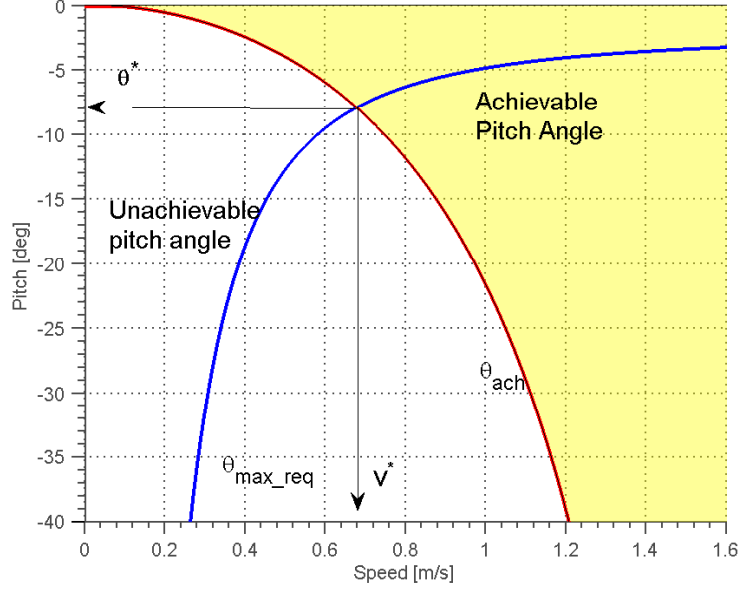


Figure 5.7: The minimum speed. Minimum speed is found at the intersection of the required pitch curve and achievable pitch curve.

and thus simplify (5.32) to

$$\frac{\beta_1 V^2}{\beta_2 - \beta_3 V^2} = \frac{\beta_4}{\beta_5 V^2} - \beta_6 \quad (5.39)$$

Then (5.39) is rewritten as a quadratic equation by treating V^2 as a variable:

$$V^4 + \frac{\beta_3 \beta_4 + \beta_2 \beta_5 \beta_6}{\beta_1 \beta_5 - \beta_3 \beta_5 \beta_6} V^2 - \frac{\beta_2 \beta_4}{\beta_1 \beta_5 - \beta_3 \beta_5 \beta_6} = 0 \quad (5.40)$$

Since the square of the minimum speed should be a real number, the discriminant of the quadratic equation need to be greater or equal to zero.

$$\left(\frac{\beta_3 \beta_4 + \beta_2 \beta_5 \beta_6}{\beta_1 \beta_5 - \beta_3 \beta_5 \beta_6} \right)^2 + 4 \left(\frac{\beta_2 \beta_4}{\beta_1 \beta_5 - \beta_3 \beta_5 \beta_6} \right) \geq 0 \quad (5.41)$$

5.2 Minimum Speed and its Characteristics

For a positive buoyant ($F_B > F_w$) AUV with center of gravity below the center of buoyancy ($z_{cg} > 0$), we have

$$\beta_2\beta_4 = z_{cg}F_w(F_B - F_w) > 0 \quad (5.42)$$

So, in order to fulfill (5.41) and has a finite minimum speed, we need to satisfy

$$\beta_1\beta_5 - \beta_3\beta_5\beta_6 > 0 \quad (5.43)$$

$$(5.44)$$

As $\beta_5 < 0$,

$$\beta_1 - \beta_3\beta_6 < 0 \quad (5.45)$$

By substituting the corresponding β_i , (5.45) becomes

$$\frac{1}{2}\rho A_f x_f C_{L_\delta} \delta_{\max} - \left[\frac{1}{2}\rho A_b L C_{m_\alpha} + (m_z - m_x) \right] \frac{A_f C_{L_\delta} \delta_{\max}}{A_b (C_{L_\alpha} + C_{D_0})} < 0 \quad (5.46)$$

Given $C_{L_\alpha} < 0$, $C_{D_0} < 0$, and ($m_z > m_x$) for slender AUV, we then obtain

$$C_{m_\alpha} > \frac{x_f}{L} (C_{L_\alpha} + C_{D_0}) - \frac{(m_z - m_x)}{\frac{1}{2}\rho A_b L} \quad (5.47)$$

By its definition of the body restoring moment, we know $C_{m_\alpha} < 0$. Finally, for the existence of minimum speed, it is required that

$$\frac{x_f}{L} (C_{L_\alpha} + C_{D_0}) - \frac{(m_z - m_x)}{\frac{1}{2}\rho A_b L} < C_{m_\alpha} < 0 \quad (5.48)$$

Figure 5.8 illustrates the non-existence of minimum speed when the inequality (5.48) is not satisfied. The θ_{ach} curve and the $\theta_{\text{max.req}}$ curve do not intersect one another even when the speed goes to infinity. It is because the restoring moment is too large that the AUV could not even pitch down at the required angle to maintain depth.

5.2 Minimum Speed and its Characteristics

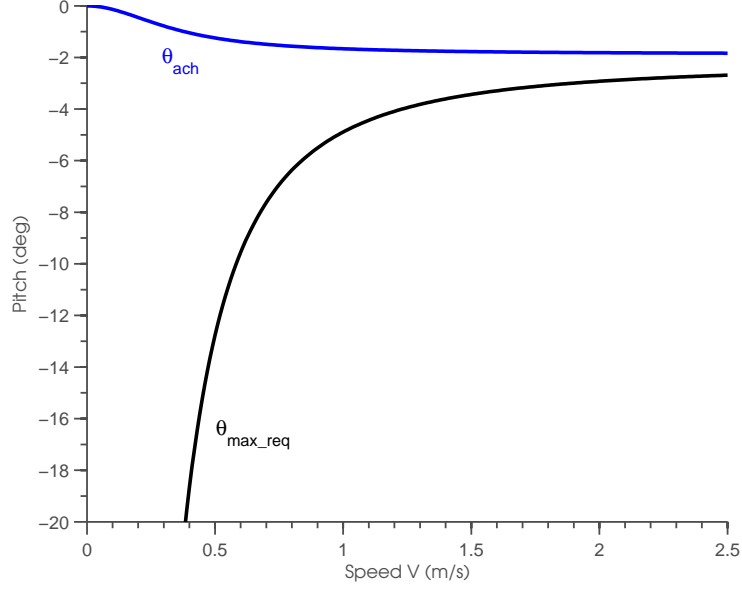


Figure 5.8: Non-existence of the minimum speed.

If the minimum speed exists, it can be calculated by solving the quadratic equation (5.40), so that

$$V_{\min}^2 = - \left(\frac{\beta_3\beta_4 + \beta_2\beta_5\beta_6}{2(\beta_1\beta_5 - \beta_3\beta_5\beta_6)} \right) \pm \sqrt{\left(\frac{\beta_3\beta_4 + \beta_2\beta_5\beta_6}{2(\beta_1\beta_5 - \beta_3\beta_5\beta_6)} \right)^2 + \left(\frac{\beta_2\beta_4}{(\beta_1\beta_5 - \beta_3\beta_5\beta_6)} \right)} \quad (5.49)$$

The solution consists of three important group of terms:

$$\beta_3\beta_4 + \beta_2\beta_5\beta_6 = \left(\frac{1}{2}\rho A_b L C_{m_\alpha} + (m_z - m_x) \right) (F_B - F_w) + \frac{1}{2}\rho z_{cg} F_w A_f C_{L_\delta} \delta_{\max} \quad (5.50)$$

$$\begin{aligned} \beta_1\beta_5 - \beta_3\beta_5\beta_6 &= \left(\frac{1}{2}\rho A_b (C_{L_\alpha} + C_{D_0}) \right) \left(\frac{1}{2}\rho A_f x_f C_{L_\delta} \delta_{\max} \right) \\ &\quad - \left(\frac{1}{2}\rho A_b L C_{m_\alpha} + (m_z - m_x) \right) \left(\frac{1}{2}\rho A_f C_{L_\delta} \delta_{\max} \right) \end{aligned} \quad (5.51)$$

$$\beta_2\beta_4 = z_{cg} F_w (F_B - F_w) \quad (5.52)$$

5.2 Minimum Speed and its Characteristics

The corresponding pitch angle at V_{\min} can be calculated by substitute V_{\min} into (5.28):

$$\theta^* = \frac{F_B - F_w}{\frac{1}{2}\rho A_b (C_{L_\alpha} + C_{D_0}) V_{\min}^2} - \frac{A_f C_{L_\delta} \delta_{\max}}{A_b (C_{L_\alpha} + C_{D_0})} \quad (5.53)$$

and the corresponding thrust force at V_{\min} is given by (5.25) as

$$F_t^* = -\frac{1}{2}\rho V_{\min}^2 A_b C_{D_0} \cos \theta^* \quad (5.54)$$

The minimum thrust ratio T_R^* is then given by substituting F_t^* into (5.16) and solving it:

$$F_t^* = 120(T_R^*)^2 - 31T_R^* - 0.53 \quad (5.55)$$

The following statements can be deduced from analyzing both the maximum required pitch curve and achievable pitch curve.

- The minimum speed is proportional to the buoyancy of the AUV. If the AUV is more buoyant, the minimum speed will increase. The buoyancy affects only the θ_{\max_req} curve as shown in Figure 5.9. The increase of minimum speed is coupled with the decrease of the pitch angle, θ^* .
- The minimum speed is proportional to the meta-centric height, z_{cg} . The greater the meta-centric height, the greater is the righting moment and thus, the higher the minimum speed. Meta-centric height affects only the θ_{ach} curve as shown in Figure 5.10. The increase of minimum speed is coupled with the increase of the pitch angle, θ^* .
- The minimum speed is *inversely* proportional to fin's effectiveness, $x_f A_f C_{L_\delta}$. The larger the x_f , A_f , and C_{L_δ} will reduce the minimum speed. Fin's effectiveness affects both the θ_{\max_req} curve and θ_{ach} as shown in Figure 5.11. The reduction of minimum speed is coupled with the decrease of the pitch angle, θ^* .
- It is also noticed that the minimum speed is independent of the viscous drag coefficient (M_q) and moment of inertia (J_y).

5.2 Minimum Speed and its Characteristics

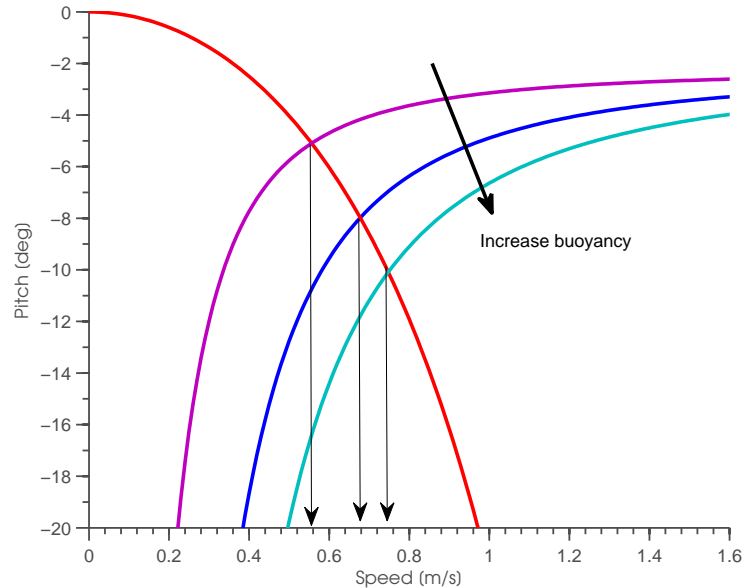


Figure 5.9: Effect of buoyancy on minimum speed.

In practice, one could reduce the minimum speed of an AUV by reducing the buoyancy, and the meta-centric height, or by increasing the fin's effectiveness. From the analysis, manipulating the buoyancy is a better option because the reduction of the minimum speed by means of buoyancy is coupled with the smaller pitch down angle. On the contrary, reduction of minimum speed by means of meta-centric height or fin's effectiveness is coupled with bigger pitch down angle, which is undesirable due to a larger drag.

In reality, there are physical constraints on how much one can manipulate buoyancy, meta-centric height and the fin's effectiveness. For example, buoyancy cannot be reduced to zero, as the AUV needs to float to the surface for easy recovery under power failure or other emergency conditions. The meta-centric height is needed to make sure that the AUV is always upright, and to keep the roll of AUV small. It is to be noted that when one factor is changed, the rest of the factors might be affected simultaneously. For instance, changing the buoyancy of the AUV by adding weight might affect the meta-centric height concurrently.

5.2 Minimum Speed and its Characteristics

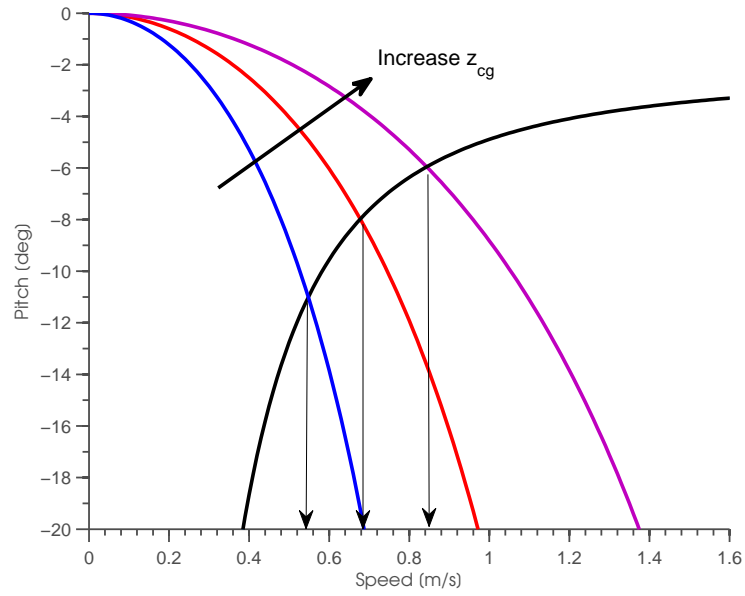


Figure 5.10: Effect of meta-centric height on the minimum speed.

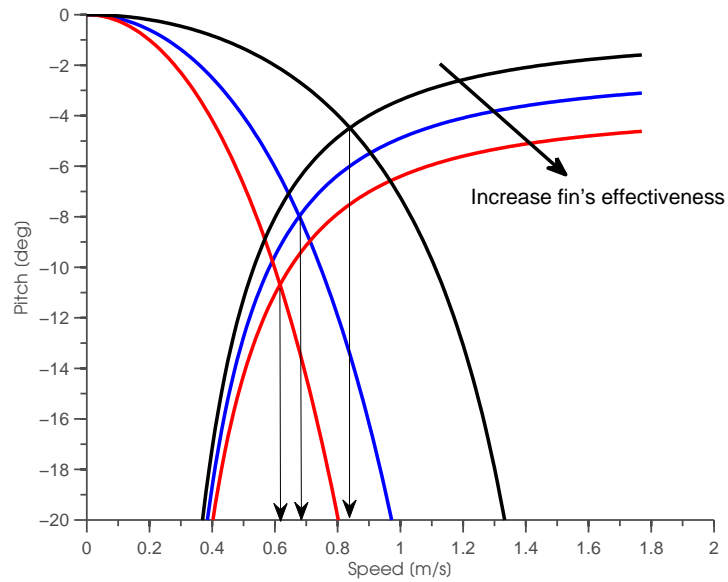


Figure 5.11: Effect of fin's effectiveness on the minimum speed.

5.2 Minimum Speed and its Characteristics

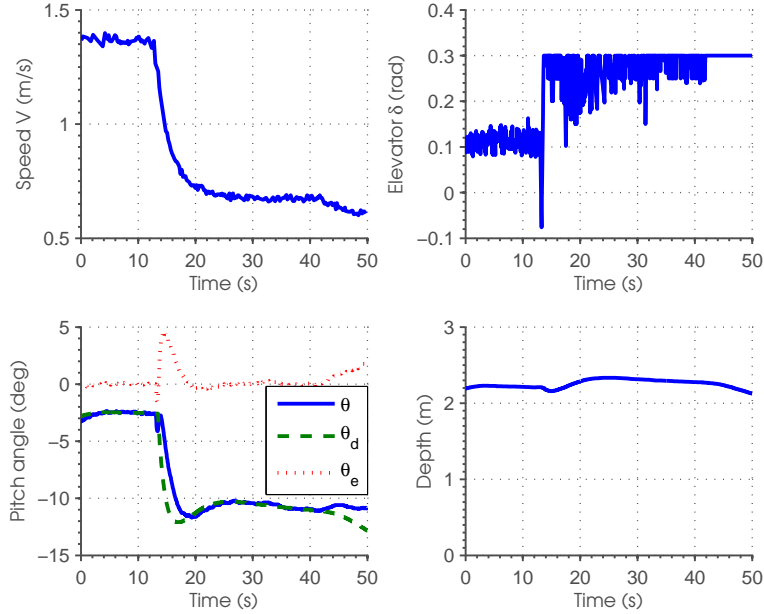


Figure 5.12: Characteristic of losing pitch-controllability. From 40 s onwards, the pitch response deviated from the desired pitch and the elevator became saturated.

5.2.2 Characteristic of losing pitch-controllability

An experiment was conducted to investigate the phenomenon of losing pitch-controllability when the AUV's speed drops below its minimum speed. There were three stages in this experiment (see Figure 5.12):

- Stage 1 ($0 s \leq t < 12 s$): The AUV was driven at a speed of $u_0 = 1.4$ m/s until it reached a depth of 2 m.
- Stage 2 ($12 s \leq t < 40 s$): The speed was reduced gradually up to a point just before the AUV lost its pitch-controllability.
- Stage 3 ($t \geq 40 s$): The speed was reduced beyond its minimum speed, causing the AUV to lose its pitch-controllability.

Consider the transition between Stage 2 and Stage 3. From the pitch response in Stage 2, it is observed that the pitch response followed the desired pitch angle θ_d closely and the pitch error² θ_e was close to zero. In Stage 3,

²pitch error $\theta_e \doteq \theta - \theta_d$.

5.3 Minimum Speed Seeking Algorithm

the pitch error grew significantly, indicating the loss of pitch-controllability as the pitch response deviated from the desired pitch. In the elevator plot from Stage 2 to Stage 3, it is observed that the elevator was becoming saturated at its maximum value. In the depth response plot, it is observed that the AUV was losing depth gradually, but its effect was not as fast and significant as seen in the pitch response plot. In summary, it is observed that when the AUV was losing its pitch-controllability, the pitch response deviated from the desired pitch and the elevator became saturated.

5.3 Minimum Speed Seeking Algorithm

In this section, we discuss the minimum speed seeking algorithm under the framework of Extremum Seeking (ES) [64]. There is difficulty in applying the existing methods in ES to solve the minimum speed problem. The problem violates important assumptions that the steady state characteristic of the plant be well defined and stable, regardless of the input parameter. We relax these assumptions by introducing a new definition of steady state mapping which imposes a new structure on the seeking algorithm. This leads naturally to the detailed discussion on the proposed seeking algorithm in Section 5.3.2.

5.3.1 Extremum Seeking

The minimum speed seeking problem could be studied under the framework of Extremum Seeking (ES). Typically, ES is employed to find the optimal operating condition for industrial processes to produce better outcomes, productivity or yield. The optimal operating condition is not known analytically or might change with time. Hence, optimization has to be performed online to search for the optimal point by making use of real-time measurement of the actual process [65].

We describe a typical extremum seeking problem using a single-input single-output system as shown in Figure 5.13. The dynamic plant has a real value input parameter, denoted by $\tau \in \mathfrak{R}$. For any fixed τ , the system converges to a steady state uniquely determined by τ . In other words, under

5.3 Minimum Speed Seeking Algorithm

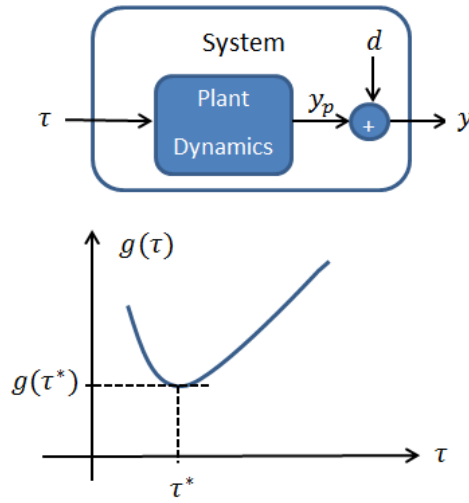


Figure 5.13: Input-output system with a steady state map.

a fixed input, the cost output $y_p = h(x)$, as a function of system state x , converges to a constant value. In this case, a function $g : \mathfrak{R} \rightarrow \mathfrak{R}$, given as a limit

$$g(\tau) := \lim_{t \rightarrow \infty} y_p(t) \Big|_{\text{input fixed at } \tau} \quad (5.56)$$

is well defined and this function $g(\cdot)$ is called a *readout* map [66]. The goal of extremum seeking is to drive the input/output pair from the initial $(\tau_0, g(\tau_0))$ to the optimal $(\tau^*, g(\tau^*))$ given measurements of input τ and output $y = y_p + d$, where d is a bounded disturbance. Starting from some initial values, the ES algorithm modifies the input parameter, monitors the plant's response to obtain the gradient of $g(\tau)$, and then adjusts the parameter towards the optimal point. The most popular scheme of ES is the method of sinusoidal perturbation where the input parameter is perturbed and updated continuously. Alternatively, the input parameter could be updated in a discrete manner. A step change is made on the parameter, and then the algorithm takes some time to measure the steady state response before another step change. The stability proof of the first and second methods is given in [67] and [66] respectively.

Unfortunately, the stability analysis requires the system to be locally

5.3 Minimum Speed Seeking Algorithm

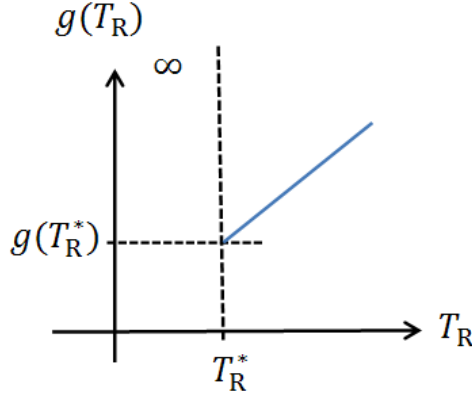


Figure 5.14: Readout map for $g(T_R)$. The *readout* map is not well defined for inputs less than T_R^* .

exponentially stable for every point in the *readout* map. Specifically, the input parameter in our study is the AUV thrust, and there exists a range of thrusts³ that will cause the AUV to lose controllability and become unstable. Define

$$y_p = T_R + k\theta_e, \quad (5.57)$$

where k is a positive constant and the negative value of pitch error θ_e is truncated to zero so that $\theta_e \geq 0$. Then

$$g(T_R) := \lim_{t \rightarrow \infty} [T_R(t) + k\theta_e(t)] \Big|_{\text{input fixed at } T_R} \quad (5.58)$$

will result in a *readout* map as shown in Figure 5.14. This is because

$$\lim_{t \rightarrow \infty} \theta_e(t) \Big|_{\text{input fixed at } T_R < T_R^*} = +\infty, \quad (5.59)$$

and

$$\lim_{t \rightarrow \infty} \theta_e(t) \Big|_{\text{input fixed at } T_R \geq T_R^*} \approx 0. \quad (5.60)$$

The *readout* map in Figure 5.14 is not well defined and is unstable for inputs

³All values of thrust that have corresponding speeds less than the minimum speed.

5.3 Minimum Speed Seeking Algorithm

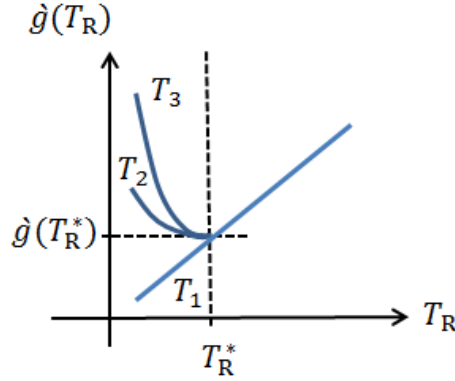


Figure 5.15: Readout map for $\dot{g}(T_R)$. A change in the definition of $g(\cdot)$ results in a well defined *readout* map.

less than T_R^* . Since the required assumptions are violated, the stability of existing ES methods is not guaranteed. However, a change in the definition of $g(\cdot)$ could result in a well defined and stable *readout* map. Instead of letting time go to infinity, define $g(\cdot)$ by having the time approach a finite value T , where $0 < T < \infty$. To uniquely determine the value of such a definition, the value of the input parameter at time $t = 0$ needs to be fixed. We choose that value to be T_R^* . So, we have

$$\dot{g}(T_R) := \lim_{t \rightarrow T} [T_R(t) + k\theta_e(t)] \Big|_{\text{input fixed at } T_R, \text{ and at } t = 0, T_R = T_R^*}. \quad (5.61)$$

Figure 5.15 shows the plot of $\dot{g}(\cdot)$ for $T = T_1, T_2$, and T_3 where $T_1 < T_2 < T_3$. At time $t = 0$, T_R is equal to T_R^* and thus the pitch error $\theta_e(0) \approx 0$. For the case of $T = T_1 \rightarrow 0^+$, there is no time for the pitch error to grow even though $T_R < T_R^*$. Hence $\dot{g}(T_R) = T_R$. The larger the value of T , the more time there is for the pitch error to grow and if $T \rightarrow \infty$, then $\dot{g}(T_R)$ is equivalent to the original definition of $g(T_R)$. In summary, we are able to construct a well defined and stable *readout* map by selecting a proper value of T . The definition of $\dot{g}(T_R)$ requires $T_R = T_R^*$ at $t = 0$ but the value of T_R^* is not known. This requirement can however be fulfilled by performing the following steps. First, discretize the solution space of T_R into a finite number of possible points separated by a constant step size, Δ_T . If the step size is small enough, it is reasonable to assume that T_R^* is equal to a particular point. Then start the

5.3 Minimum Speed Seeking Algorithm

search from an initial $T_R(0)$, where $T_R(0) > T_R^*$, and make Δ_T change to T_R at every iteration. Each iteration is time-separated by a seeking period T . Such a seeking method will ensure that $T_R = T_R^*$ before entering the region of $T_R < T_R^*$. Hence, by restricting the search to a small step at every interval of properly selected T , the unstable map (Figure 5.14) can be transformed to a stable one (Figure 5.15).

Before describing the seeking algorithm in Section 5.3.2, the problem is first posed formally. The task of the minimum speed seeking algorithm is: given real-time measurement of pitch error θ_e and elevator δ_s , force the solution of the closed-loop AUV depth subsystem (Figure 5.4) to eventually converge to the optimal states where $V = V_{\min}$ from (5.49) and $\theta = \theta^*$ from (5.53) by manipulating the thrust ratio T_R , and to do so without any precise knowledge of the AUV depth subsystem and the optimal states.

The algorithm resides in the minimum speed seeking subsystem, which augments the AUV depth subsystem by changing the thrust ratio, such that the AUV cruises as slowly as possible while maintaining the desired depth (see Figure 5.16). It is assumed that when the minimum speed seeking algorithm is turned on, the AUV depth subsystem has already reached steady state at the desired depth and is cruising at a certain speed larger than the minimum speed.

5.3.2 Seeking Algorithm

Figure 5.17 illustrates how the seeking algorithm determines the output T_R based on two inputs θ_e and δ_s . A Fuzzy Inference System (FIS) is used to map the two inputs to three decisions: to keep the current T_R , to increase or to decrease the current T_R by a constant step gain Δ_T . Mathematically, the algorithm can be described as follows:

At every seeking interval k (each interval is separated by seeking period T_S), the thrust ratio is determined by

$$T_R(k) = T_R(k-1) + \Delta T_R, \quad k = 1, 2, 3, \dots \quad (5.62)$$

5.3 Minimum Speed Seeking Algorithm

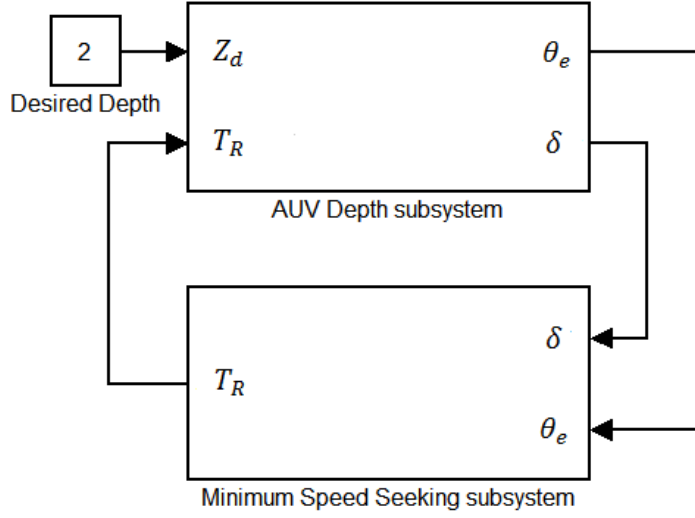


Figure 5.16: Problem formulation. The block diagram shows the interaction between the AUV Depth Subsystem and Minimum Speed Seeking Subsystem. The minimum speed seeking subsystem sends thrust command to the AUV depth subsystem and receives pitch error θ_e and elevator deflection δ_s in return.

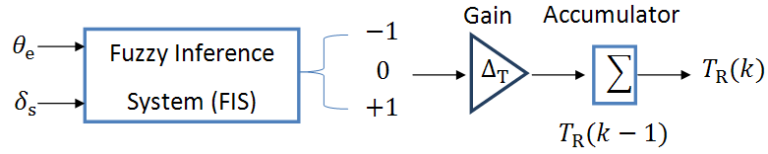


Figure 5.17: Block diagram of seeking loop. Fuzzy Inference System determines whether to maintain, decrease or increase T_R by a constant step gain Δ_T based on two inputs, θ_e and δ_s at every seeking interval.

where

$$\Delta T_R = \begin{cases} -\Delta_T & \text{if FIS output} = -1 \\ 0 & \text{if FIS output} = 0 \\ +\Delta_T & \text{if FIS output} = +1 \end{cases} \quad (5.63)$$

The seeking algorithm starts to search from an initial thrust ratio $T_R(0)$, a nominal thrust ratio that the AUV normally operates at. It is obvious that

5.3 Minimum Speed Seeking Algorithm

$T_R(0)$ is greater than T_R^* .

The period of the seeking loop, denoted by T_s determines how frequent T_R is changed. The searching algorithm should run at a much slower rate in order to achieve time-scale separation between the nonlinear system dynamics and the seeking loop. This is because the seeking algorithm assumes that the dynamic system functions as a static map, which can be justified only if the time between the change in input parameter is sufficiently long compared to the dynamics of the system. However, T_s also cannot be too large. The seeking algorithm should react fast enough to bring T_R out of the unstable region ($T_R < T_R^*$), or else θ_e may grow unbounded.

From (5.62), the algorithm generates a new thrust ratio $T_R(k)$ recursively by adding Δ_T , 0 or $-\Delta_T$ to the previous thrust ratio $T_R(k-1)$. In other words, the thrust ratio is restricted by the maximum change of Δ_T per iteration. As the algorithm drives a dynamical system, a large step will cause a large transient, which is undesirable. By having a known constant step change of thrust ratio Δ_T , there is better control over the time taken for the transient to fade. Furthermore, Δ_T will determine the resolution of the solution by dividing the whole solution space with a step size of Δ_T .

5.3.2.1 Fuzzy inference system (FIS)

The fuzzy inference system is chosen because it is a universal mapping tool that allows incorporation of the expert's knowledge via its *If-Then* rules. In this study, the FIS is designed as a switching control system where it only yields three crisp output levels for all input values. This is done by using the *Mamdani-type* fuzzy inference system with the Largest of Maximum (LOM) defuzzification method. The design of such a switching control system using fuzzy set theory is discussed in [68].

In this section, we discuss mainly how to determine a set of fuzzy rules, design the input and output membership functions and the resulting input-output mapping. For more information on FIS, one could refer to [69].

As discussed in Section 5.2.2, when the AUV travels below its minimum speed, the pitch response deviates from the desired pitch and the elevator

5.3 Minimum Speed Seeking Algorithm

becomes saturated. Therefore, as long as the elevator is not saturated, T_R could be decreased. When the elevator is saturated and the pitch error is small, it is desirable to keep the current T_R . However, when the elevator is saturated and the pitch error is big, T_R should be increased. The above knowledge is translated to the following fuzzy rules:

1. If (δ is *NotSaturated*) then (Δ_T is *decreased*).
2. If (θ_e is *Small*) and (δ_s is *Saturated*) then (Δ_T is *kept*).
3. If (θ_e is *Big*) and (δ_s is *Saturated*) then (Δ_T is *increased*).

Figure 5.18 illustrates the active region of each fuzzy rule in the *readout* map. When $T_R \gg T_R^*$, this belongs to the *blue* region and δ_s is far from saturation. Hence, *rule 1* is active and T_R is decreased. When $T_R < T_R^*$, this belongs to the *red* region and δ_s should become saturated, and θ_e starts to grow significantly. Then *rule 3* is activated and T_R is increased. Apparently, *rule 1* and *rule 3* together will force T_R into the *green* region, where *rule 2* is active and T_R is kept unchanged. In practice, T_R^* is changing with time when the AUV is subjected to the disturbance. The cost-driven algorithm will try to track T_R^* by changing T_R continuously and causing T_R to oscillate. In contrast, the proposed algorithm will operate the AUV at a constant T_R that is slightly larger than T_R^* , which is a more desirable behavior.

If we know only the fin saturation without the knowledge of pitch error, we could construct two rules: decrease the T_R when fin is not saturated, and increase the T_R when fin is saturated. This will cause the green region R2 to disappear from Figure 5.18. In this circumstance, the T_R is never kept at a constant value, but will oscillate around the T_R^* and forming a limit cycle, which will affect the controller performance of the AUV. On the other hand, one could keep the T_R constant when fin is saturated, instead of increase the T_R . In this construction, the seeking algorithm will lost its ability to increase T_R when conditions are not favorable such as the AUV encounter a lager disturbance or increase of buoyancy. These are the reasons why the knowledge of pitch error is useful in the algorithm.

5.3 Minimum Speed Seeking Algorithm

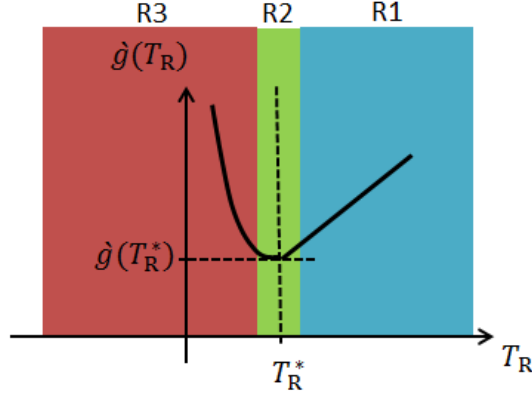


Figure 5.18: Fuzzy Rules and the *readout* map.

Next, all the linguistic terms that are used in the rules need to be defined via membership functions. Two fuzzy sets are used for each input as shown in Figure 5.19. The membership functions of pitch error are characterized by the pitch error threshold θ_e^{TS} which determines the intersection of the two fuzzy sets. For $\theta_e < \theta_e^{\text{TS}}$, the error is considered relatively *Small* and acceptable; otherwise it is considered as *Big*. Note that θ_e is considered small when it is negative. The AUV speed needs to be increased when more downward pitching is required (when θ_e is positive). With the increase of speed, the elevator will gain more control authority to close the pitch error gap. On the other hand, when the AUV is pitching down too much (θ_e is negative), there is no need to increase the speed, as the gap can be closed by reducing the elevator deflection. The pitch error threshold θ_e^{TS} is obtained by examining the usual bound of the pitch error during normal AUV maneuvers. One example is given in Figure 5.20 showing the pitch error changing within a range of 0.01 rad.

Based on the second input δ_s , it is of interest to know how close the elevator is to saturation. The intersection between *Saturated* sets and *NotSaturated* sets is determined by subtracting the elevator fin budget, δ_{FB} from the maximum elevator angle δ_{max} . The fin budget δ_{FB} is allocated such that there is enough control authority for the elevator to overcome the environmental disturbance and to keep the pitch at the desired pitch angle. One can select

5.3 Minimum Speed Seeking Algorithm

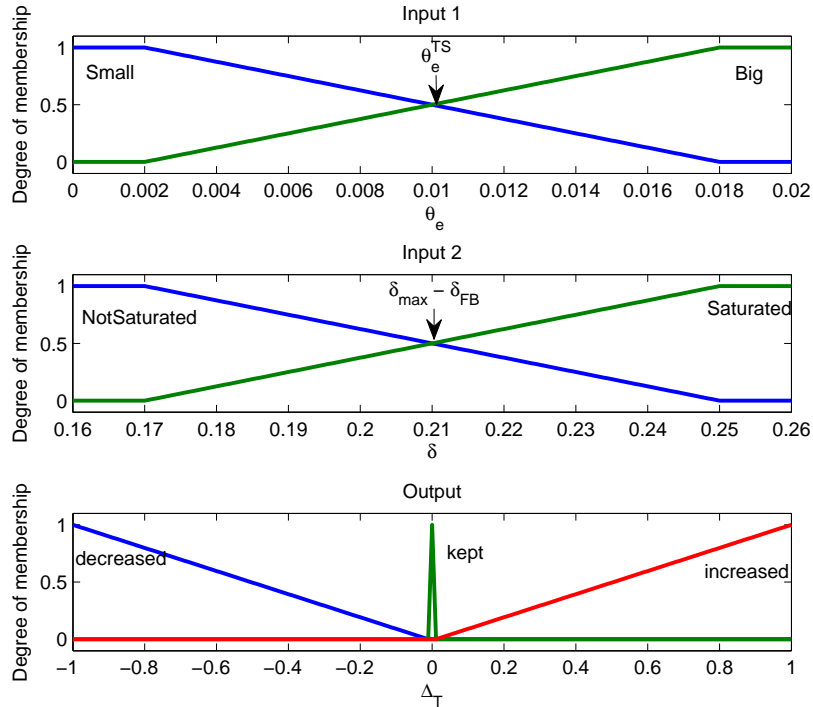


Figure 5.19: Membership functions of the two inputs and one output. The membership functions of the two inputs, θ_e and δ are characterized by θ_e^{TS} and δ_{FB} respectively. We use triangular or trapezoidal shapes as the type of membership function because they are simple to implement and fast for computation

δ_{FB} based on past experiments by looking at the range of the elevator within which the depth is maintained. One example is given in Figure 5.20 showing the elevator changing within a range of 0.05 rad.

The output consists of three fuzzy sets: *decreased*, *kept* and *increased* corresponding to values -1 , 0 and 1 respectively as shown in Figure 5.19. The design of such an output membership function together with the LOM defuzzification method restricts the output value to three levels similar to a bang-off-bang controller output. This is best illustrated by the output surface map (Figure 5.21). The output surface has only three distinct colors: red for 1 , green for 0 and blue for -1 . The output surface map shows that the seeking algorithm will reduce T_R whenever δ_s is not saturated and θ_e is small (blue region). Reduction in T_R will cause δ_s to become saturated eventually.

5.3 Minimum Speed Seeking Algorithm

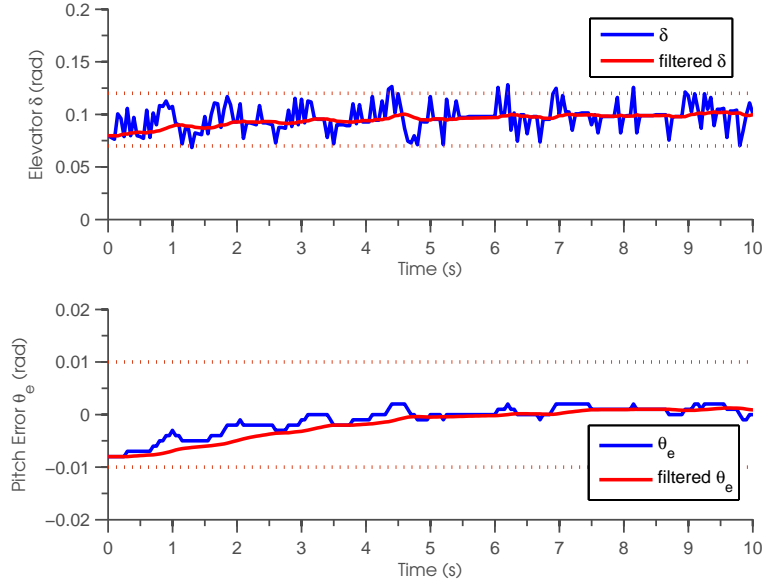


Figure 5.20: A snapshot of steady state elevator and pitch error when the AUV is operating under nominal thrust. This figure is the zoom-in of the first 10 s of Figure 5.12. The top figure shows the elevator operating within the range of 0.07-0.12 rad which leads to the assignment of $\delta_{\text{FB}} = 0.05$ rad. The bottom graph shows the corresponding pitch error which leads to the assignment of $\theta_e^{\text{TS}} = 0.01$ rad. The figure also shows how the filter smooths θ_e and removes the spikes in δ_s .

If δ_s is saturated and θ_e is small (green region), T_R will be kept. If the AUV experiences a disturbance that is larger than expected, θ_e will become large. The current T_R is not sufficient to overcome the disturbance and thus T_R needs to be increased (red region). When the disturbance fades away, the vehicle goes back to the blue region. Then the seeking algorithm will reduce T_R until the green region is reached again.

5.3.2.2 Filtering

Both elevator δ_s and pitch error θ_e are filtered using a low pass filter [70] of the following form:

$$y(n) = (1 - r)x(n) + ry(n - 1), \quad 0 < r < 1, \quad r = \exp(-1/d) \quad (5.64)$$

5.4 Simulation Results

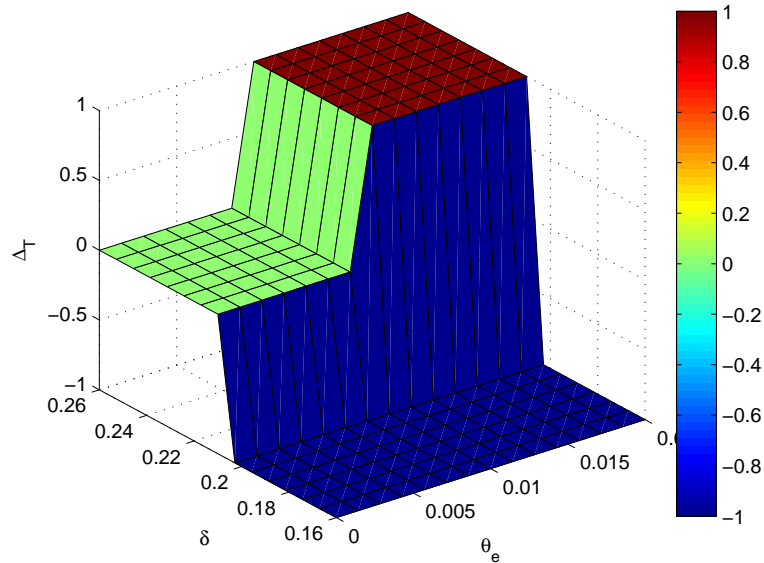


Figure 5.21: Output surface map of the Fuzzy Inference System. The plot displays the dependency of the output Δ_T on the two inputs: pitch error θ_e , and elevator deflection δ .

where y is the filtered output, x is the input and d is the filter time constant. In the actual implementation, filtering is performed in the AUV depth subsystem, which runs at 20 Hz, before the data is fed into the minimum speed seeking subsystem. r is chosen as 0.95 which corresponds to $d \approx 20$ samples, equivalent to $T_S = 1$ s. As shown in Figure 5.20, the signals are filtered to average out the measurement noise and to remove spikes.

5.4 Simulation Results

A simulation model was built in Matlab/Simulink environment based on the AUV depth subsystem described in Section 5.1, and the minimum speed seeking subsystem described in Section 5.3. The two main objectives of performing the simulation are:

- The theoretical minimum speed is known in simulation. It is of interest to find out via simulation how close the seeking algorithm approaches the minimum speed.

5.4 Simulation Results

- Simulation allows trials of different sets of design parameters rapidly, hence enabling the study of the impact of individual design parameters on the seeking performance.

All relevant parameters used in the simulation are listed in Table 5.1.

Table 5.1: Simulation parameters

Design			Initial			Controller		
Parameters	Value	Units	Parameters	Value	Units	Parameters	Value	Units
θ_e^{Ts}	0.01	rad	$T_R(0)$	0.7	-	K_{pz}	-0.15	rad/m
δ_{FB}	0.05	rad	Z_0	2	m	K_{iz}	-0.01	rad/m
T_S	1	s	θ_0, α_0, q_0	0	rad, rad/s	$K_{p\theta}$	-20	-
Δ_T	0.01	-	V_0	1.4	m/s	$K_{i\theta}$	-0.1	-
Model			Model			Hydrodynamics		
Parameters	Value	Units	Parameters	Value	Units	Parameters	Value	Units
ρ	1000	kgm ⁻³	J_y	40	kgm ²	C_{D_0}	-1.2	-
m	66	kg	z_{cg}	0.01	m	$C_{L\alpha}$	-1.5	-
m_x	70.2	kg	x_{cg}	0	m	$C_{L\delta}$	-0.3	-
m_z	128.8	kg	A_b	0.0314	m ²	$C_{M\alpha}$	-1.8	-
F_w	647.5	N	A_f	0.0431	m ²	C_{Mq}	-0.8	-
F_B	649.4	N	L	2	m	δ_{max}	0.26	rad
g	9.81	ms ⁻²	x_f	1	m			

Figure 5.22 shows the trajectory of the simulated thrust and speed with respect to time. Initially, the AUV is commanded to thrust at 0.70 until 100 s, which is when the seeking algorithm is turned on. The thrust ratio is reduced to 0.44, which is very close to the optimal thrust ratio ($T_R^* = 0.433$ from (5.55)). The thrust ratio takes 50 s to settle down despite a small fluctuation seen in the transition stage. A similar response is seen in the speed, where it settles down to 0.69 m/s, just above the minimum speed ($V_{min} = 0.678$ m/s).

Figure 5.23 illustrates how the output of the FIS is driven by the two inputs, δ_s and θ_e . Initially, since δ_s is not saturated, T_R is reduced. In order to maintain its depth, the AUV needs more downward pitching when the speed is reduced consecutively from 100 s to 130 s. θ_d decreases faster than θ , causing θ_e to grow. At the interval 131 s-139 s, T_R is increased for nine consecutive steps. Then, θ_e becomes smaller as the pitch response manages to catch up with the desired pitch. T_R is reduced from 0.49 back to 0.44 and

5.4 Simulation Results

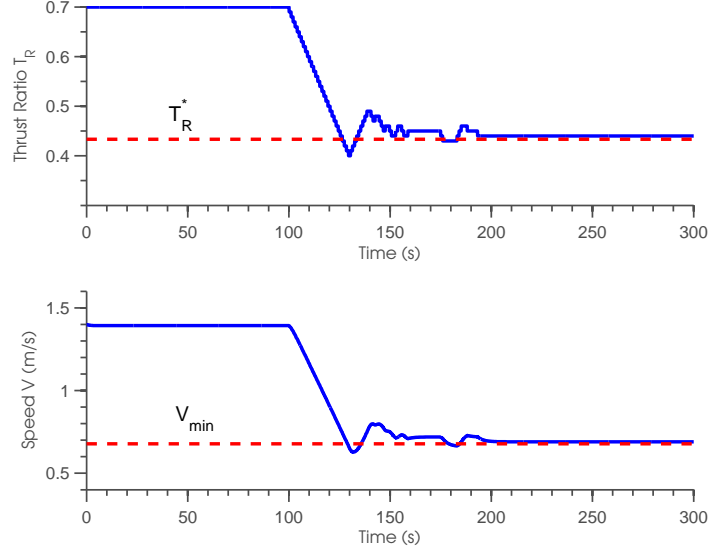


Figure 5.22: Simulated thrust ratio and speed.

stable after 50 s.

As shown in Figure 5.24, to maintain its depth, the AUV needs to pitch at -1.4 deg when cruising at 1.4 m/s. While the speed is reduced, the pitch angle decreases and settles down to -7.8 deg. There is a small oscillation in pitch seen in the transition stage, but in general the pitch response follows the desired pitch closely. The depth is kept at the desired value of 2 m throughout the entire period despite small oscillations during the transition stage.

The minimum speed that can be attained by the seeking algorithm depends on the allocated fin budget δ_{FB} (see Figure 5.25). The smaller the fin budget, the closer the attainable minimum speed approaches the minimum speed V_{min} , but this is achieved at the expense of robustness against disturbance. In practice, the disturbance always exists; if there is not enough fin budget to overcome the disturbance, fuzzy *rule 3* will be triggered periodically, causing T_R to oscillate. Hence, the selection of the fin budget is a trade-off between optimality and robustness.

Figure 5.26 shows the convergence of thrust ratio corresponding to different seeking periods T_S . The seeking period determines how frequent the seeking algorithm is executed. In order to achieve time-scale separation between the

5.4 Simulation Results

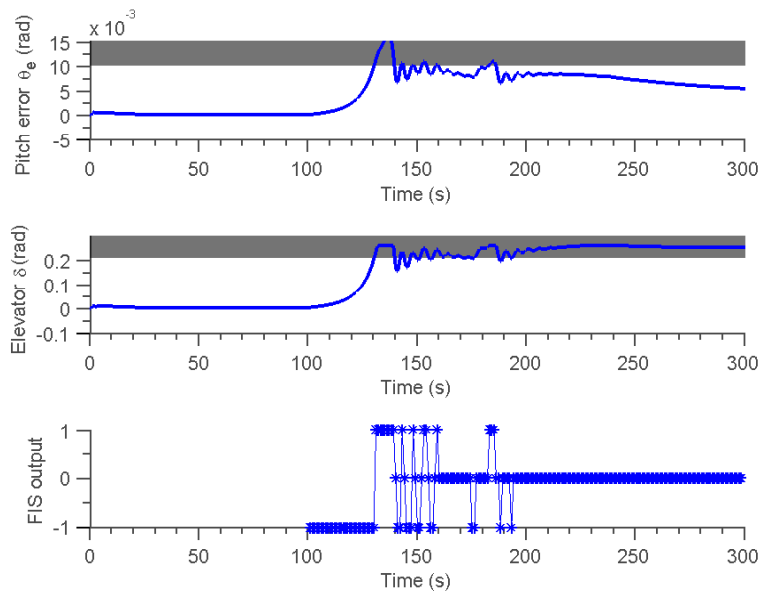


Figure 5.23: Simulated elevator and pitch error and the corresponding FIS output.

pitch dynamics and the seeking dynamics, T_S has to be many times larger than the time constant of pitch dynamics. The simulation results show that the seeking algorithm is unstable for $T_S = 0.5$ s, which causes bounded oscillation of the thrust ratio. As T_S is increased, the response becomes more stable but the convergence time is longer. $T_S = 1$ s is ideal as it strikes a balance between stability and convergence time. In addition, the results show that the choice of T_S does not affect the optimality.

5.4 Simulation Results

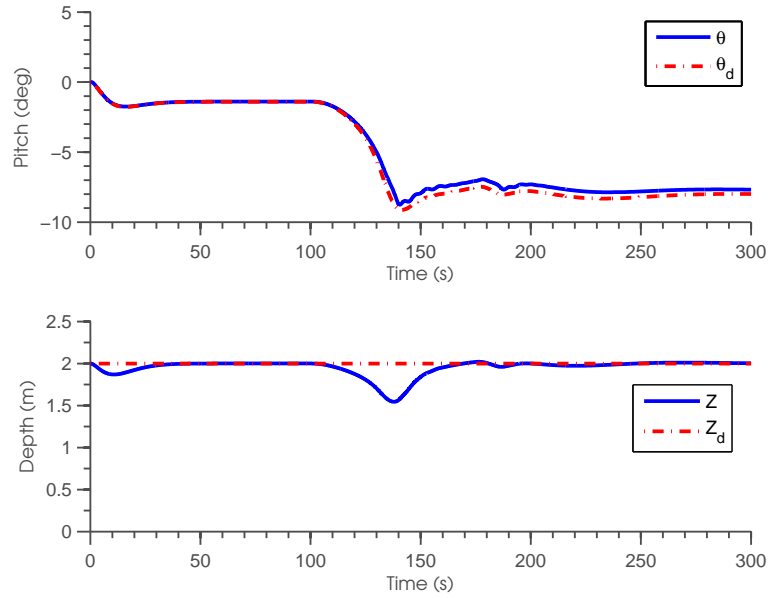


Figure 5.24: Simulated pitch and depth responses.

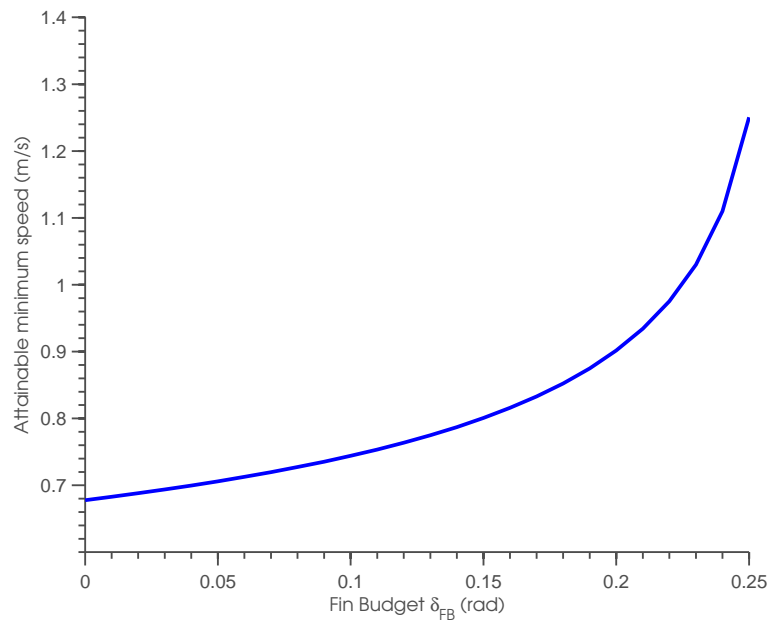


Figure 5.25: Attainable minimum speed versus allocated fin budget.

5.4 Simulation Results

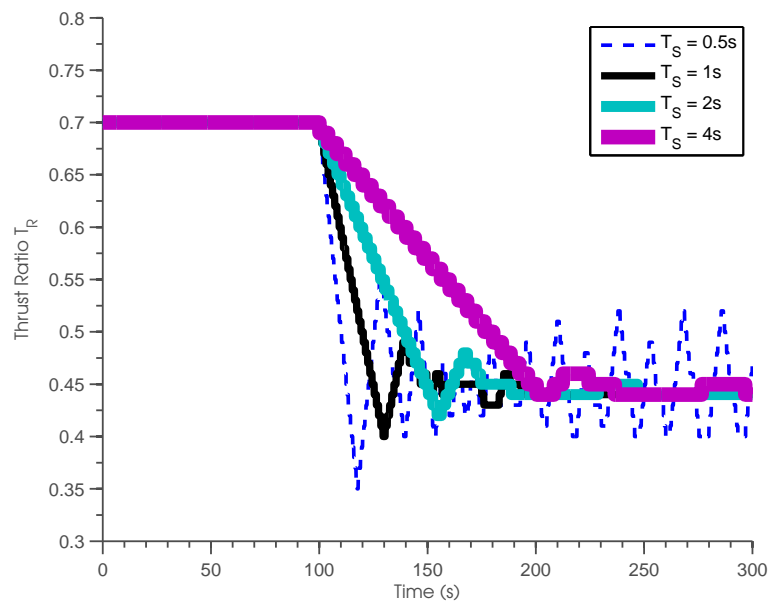


Figure 5.26: Convergence of thrust ratio for different seeking periods T_S .

5.5 Experiment Results

In this section, we verify the minimum speed seeking algorithm via field experiments conducted in both the lake and sea environment. First, we start with the lake experiments where the water is considered static and the underwater disturbance is relatively small. As there is no underwater current, the AUV speed relative to the surrounding water is equal to its ground speed, which is measured by the DVL. Compared to experiments in the lake, the experiments conducted at the sea, especially in the case of shallow water, belong to the other extreme. The AUV is subjected to waves, tides, weather conditions, air and water interactions, and commercial and recreational navigations when operating in the shallow water region [71]. Therefore, the lake experiments allow us to investigate the performance of the algorithm without worrying about the effects of the disturbance, while the sea experiments provide a real test on the robustness of the algorithm.

5.5.1 Lake Experiments

The lake experiments were conducted at Pandan Reservoir⁴ with the *STAR-FISH* AUV, equipped with DVL and an in-situ water particle sensing payload.

Figure 5.27 shows the trajectory of the thrust and speed with respect to time. Initially, the AUV was commanded to cruise at a speed of 1.4 m/s until the seeking algorithm was turned on at 50 s. The thrust ratio was reduced gradually to 0.47 from 0.70. A small transient of T_R was seen in the transition stage. However, the fluctuation was so small that it did not affect the speed, which settled down to 0.75 m/s in 23 s. We observed the same behavior when we compare the experimental results with the simulated ones. The thrust ratio reduced gradually to a minimum point, followed by a small increase, and settled down quickly thereafter. This similarity gives a very strong assurance to the model, in the sense that the characteristic of the dynamics is modeled correctly although the model parameters are not known precisely.

The fact that the thrust ratio settles down to a constant is an appealing

⁴Pandan Reservoir is located in the western region of Singapore.

5.5 Experiment Results

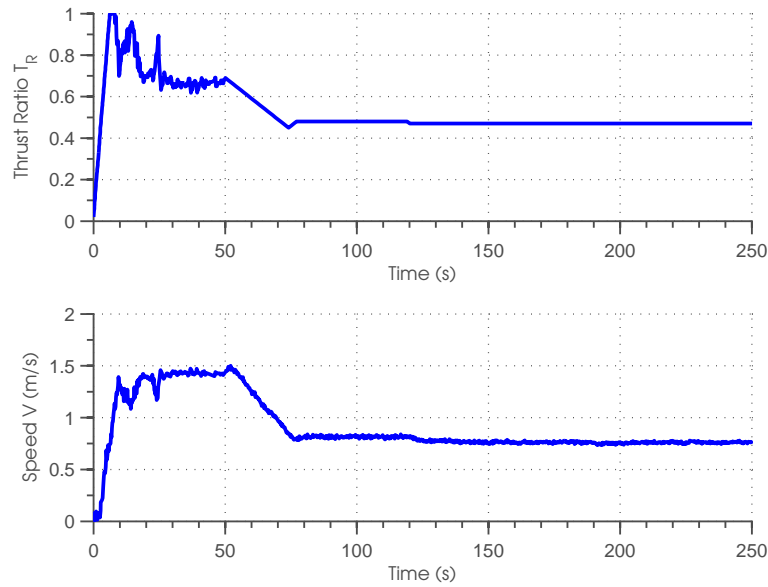


Figure 5.27: Lake experiment: thrust ratio and speed.

feature because this results in a constant speed operation. The settling down of the thrust ratio is not due to the termination of the seeking algorithm. In fact, the algorithm is still active and will modify the thrust ratio if there is any change in the operating condition. For example, if the AUV experiences a sudden disturbance that affects the pitch error, its speed will be increased to generate more lift to overcome the disturbance. When the disturbance fades away, the seeking algorithm will bring back the thrust ratio to its minimum again.

The *STARFISH* AUV is normally operated at a nominal thrust ratio of 0.70, which requires a thrust power of 145 W. If the thrust ratio is reduced to 0.47, the thrust power will be reduced to 43 W, giving a savings of 102 W. If we have 1 kW hour of battery energy for propulsion, traveling at $T_R = 0.47$ instead of 0.70 will increase the vehicle's endurance from 7 hours to 23 hours.⁵

Figure 5.28 illustrates how the elevator and pitch error evolved with time, and the corresponding FIS output. The data was logged in the seeking algorithm and only available from 50 s onwards. Both the inputs and the FIS

⁵For illustration purpose only; the hotel load is not included in the calculation.

5.5 Experiment Results

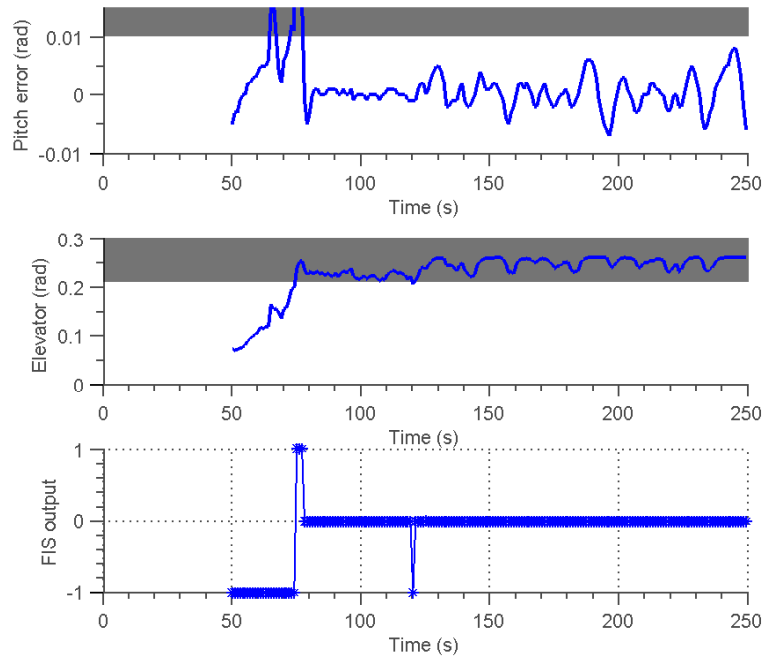


Figure 5.28: Lake experiment: elevator and pitch error.

output exhibited similar response to their simulated counterparts. However, since the AUV experienced disturbance in the real world environment, the pitch error fluctuated even after the speed has settled down. As a result, the elevator changed rapidly to overcome the disturbance and to keep the pitch error small. Enough fin budget needs to be allocated to counteract the disturbance; otherwise the pitch error will grow and lead to oscillations in the thrust ratio.

As shown in Figure 5.29, the AUV pitched at -2 deg and cruised at 1.4 m/s just before the seeking algorithm was turned on. As the speed was decreased from 50 s to 73 s, the pitch angle decreased and settled down to -10 deg. Throughout the process, the pitch response followed the desired pitch closely. The depth plot shows how the AUV breached the surface and settled down to 1.5 m depth at 50 s. The depth response displayed a steady state error because the integral control had not yet been implemented. In other words, the depth controller was a pure proportional controller where steady state error was expected. Nevertheless, this did not affect the minimum speed

5.5 Experiment Results

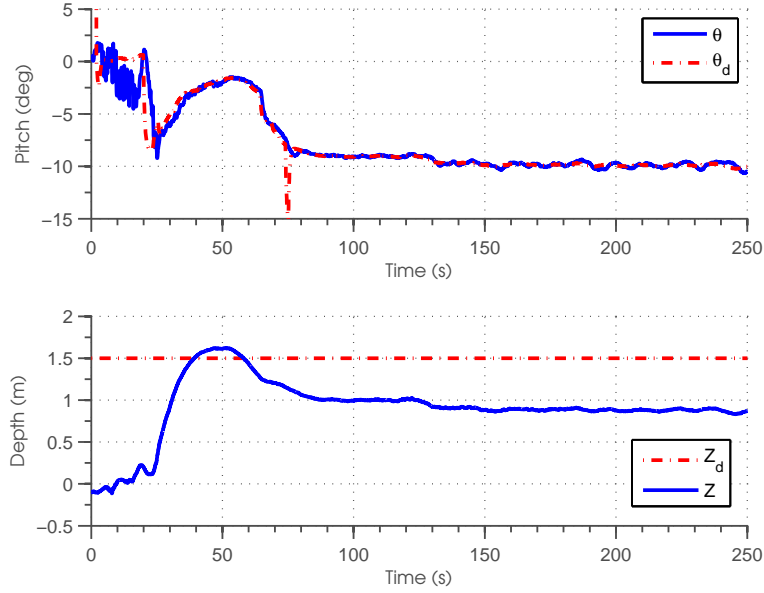


Figure 5.29: Lake experiment: pitch and depth responses.

seeking algorithm as depth measurement was not used in the algorithm.

The results that we discussed above are based on experiment 1 which $\delta_{\max} = 0.26$. We repeated the experiments twice for $\delta_{\max} = 0.35$ and twice for $\delta_{\max} = 0.40$. They are labeled as experiment 2 & 3, and as experiment 4 & 5 respectively as indicated in Table 5.2. Table 5.2 summarizes the important vehicle's states such as depth, pitch angle, thrust ratio, surge speed, heave speed and elevator deflection by taking the average of the last one hundred seconds of data (from 150 s to 250 s). Their respective standard of deviation are indicated in the bracket shown underneath their average value.

Let first look at the experiment 2 and 3. They are repeated experiment for $\delta_{\max} = 0.35$. During the steady state, the AUV was pitch at around -12 deg, traveling at $T_R = 0.44$ with the resultant surge speed around 0.67 m/s for both experiments. This indicates consistency in term of the behavior of the minimum speed seeking algorithm despite working in an unstructured environment that is full of unknown disturbance. Similarly, the results of experiments 4 and 5 for $\delta_{\max} = 0.40$ are also consistent. During the steady state, the AUV was pitch at around -13 deg, traveling at $T_R = 0.43$ with the resultant surge speed around 0.62 m/s for both experiments. We also overlay

5.5 Experiment Results

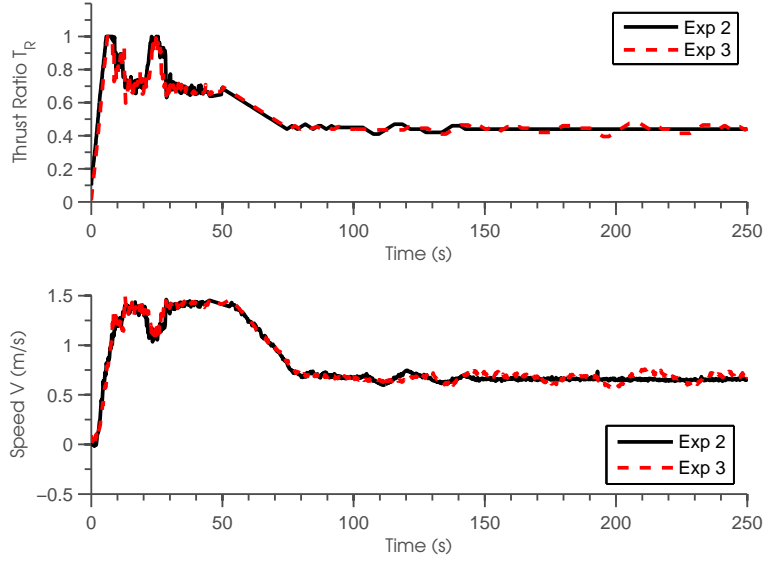


Figure 5.30: Thrust and speed response for two repeated experiments with $\delta_{\max} = 0.35$.

the trajectory of thrust ratio and vehicle speed for experiment 2 & 3, and experiment 4 & 5 in Figure 5.30 and 5.31 respectively. The results match each and other very closely for the repeated experiments.

The results in Table 5.2 also show the effect of fin's effectiveness on the minimum speed. Analysis in Section 3.1 claims that the minimum speed is *inversely* proportional to fin's effectiveness, and the reduction of the minimum speed is coupled with the decrease of the pitch angle (see also Figure 5.11). In this case, increase of δ_{\max} from 0.26 to 0.40 has a similar effect of increasing fin's effectiveness, as the δ_{\max} produces lift force only by multiplication with fin's effectiveness $x_f A_f C_{L\delta}$. The results indicates that the minimum speed reduces and the pitch becomes more negative when the δ_{\max} increases. This matches the theoretical analysis made in Section 3.1.

When the δ_{\max} is set to a larger value, the average thrust ratio and hence the average speed is reduced. At the lower speed, the vehicle needs more downward pitching in order to maintain depth, as indicated by the decrease of pitch angle. However, for $\delta_{\max} = 0.40$, the thrust ratio and the speed of the vehicle is in fact oscillatory as shown in Figure 5.31. This phenomenon is discussed further in detail in Section 5.6.1.

5.5 Experiment Results

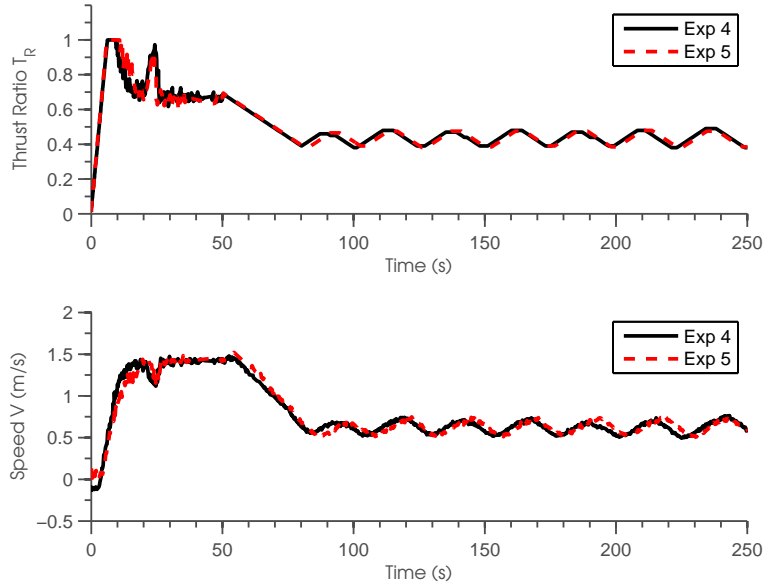


Figure 5.31: Thrust and speed response for two repeated experiments with $\delta_{\max} = 0.40$.

Table 5.2: Summary of experiment results during steady state for different δ_{\max}

Experiment No.	δ_{\max} (rad)	Depth (m)	Pitch (deg)	T_R	u (m/s)	w (m/s)	δ (rad)
1	0.26	0.89 (0.013)	-9.86 (0.220)	0.47 (0.000)	0.76 (0.009)	-0.14 (0.005)	0.25 (0.019)
2	0.35	1.10 (0.035)	-12.86 (0.458)	0.44 (0.007)	0.66 (0.015)	-0.16 (0.005)	0.33 (0.029)
3	0.35	1.22 (0.095)	-11.97 (1.013)	0.44 (0.018)	0.67 (0.042)	-0.15 (0.012)	0.31 (0.063)
4	0.40	0.91 (0.157)	-13.70 (2.169)	0.43 (0.031)	0.61 (0.061)	-0.16 (0.016)	0.36 (0.062)
5	0.40	0.80 (0.170)	-13.63 (2.251)	0.43 (0.032)	0.63 (0.066)	-0.16 (0.016)	0.35 (0.073)

5.5 Experiment Results

5.5.2 Open Sea Experiments

The sea experiments were conducted at Selat Pauh⁶ with the *STARFISH* AUV equipped with a DVL payload (see Figure 5.32).



Figure 5.32: *STARFISH* AUV was towing a float during the open sea experiment. The picture was taken when the AUV was breaching the surface after completing a dive at 1.5 m depth.

Before the start of the mission (0 s - 25 s), the AUV was at rest on the surface and facing the opposite current. The current has a magnitude of 0.5 m/s, indicated by the initial speed in Figure 5.33. Then, the AUV was commanded to cruise at 1.2 m/s until the seeking algorithm was turned on at 75 s. The algorithm started seeking from $T_R = 0.70$, which explained why there was a sudden drop of thrust ratio at 75 s. After that, the thrust ratio was reduced gradually to 0.43. At the same time, the ground speed was reduced to zero. Based on equation (5.54) and (5.55), at $T_R = 0.43$, the AUV should cruise at 0.67 m/s, which was canceled by the opposing current.

Figure 5.34 illustrates how the elevator and the pitch error evolved with time and the corresponding FIS output. The data was logged in the seeking algorithm and was only available from 50 s till 275 s. For sea experiments, the disturbance was expected to be large as the AUV was subjected to underwater currents, surface waves, and external forces and moments introduced by the towing buoy (see Figure 5.32). As a result, the pitch error fluctuated beyond

⁶Selat Pauh is a strait between Hantu Island and Sudong Island, located south-west of mainland Singapore. The area is characterized by strong currents which could run up to 4 knots.

5.5 Experiment Results

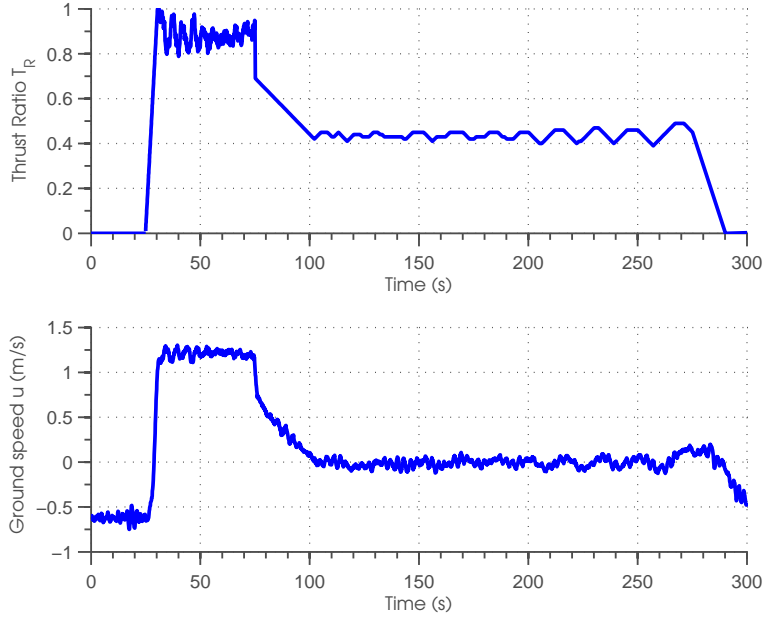


Figure 5.33: Sea experiments: thrust ratio and speed.

the expected bound of 0.01 rad. This triggered fuzzy *rule 3* and led to the oscillation of the thrust ratio. An examination of the pitch error in an early run at sea revealed that θ_e^{TS} should be set to 0.02 rad instead of 0.01 rad. However, since the main aim of this experiment is to test the robustness of the algorithm, the design parameters determined from the lake experiments were maintained here despite changes in vehicle configuration, buoyancy, and operating condition. The pitch error threshold θ_e^{TS} could easily be calibrated in the future by examining the expected pitch error when the AUV is cruising at nominal speed at the sea.

As the ground speed is decreased from 1.2 m/s to almost zero, the pitch angle decreased and settled down at around -10 deg (see Figure 5.35). Similar to the lake experiment, the pitch response followed the desired pitch closely. The depth plot shows how the AUV breached the surface and overshot to 2 m before reaching the desired depth of 1.5 m. In contrast to the lake experiments, integral control was implemented during the sea experiments, causing the depth to be changed slowly to remove the steady state error. Small oscillations in both the pitch and depth responses were observed and

5.5 Experiment Results

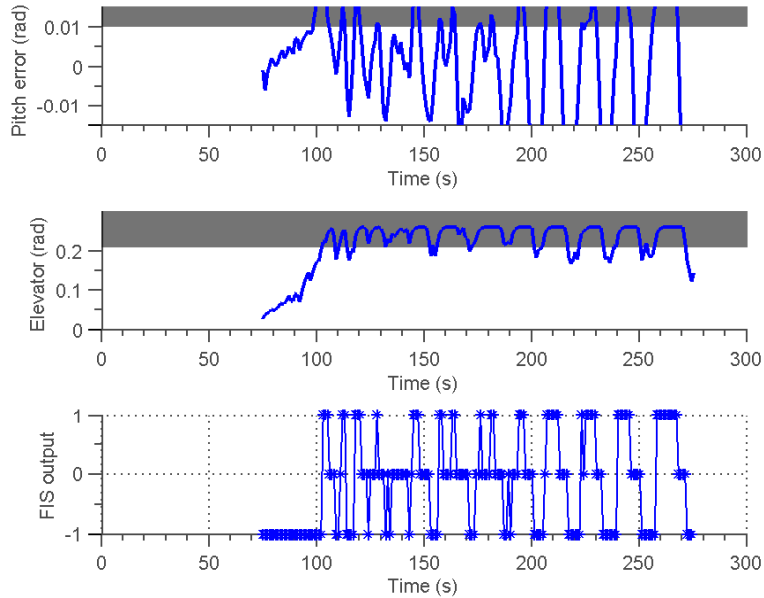


Figure 5.34: Sea experiments: elevator and pitch error.

these were due to the oscillation of thrust ratio explained earlier. The mission ended at 275 s and the AUV was commanded to the surface.

Figure 5.36 plots the x and y positions of the AUV with timing indication. From 0 s to 25 s, the AUV traveled to the east, carried by the current. From 25 s to 75 s, the AUV traveled to the west for about 50 m. After that, the speed of the AUV was reduced gradually to almost zero at 100 s. From 125 s to 275 s, the AUV moved just 10 m to the north for the duration of 150 s, with a speed averaging at 0.07 m/s. The AUV maintained a west heading throughout the whole experiment; the northward motion is due to the underwater current causing a small sway velocity. The results show the possibility that non-hovering AUVs like the *STARFISH* AUV can indeed hover underwater when facing the opposite current.

In order to study the repeatability of the proposed solution, second experiment was conducted immediately after the first experiment using the same set of design parameters. We overlay the trajectory of thrust ratio and vehicle speed for the both experiments in Figure 5.37. Once again, the results match each and other very closely for the repeated experiments.

5.5 Experiment Results

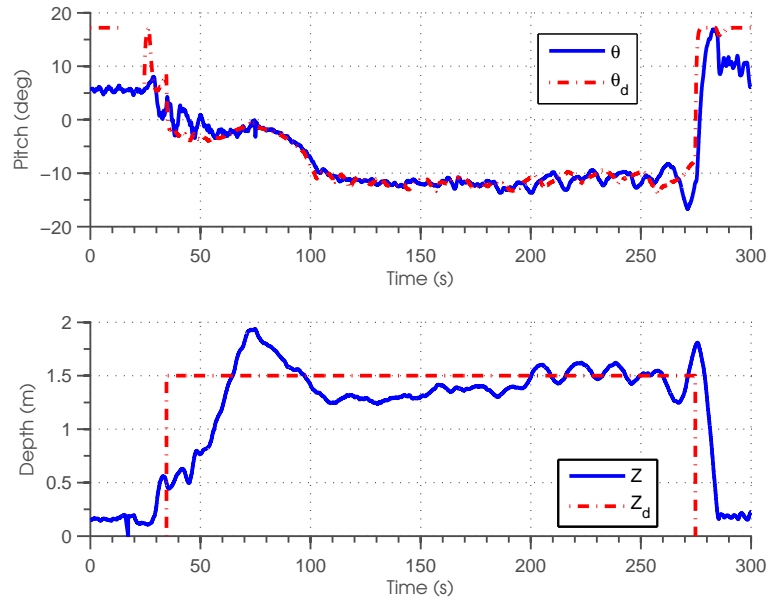


Figure 5.35: Sea experiments: pitch and depth responses.

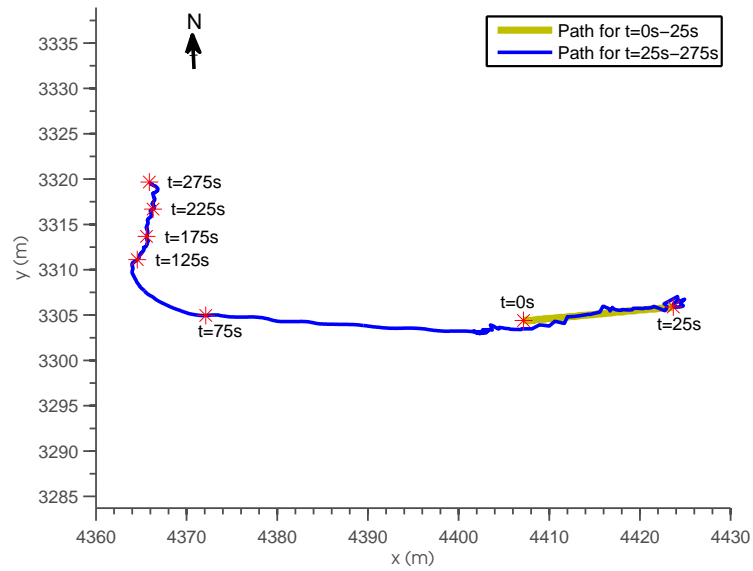


Figure 5.36: Trajectory of the AUV. The AUV was facing west throughout the experiment.

5.5 Experiment Results

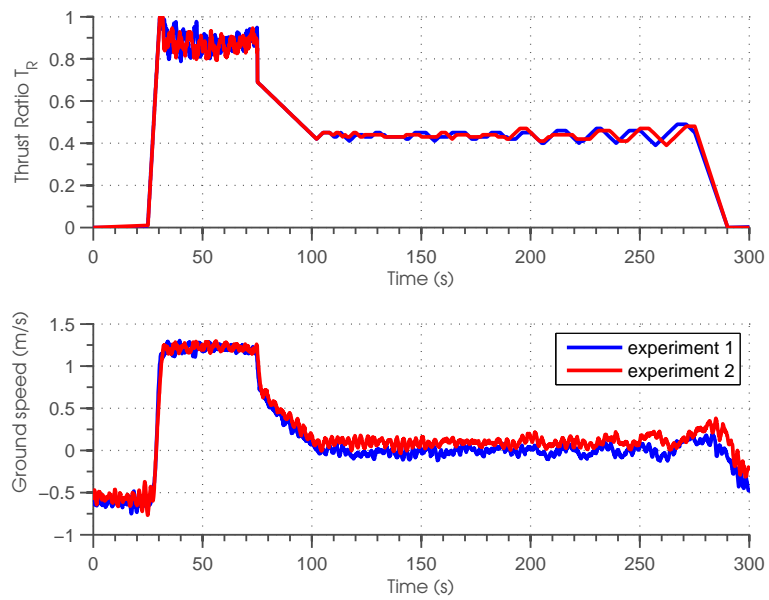


Figure 5.37: Thrust and speed response for two repeated open sea experiments.

5.6 Discussion

5.6.1 Effect of δ_{\max}

The seeking algorithm requires one to know the value of δ_{\max} . The value of δ_{\max} should have been decided earlier when designing the depth and pitch controller. It is understood that when deciding the value of δ_{\max} , controller designers tend to be more conservative to ensure that the fins work within the linear region and away from stall. Here, we investigate the consequence of changing δ_{\max} on the optimality of the solution.

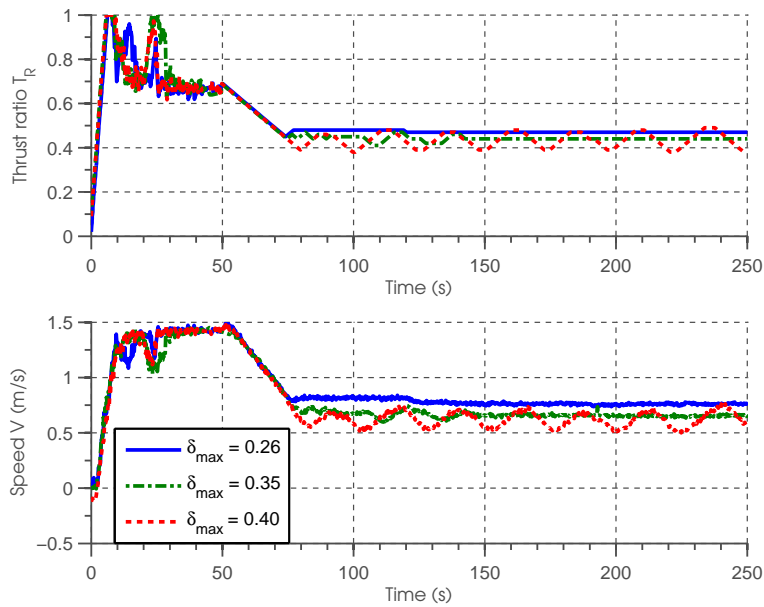


Figure 5.38: Thrust ratio and speed for different δ_{\max} .

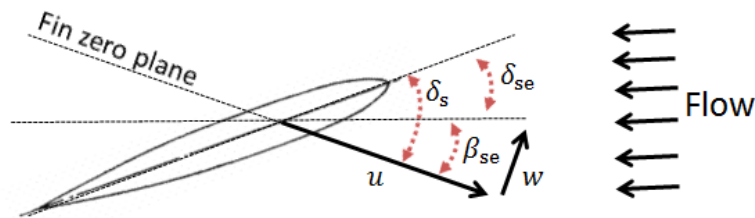


Figure 5.39: Effective fin angles δ_{se} .

We repeated the lake experiments presented in Section 5.5.1 for three

5.6 Discussion

different δ_{\max} and the results are presented in Figure 5.38. At $\delta_{\max} = 0.26$, T_R settled down to 0.47 and the corresponding speed was 0.75 m/s. At $\delta_{\max} = 0.35$, T_R settled down to 0.44 and the corresponding speed was 0.66 m/s. T_R could not settle down and was in a limit cycle when $\delta_{\max} = 0.40$. The results show that the gain in thrust deduction is only marginal even though the change in δ_{\max} is large (from 0.26 to 0.35). When δ_{\max} is set too large, the seeking algorithm will reduce T_R beyond T_R^* . Then, θ_e becomes larger than the θ_e^{TS} , causing the seeking algorithm to increase T_R . When T_R becomes larger than T_R^* , θ_e returns to the normal region. The process repeats itself, forming the limit cycle.

It is of interest to know why the elevator stalls at a much higher value of δ_{\max} . As shown in Figure 5.39, there is a difference between the elevator incidence angle relative to the incoming flow, δ_{se} and the elevator angle relative to the vehicle hull, δ_s . During a constant depth maneuver, the AUV pitches down at a certain angle β_{se} to maintain depth. This causes the stall to occur at a larger δ_{\max} , extended by β_{se} .

5.6.2 Choice of input parameter: thrust or speed

In the initial design, a speed control system which allowed the desired speed to be specified was included in the depth subsystem. The inclusion was found to be a poor choice. Firstly, it is desirable to have the algorithm independent of the Doppler Velocity Log (DVL), since the DVL is an expensive sensor and not all AUVs are equipped with it. Secondly and more importantly, the speed measured by the DVL is with respect to the ground. Minimizing the AUV speed in terms of ground speed should be avoided because the ground speed is affected by underwater currents. On the other hand, the minimum speed of the AUV should be defined in terms of the relative speed to the surrounding water, which determines the hydrodynamic forces acting on the vehicle body and fins. The AUV's relative speed to the surrounding water is purely a function of AUV thrust ratio. Hence, instead of minimizing speed, we solve the equivalent problem of minimizing thrust ratio which is invariant under the influence of the current.

5.7 Summary

Since it is useful for AUVs to move as slowly as possible in some scenarios, we develop an online minimum speed seeking algorithm. While previous research works focused on extending the minimum speed by adding actuators, we propose algorithmic enhancements without the need for any hardware changes. This algorithm is applicable to non-hovering AUVs, which are widely in service nowadays.

We constructed a depth dynamic model for a typical torpedo-shaped AUV. Through the model, we explained the mechanism of the minimum speed and identified three major factors (buoyancy, righting moment and the fin's effectiveness) that affect the value of the minimum speed. A minimum speed seeking algorithm was then developed under the framework of extremum seeking. We extend the framework by introducing a new definition of steady state mapping which imposes new structure on the seeking algorithm.

We verified the seeking algorithm in the lake experiments using the STARFISH AUV. The STARFISH AUV is normally operated at 0.70 thrust ratio with a nominal speed of 1.4 m/s. The seeking algorithm managed to reduce the thrust ratio to 0.47 with the corresponding speed of 0.75 m/s, while maintaining the depth of the AUV. We repeated the experiment in a sea environment with the same set of design parameters to demonstrate the robustness of the algorithm. The thrust ratio converged to 0.43 despite a small oscillation. The results from the sea experiments show the possibility that the non-hovering AUV can indeed hover underwater when facing opposite currents.

Chapter 6

Conclusions and Future Research

6.1 Conclusions

AUVs have a wide range of applications in ocean research and are increasingly being used for different scientific, military, and commercial purposes. In order to achieve different tasks, AUVs are designed to be modular, where their payload configuration can be changed frequently depending on the mission requirements. However, the changing of the payload configuration will affect the dynamic characteristic of an AUV. Since the dynamic model underlies the design of its navigation, guidance and control systems, any deviation from the nominal model would potentially degrade the vehicle's performance.

Therefore, we have developed a method to enable rapid identification of AUV dynamics via field experiments. The method can be employed to obtain an updated dynamic model economically whenever there is a change in payload configuration or vehicle geometry. The newly configured AUV is commanded to perform a compact set of maneuvers where doublet excitation is used to excite the dynamics. The identification process has two main stages. In the training stage, the control fins and attitude measurements are processed online by the SVF-RLS estimator to produce an estimation of the unknown model parameters. In the validation stage, the prediction capability

6.1 Conclusions

of the identified model is checked using fresh validation data sets.

For experiments on five different thrust settings, the parameters showed fast convergence within 12 s. Validation results showed that the identified models can explain 78% to 92% of the output variation, and hence we are convinced that the identified models have captured the dominant characteristics of the dynamics. The identification results indicated that the rotational drag coefficient a_{22} has a small variation around its mean when the speed varies. The rudder control authority b_2 varies linearly with the square of speed u^2 which matches well with our physical understanding. These observations are important because they allow us to predict the dynamic model beyond those identified, via interpolation or extrapolation.

We have compared the SVF-RLS estimator against a conventional offline identification method that requires numerical optimization. The comparison showed that the SVF-RLS estimator outperforms the offline method in terms of prediction accuracy, computational cost, and shorter training time by detecting parameter convergence online. The usefulness of the identified parameters was highlighted in two applications. First, we illustrated how the yaw identification results can be used to estimate the turning radius of the AUV at different speeds. The accuracy of the estimation was validated in a field experiment. Second, the understanding of yaw dynamics at different speeds allows easy implementation of a gain-scheduled controller. The experimental results indicated that the gain-scheduled controller achieved better system performance compared with a constant gain controller.

In order to meet the decoupling assumption, the roll angle of the AUV has to be kept small. Hence, we have demonstrated the use of an internal rolling mass mechanism for active roll stabilization in a typical AUV. We are the first to report on the use of such mechanism for roll stabilization. The mechanism was designed and implemented in the STARFISH AUV. A nonlinear model was first developed to describe the dynamics of the AUV's roll. The model was later linearized to obtain a transfer function for controller synthesis. The model parameters were identified through open-loop testing in a water tank. A Proportional-Integral controller was then designed to increase the overall system damping and remove the steady-state error. The capability of IRM to

6.1 Conclusions

stabilize the roll motion was demonstrated in tank tests and field experiments.

As the parameters of the dynamic model are scheduled according to the vehicle's speed, the operating range of the speed need to be known, in particular, the minimum achievable speed. We have explained the mechanism behind the phenomenon and also developed a novel algorithm such that the AUV is automatically controlled to travel at its minimum speed while maintaining a constant depth. It is the first time that such an algorithm is developed.

First, we have analyzed a depth dynamic model for a typical torpedo-shaped AUV. Through the model, we gave a formal definition of the minimum speed. Next, we derived the equations for two important curves: maximum required pitch curve and achievable pitch curve. We then argued that the minimum speed occurs at the intersection of these two curves. The final solution of the minimum speed was then derived together with its condition of existence. By analyzing the maximum required pitch curve and the achievable pitch curve, we studied how the buoyancy, righting moment, and the fin's effectiveness affect the minimum speed. This understanding provides us with an insight into how the minimum speed of an AUV could be altered in practice.

However, the model is not useful in predicting the exact value of the minimum speed as the model parameters (hydrodynamic coefficients) are not known with high accuracy. In addition, the minimum speed is also affected by the environmental disturbance. Therefore, any prior determination of the minimum speed would be either highly conservative or else, it runs the risk of the AUV losing its controllability. We have developed a minimum speed seeking algorithm under the framework of extremum seeking. Online measurements of the elevator and the pitch error is fed to a fuzzy inference system, which in turn decides whether to increase, decrease or keep the thrust ratio at every seeking interval. The design of the seeking algorithm does not require accurate modeling of the dynamics of the AUV. Instead, the design parameters can be determined based on some known characteristic of the AUV and some available measurements.

The effectiveness of the algorithm in seeking the minimum speed was first

6.2 Future Research

studied by simulation. Through simulation, we also investigated the effect of the design parameters on the stability and the optimality of the solution. Next, we verified the seeking algorithm in the lake experiments using the *STARFISH* AUV. The *STARFISH* AUV is normally operated at 0.70 thrust ratio with a nominal speed of 1.4 m/s. The seeking algorithm managed to reduce the thrust ratio to 0.47 with the corresponding speed of 0.75 m/s while maintaining the depth of the AUV. The seeking algorithm worked consistently in a number of repeated experiments. We also repeated the experiment in a sea environment with the same set of design parameters to demonstrate the robustness of the algorithm. The thrust ratio converged to 0.43 despite a small oscillation was observed. The results from the sea experiments showed the possibility that the non-hovering AUV can indeed hover underwater when facing opposite currents.

The availability of such an algorithm as a built-in function of an AUV, will open up new possibilities in a number of operation scenarios such as underwater loitering with minimal energy consumption, underwater docking with minimal impact, target scanning with minimum speed, and hovering with the help of underwater current.

6.2 Future Research

1. The online system identification might be expanded in the future to detect potential faults that could occur, such as fin stuck due to the malfunction of a servomotor, and fin offset due to a collision. In order to capture the fault, fault detection system needs to be turned on during normal operation of the AUV. However, data collected during the normal operation (for example, when running on a straight path) have very low signal to noise ratio and could result in erroneous parameter estimation. Hence, an intelligent filter needs to be designed so that the dynamic model is updated only if the data contain useful information.
2. Through the sea experiments, we have shown the potential of an AUV performing hovering with the help of underwater current. However, in

6.2 Future Research

order to hover, the direction and magnitude of the underwater current need to be estimated. If the underwater current has a magnitude larger than or equal to the minimum speed of the AUV, then the AUV can be commanded at the particular thrust to cancel the opposite current.

3. We have demonstrated the effectiveness of the internal rolling mass in regulating the roll of the AUV. However, since the controller was designed based on the decoupling technique, it does not tackle directly the moment generated when the AUV is turning. The coupling effect between yaw and roll during the turn could be studied in the future, and a controller could be designed to suppress the coupling effect.

Appendix A

Publications arising from this thesis

- Y. H. Eng and M. Chitre, “Roll control of an autonomous underwater vehicle using an internal rolling mass”, in Field and Service Robotics Conference, QUT, Australia, 2013.
- Y. H. Eng, K. M. Teo, and M. Chitre, “Online system identification of the dynamics of an Autonomous Underwater vehicle”, in IEEE International Underwater Technology Symposium (UT), The University of Tokyo, Tokyo, Japan, Mar 2013.
- Y. H. Eng, K. M. Teo, M. Chitre, and K. M. Ng, “Online system identification of an autonomous underwater vehicle via in-field experiments”, in IEEE Journal of Ocean Engineering.
- Y. H. Eng, M. Chitre, K. M. Teo, and K. M. Ng, “Minimum speed seeking control for non-hovering autonomous underwater vehicles”, in Journal of Field Robotics. (under review)

Appendix B

Online Identification Result for Pitch Dynamics

In this appendix, we present the identification result for pitch dynamics of the AUV. First, we start with the development of pitch dynamics model. Once the dynamics is described in a linear parameter model, one then apply method developed in chapter 3 to identify the four unknown parameters for different thrust settings.

B.1 Pitch Dynamics

By making the following assumptions, we restrict the motion of the AUV in the diving plane (x - z plane):

1. sway velocity $v = 0$.
2. roll $\phi = 0$.
3. constant heading $\psi = \psi_o \Rightarrow$ yaw rate $\dot{\psi} = 0$.

The equations of motion for heave and pitch are:

$$m(\dot{w} - u_0q) = Z \tag{B.1}$$

$$I_y\dot{q} = M \tag{B.2}$$

B.1 Pitch Dynamics

The heave external force Z and pitch moments M consist of hydrodynamic added mass, linear damping, cross flow drag, Munk moment and effect of elevator plane deflection. In addition, there is righting moment in pitch due to the vertical distance between the center of mass and the center of buoyancy $BG_z = z_G - z_B$. There is also excessive positive buoyancy of the vehicle $\Delta B = B - mg$ that acts in z -axis.

$$Z = Z_{\dot{w}}\dot{w} + Z_{\dot{q}}\dot{q} + Z_w w + Z_q q + Z_{\delta}\delta_s + \Delta B \quad (\text{B.3})$$

$$\begin{aligned} M &= M_{\dot{w}}\dot{w} + M_{\dot{q}}\dot{q} + M_w w + M_q q \\ &\quad - mg(z_G - z_B) \sin \theta + M_{\delta}\delta_s \\ &\simeq M_{\dot{w}}\dot{w} + M_{\dot{q}}\dot{q} + M_w w + M_q q \\ &\quad - mgBG_z \theta + M_{\delta}\delta_s \end{aligned} \quad (\text{B.4})$$

From kinematics analysis in x-z plane with assumption of small pitch angle, we have:

$$\dot{\theta} = q \quad (\text{B.5})$$

$$\dot{z} = -\theta u_0 + w \quad (\text{B.6})$$

Substituting (B.3) and (B.4) into (B.1) and (B.2) respectively and combining with (B.5) and (B.6), we can write the following state space representation using state variable $w(t)$, $q(t)$, $\theta(t)$, and $z(t)$:

$$\begin{aligned} \begin{bmatrix} \dot{w} \\ \dot{q} \\ \dot{\theta} \\ \dot{z} \end{bmatrix} &= \begin{bmatrix} -c_{11} & -c_{12} & -c_{13} & 0 \\ -c_{21} & -c_{22} & -c_{23} & 0 \\ 0 & 1 & 0 & 0 \\ 1 & 0 & -u_0 & 0 \end{bmatrix} \begin{bmatrix} w \\ q \\ \theta \\ z \end{bmatrix} \\ &+ \begin{bmatrix} d_1 \\ d_2 \\ 0 \\ 0 \end{bmatrix} \delta_s + \begin{bmatrix} e_1 \\ e_2 \\ 0 \\ 0 \end{bmatrix} \Delta B \end{aligned} \quad (\text{B.7})$$

B.1 Pitch Dynamics

By assuming the value of $c_{21}w$ to be constant as heave velocity does not fluctuate significantly during a run, the linear model in (B.7) reduces to:

$$\begin{aligned} \begin{bmatrix} \dot{q} \\ \dot{\theta} \\ \dot{z} \end{bmatrix} &= \begin{bmatrix} -c_{22} & -c_{23} & 0 \\ 1 & 0 & 0 \\ 0 & -u_0 & 0 \end{bmatrix} \begin{bmatrix} q \\ \theta \\ z \end{bmatrix} \\ &+ \begin{bmatrix} d_2 \\ 0 \\ 0 \end{bmatrix} \delta_s + \begin{bmatrix} c_{21}w + e_2\Delta B \\ 0 \\ 0 \end{bmatrix} \end{aligned} \quad (\text{B.8})$$

Thus, the pitch dynamics are:

$$\dot{\theta} = q \quad (\text{B.9})$$

$$\dot{q} = -c_{22}q - c_{23}\theta + d_2\delta_s + C_b \quad (\text{B.10})$$

where

$$C_b = c_{21}w + e_2\Delta B \quad (\text{B.11})$$

The above derivation of the depth subsystem model follows the derivation in [13] closely but takes into the consideration that the AUV is positive buoyant. From experimental measurements, the resulting heave velocity is around 0.13 m/s and therefore it is not negligible. In [13], the heave velocity is small (less than 0.05 m/s). The heave velocity introduces cross flow drag and Munk moment which result in an offset term C_b that needs to be compensated by the pitch controller.

Rewriting (B.10), we have four parameters to be identified:

$$\dot{q} = \begin{bmatrix} -q & -\theta & \delta & 1 \end{bmatrix} \begin{bmatrix} c_{22} \\ c_{23} \\ d_2 \\ C_b \end{bmatrix} \quad (\text{B.12})$$

B.2 Identification Results and Discussion

Equation (B.10) can also be rewritten in the following form by introducing a new term, steady state elevator deflection δ_{s0} :

$$\begin{aligned}\dot{q} &= -c_{22}q - c_{23}\theta + d_2\left(\delta_s + \frac{C_b}{d_2}\right) \\ \dot{q} + c_{22}q + c_{23}\theta &= d_2(\delta_s + \delta_{s0})\end{aligned}\tag{B.13}$$

Applying Laplace Transform and a change of variable, we have:

$$\frac{\theta(S)}{\delta'_s(S)} = \frac{d_2}{s^2 + c_{22}s + c_{23}}, \delta'_s(S) = \mathcal{L}(\delta_s + \delta_{s0})\tag{B.14}$$

B.2 Identification Results and Discussion

B.2.1 Experimental Procedure

The AUV was commanded to perform a straight run of 100 m at a depth of 2 m. When the AUV reached steady state (maintaining constant heading and depth), the excitation signal of ± 0.26 rad for 2 seconds respectively was injected into elevator deflection (Fig. B.2d). The deflection generates moment in pitch axis and excites the pitch dynamics dramatically (Fig. B.2b). After the excitation, the depth controller was switched on to return the AUV to the desired depth. The whole process was repeated for the second time for the richness of the data set. During the data collection, it is important to monitor the AUV's roll and yaw angle. Roll should be maintained near zero (Fig. B.2a) and yaw angle should be maintained constant (Fig. B.2c) in order to minimize the coupling effect. This is also illustrated in Fig. B.1b where the AUV was moving in a straight path in the x-y position plot.

B.2.2 Identification Result

The results of identification are summarized in Table B.1 and Fig. B.3 shows how the parameters evolve with time. The linear damping term c_{22} and righting moment term c_{23} have values range between 2.1 to 2.6 and 0.02 to

B.2 Identification Results and Discussion

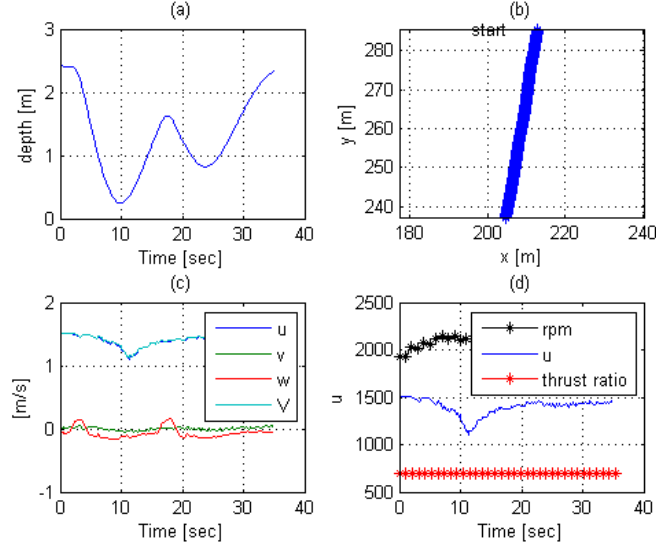


Figure B.1: Experiment run for identification for pitch dynamics at thrust ratio 70%. Plot of depth, x-y position, velocity and thrust ratio

0.05 respectively with varying speeds. The positive value of both c_{22} and c_{23} indicate that the pitch dynamics is inherently stable (poles are in the left-half plane) over the entire speed range. The elevator control authority d_2 increases with speed due to higher dynamic pressure at the control surfaces. Theoretically, the gain d_2 should vary linearly with the square in speed, u^2 . This is verified in Fig. B.4 which plot d_2 against u^2 . The negative value of d_2 indicates that the positive rudder input creates negative moment in pitch. The magnitude of steady state elevator fin deflection δ_{s_0} reduces with increase of speed. In order to maintain a constant depth, AUV needs to pitch down slightly to overcome its own buoyancy. The net buoyancy stays constant. However, when AUV's thrust increases, the required pitch down angle θ_0 is reduced and thus the steady state elevator deflection.

From the last column of Table B.1, it is observed that R^2 ranges from 0.83 to 0.93, which indicates that the models can explain 83% to 93% of the pitch output variation. The variation of R^2 values is expected as the experiments were conducted in unstructured real world environment, subjected to unknown disturbance and measurement noise. Nevertheless, the overall

B.2 Identification Results and Discussion

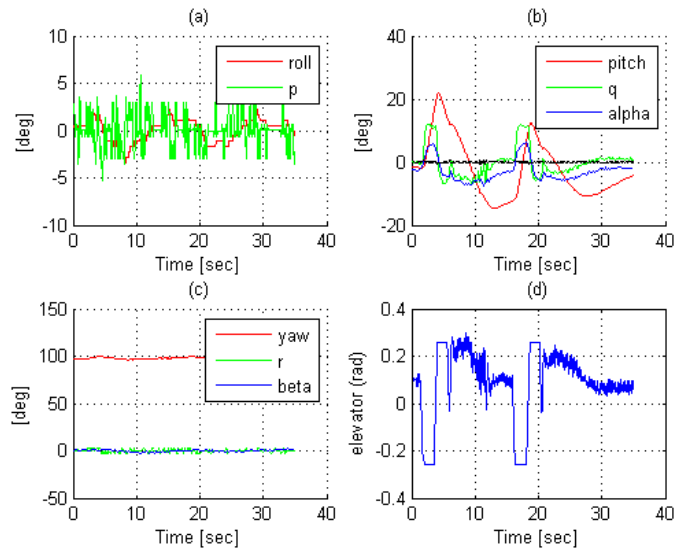


Figure B.2: Experiment run for identification for pitch dynamics at thrust ratio 70%. Plot of roll, pitch, yaw and elevator

prediction capabilities are satisfactory as one could see in Fig. B.5, which overlays both θ_{real} and θ_{sim} for thrust 60% to 100% and their corresponding R^2 values. The simulated response ψ_{sim} is able to describe the measured response very well for all thrust settings. From the results, we are convinced that the identified models have captured the dominant dynamic characteristic of the process.

Table B.1: Parameters identified for Pitch dynamics at different thrust

Thrust (%)	Speed (m/s)	c_{22}	c_{23}	d_2	C_b	δ_{s_0} (rad)	θ_0 (deg)	R^2
60	1.09	2.13	0.052	-0.94	0.089	-0.095	-2.72	0.87
70	1.37	2.34	0.057	-1.34	0.100	-0.075	-1.53	0.90
80	1.67	2.31	0.031	-1.58	0.081	-0.051	-0.94	0.83
90	1.93	2.43	0.021	-1.91	0.102	-0.054	-0.40	0.93
100	2.23	2.57	0.033	-2.39	0.099	-0.042	-0.06	0.90

B.2 Identification Results and Discussion

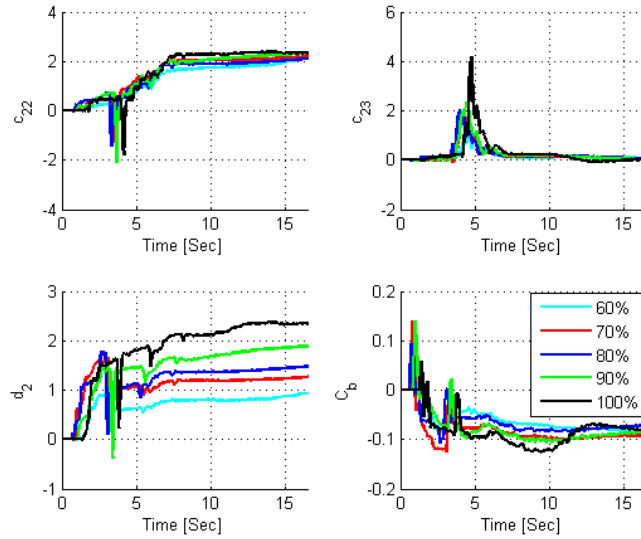


Figure B.3: Online parameters estimation of pitch dynamics for different thrusts

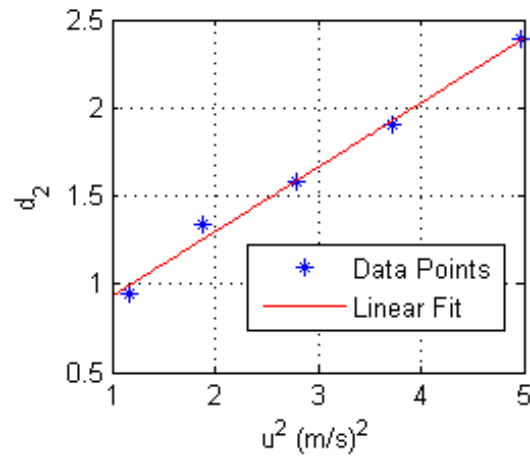


Figure B.4: Plot of elevator control authority d_2 against speed²

B.2 Identification Results and Discussion

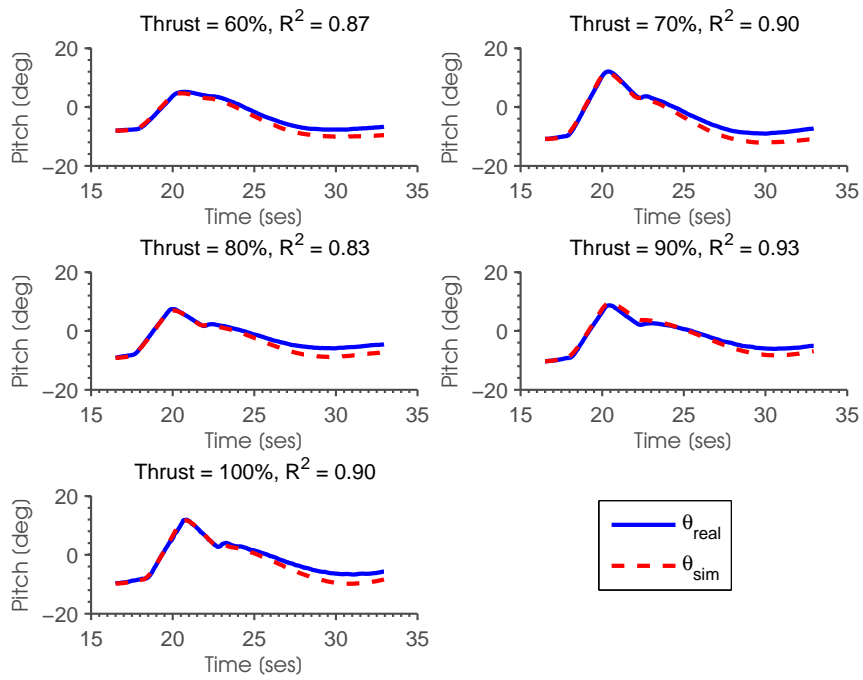


Figure B.5: Validation plots for experiments on five different thrust settings.

References

- [1] S. M. Glenn, J. F. Grassle, and C. von Alt, “A well sampled ocean: the LEO approach,” *Oceanus*, vol. 42, pp. 28–30, 2000.
- [2] J. Yuh, “Design and control of autonomous underwater robots: A survey,” *Autonomous Robots*, vol. 8, no. 1, pp. 7–24, 2000.
- [3] L. Shirtley, P. Formby, M. Bell, and S. Anstee, “Modification of a nose cone for a remus 100 autonomous underwater vehicle to improve low-speed stability.” 2009.
- [4] K. Zhou and J. C. Doyle, *Essentials of robust control*. Prentice hall Upper Saddle River, NJ, 1998, vol. 104.
- [5] K. J. Åström and B. Wittenmark, *Adaptive control*. Courier Dover Publications, 2013.
- [6] A. Zilouchian and M. Jamshidi, *Intelligent control systems using soft computing methodologies*. CRC Press, Inc., 2000.
- [7] M. Caccia, G. Indiveri, and G. Veruggio, “Modeling and identification of open-frame variable configuration unmanned underwater vehicles,” *IEEE Journal of Oceanic Engineering*, vol. 25, no. 2, pp. 227–240, 2000.
- [8] N. Mišković, Z. Vukić, M. Bibuli, G. Bruzzone, and M. Caccia, “Fast in-field identification of unmanned marine vehicles,” *Journal of Field Robotics*, vol. 28, no. 1, pp. 101–120, 2011.
- [9] A. Healey, “Towards an automatic health monitor for autonomous underwater vehicles using parameter identification,” in *American Control Conference, 1993*. IEEE, 1993, pp. 585–589.
- [10] M. Rentschler, F. Hover, and C. Chryssostomidis, “System identification of open-loop maneuvers leads to improved AUV flight performance,” *IEEE Journal of Oceanic Engineering*, vol. 31, no. 1, pp. 200–208, 2006.

REFERENCES

- [11] L. Ljung and T. Glad, "On global identifiability for arbitrary model parametrizations," *Automatica*, vol. 30, no. 2, pp. 265–276, 1994.
- [12] T. Fossen, *Marine control systems: Guidance, navigation and control of ships, rigs and underwater vehicles*. Marine Cybernetics Trondheim,, Norway, 2002.
- [13] B. Jalving, "The NDRE-AUV flight control system," *IEEE Journal of Oceanic Engineering*, vol. 19, no. 4, pp. 497–501, 1994.
- [14] A. Healey and D. Lienard, "Multivariable sliding mode control for autonomous diving and steering of unmanned underwater vehicles," *IEEE Journal of Oceanic Engineering*, vol. 18, no. 3, pp. 327–339, 1993.
- [15] R. McEwen and K. Streitlien, "Modeling and control of a variable-length AUV," *Proc 12th UUST*, 2001.
- [16] P. Ridao, A. Tiano, A. El-Fakdi, M. Carreras, and A. Zirilli, "On the identification of non-linear models of unmanned underwater vehicles," *Control engineering practice*, vol. 12, no. 12, pp. 1483–1499, 2004.
- [17] D. Smallwood and L. Whitcomb, "Adaptive identification of dynamically positioned underwater robotic vehicles," *Control Systems Technology, IEEE Transactions on*, vol. 11, no. 4, pp. 505–515, 2003.
- [18] A. Tiano, R. Sutton, A. Lozowicki, and W. Naeem, "Observer kalman filter identification of an autonomous underwater vehicle," *Control engineering practice*, vol. 15, no. 6, pp. 727–739, 2007.
- [19] J. Petrich, W. Neu, and D. Stilwell, "Identification of a simplified AUV pitch axis model for control design: Theory and experiments," in *OCEANS 2007*. IEEE, 2007, pp. 1–7.
- [20] T. Fossen, "Guidance and control of ocean vehicles," *New York*, 1994.
- [21] T. Presterio, "Verification of a six-degree of freedom simulation model for the remus autonomous underwater vehicle," Master's thesis, Massachusetts Institute of Technology and Woods Hole Oceanographic Institution, 2001.
- [22] C. Silvestre and A. Pascoal, "Control of the infante AUV using gain scheduled static output feedback," *Control Engineering Practice*, vol. 12, no. 12, pp. 1501–1509, 2004.

REFERENCES

- [23] D. Yoerger and J. Slotine, "Robust trajectory control of underwater vehicles," *IEEE Journal of Oceanic Engineering*, vol. 10, no. 4, pp. 462–470, 1985.
- [24] T. Fossen and S. Sagatun, "Adaptive control of nonlinear systems: A case study of underwater robotic systems," *Journal of Robotic Systems*, vol. 8, no. 3, pp. 393–412, 1991.
- [25] J. Da Cunha, R. Costa, and L. Hsu, "Design of a high performance variable structure position control of ROVs," *IEEE Journal of Oceanic Engineering*, vol. 20, no. 1, pp. 42–55, 1995.
- [26] J. Slotine, W. Li *et al.*, *Applied nonlinear control*. Prentice-Hall Englewood Cliffs, NJ, 1991, vol. 199, no. 1.
- [27] D. Yoerger, J. Newman, and J. Slotine, "Supervisory control system for the JASON ROV," *IEEE Journal of Oceanic Engineering*, vol. 11, no. 3, pp. 392–400, 1986.
- [28] D. Yoerger and J. Slotine, "Adaptive sliding control of an experimental underwater vehicle," in *Robotics and Automation, 1991. Proceedings., 1991 IEEE International Conference on*. IEEE, 1991, pp. 2746–2751.
- [29] R. Cristi, F. Papoulias, and A. Healey, "Adaptive sliding mode control of autonomous underwater vehicles in the dive plane," *IEEE Journal of Oceanic Engineering*, vol. 15, no. 3, pp. 152–160, 1990.
- [30] J. Yuh, "Learning control for underwater robotic vehicles," *Control Systems, IEEE*, vol. 14, no. 2, pp. 39–46, 1994.
- [31] J. Yuh and J. Nie, "Application of non-regressor-based adaptive control to underwater robots: experiment," *Computers & Electrical Engineering*, vol. 26, no. 2, pp. 169–179, 2000.
- [32] K. Goheen and E. Jefferys, "Multivariable self-tuning autopilots for autonomous and remotely operated underwater vehicles," *IEEE Journal of Oceanic Engineering*, vol. 15, no. 3, pp. 144–151, 1990.
- [33] K. Ishii, T. Fujii, and T. Ura, "An on-line adaptation method in a neural network based control system for AUVs," *IEEE Journal of Oceanic Engineering*, vol. 20, no. 3, pp. 221–228, 1995.
- [34] S. Smith, G. Rae, D. Anderson, and A. Shein, "Fuzzy logic control of an autonomous underwater vehicle," *Control Engineering Practice*, vol. 2, no. 2, pp. 321–331, 1994.

REFERENCES

- [35] N. Kato, Y. Ito, J. Kojima, S. Takagi, K. Asakawa, and Y. Shirasaki, "Control performance of autonomous underwater vehicle AQUA EXPLORER 1000 for inspection of underwater cables," in *OCEANS'94. 'Oceans Engineering for Today's Technology and Tomorrow's Preservation. Proceedings*, vol. 1. IEEE, 1994, pp. I-135.
- [36] J. Wang and C. Lee, "Self-adaptive recurrent neuro-fuzzy control of an autonomous underwater vehicle," *Robotics and Automation, IEEE Transactions on*, vol. 19, no. 2, pp. 283-295, 2003.
- [37] X. Liang, Y. Gan, and L. Wan, "Motion controller for autonomous underwater vehicle based on parallel neural network." *JDCTA*, vol. 4, no. 9, pp. 61-67, 2010.
- [38] J. Petrich and D. Stilwell, "Robust control for an autonomous underwater vehicle that suppresses pitch and yaw coupling," *Ocean Engineering*, 2010.
- [39] H. Singh, L. Whitcomb, D. Yoerger, and O. Pizarro, "Microbathymetric mapping from underwater vehicles in the deep ocean," *Computer Vision and Image Understanding*, vol. 79, no. 1, pp. 143-161, 2000.
- [40] W. Kirkwood, W. R. Anderson, and C. Kitts, "Fault tolerant actuation for Dorado class AUVs." *Instrumentation viewpoint*, no. 8, pp. 40-41, 2009.
- [41] P. Woock, "Deep-sea seafloor shape reconstruction from side-scan sonar data for AUV navigation," in *OCEANS, 2011 IEEE-Spain*. IEEE, 2011, pp. 1-7.
- [42] C. Woolsey and N. Leonard, "Moving mass control for underwater vehicles," in *American Control Conference, 2002. Proceedings of the 2002*, vol. 4. IEEE, 2002, pp. 2824-2829.
- [43] N. Leonard and J. Graver, "Model-based feedback control of autonomous underwater gliders," *IEEE Journal of Oceanic Engineering*, vol. 26, no. 4, pp. 633-645, 2001.
- [44] A. Alvarez, A. Caffaz, A. Caiti, G. Casalino, L. Gualdesi, A. Turetta, and R. Viviani, "Folaga: a low-cost autonomous underwater vehicle combining glider and AUV capabilities," *Ocean Engineering*, vol. 36, no. 1, pp. 24-38, 2009.
- [45] P. J. LeBas, "Maximizing AUV slow speed performance," Master's thesis, Monterey, California. Naval Postgraduate School, 1997.

REFERENCES

- [46] J. Liu, M. Furlong, A. Palmer, A. Phillips, S. Turnock, and S. Sharkh, *Design and Control of a Flight-Style AUV with Hovering Capability*. Autonomous Undersea Systems Institute (AUSI), 2009.
- [47] B. Helgason, “Low Speed Modeling and Simulation of Gavia AUV,” Master’s thesis, Reykjavik University, 2012.
- [48] C. L. Nickell, C. A. Woolsey, and D. J. Stilwell, “A low-speed control module for a streamlined AUV,” in *OCEANS, 2005. Proceedings of MTS/IEEE*. IEEE, 2005, pp. 1680–1685.
- [49] C. L. Nickell, “Modular modification of a buoyant AUV for low-speed operation,” Master’s thesis, Virginia Polytechnic Institute and State University, 2005.
- [50] K. Mahata and H. Garnier, “Direct identification of continuous-time errors-in-variables models,” in *Preprints of the 16th World Congress of the International Federation of Automatic Control, July, 2005*, pp. 3–8.
- [51] M. Verhaegen and V. Verdult, *Filtering and system identification: a least squares approach*. Cambridge university press, 2007.
- [52] T. Söderström, L. Ljung, and I. Gustavsson, “A theoretical analysis of recursive identification methods,” *Automatica*, vol. 14, no. 3, pp. 231–244, 1978.
- [53] L. Ljung, *System identification*. Wiley Online Library, 1999.
- [54] J. C. Lagarias, J. A. Reeds, M. H. Wright, and P. E. Wright, “Convergence properties of the nelder–mead simplex method in low dimensions,” *SIAM Journal on Optimization*, vol. 9, no. 1, pp. 112–147, 1998.
- [55] H. Garnier, M. Gilson, T. Bastogne, and M. Mensler, “The CONSTID toolbox: A software support for data-based continuous-time modelling,” *Identification of Continuous-time Models from Sampled Data*, pp. 249–290, 2008.
- [56] J. Kim, K. Kim, H. Choi, W. Seong, and K. Lee, “Depth and heading control for autonomous underwater vehicle using estimated hydrodynamic coefficients,” in *MTS/IEEE OCEANS, 2001*, vol. 1. IEEE, 2001, pp. 429–435.
- [57] T.-B. Koay, Y.-T. Tan, Y.-H. Eng, R. Gao, M. Chitre, J.-L. Chew, N. Chandhavarkar, R. Khan, T. Taher, and J. Koh, “Starfish – a small

REFERENCES

- team of autonomous robotic fish,” *Indian Journal of Geo-Marine Science*, vol. 40, no. 2, pp. 157–167, April 2011.
- [58] Y. H. Eng, K. M. Teo, and M. Chitre, “Online system identification of the dynamics of an autonomous underwater vehicle,” in *IEEE International Underwater Technology Symposium (UT) 2013*, 2013, pp. 1–10.
- [59] S. M. LaValle, *Planning algorithms*. Cambridge university press, 2006.
- [60] N. S. Nise, *Control systems engineering*, 3rd ed. John Wiley & Sons, 2000.
- [61] M. A. Abkowitz, *Stability and motion control of ocean vehicles: organization, development, and initial notes of a course of instruction in the subject*. MIT press, 1969.
- [62] J. Petrich and D. Stilwell, “Model simplification for AUV pitch-axis control design,” *Ocean Engineering*, vol. 37, no. 7, pp. 638–651, 2010.
- [63] M. S. Triantafyllou and F. S. Hover, “Maneuvering and control of marine vehicles,” *Department of Ocean Engineering, Massachusetts Institute of Technology, Cambridge, USA*, 2002.
- [64] Y. Tan, W. Moase, C. Manzie, D. Nesic, and I. Mareels, “Extremum seeking from 1922 to 2010,” in *IEEE Control Conference (CCC), 2010 29th Chinese*, 2010, pp. 14–26.
- [65] C. Zhang and R. Ordãoãnez, *Extremum-seeking control and applications: a numerical optimization-based approach*. Springer, 2012.
- [66] A. R. Teel and D. Popovic, “Solving smooth and nonsmooth multivariable extremum seeking problems by the methods of nonlinear programming,” in *Proceedings of the American Control Conference, 2001.*, vol. 3, 2001, pp. 2394–2399.
- [67] M. Krstić and H.-H. Wang, “Stability of extremum seeking feedback for general nonlinear dynamic systems,” *Automatica*, vol. 36, no. 4, pp. 595–601, 2000.
- [68] L. Perumal and F. H. Nagi, “Switching control system based on largest of maximum (LOM) defuzzification–theory and application,” *Fuzzy Logic–Controls, Concepts, Theories and Applications, InTech, Rijeka*, pp. 301–324, 2012.

REFERENCES

- [69] “Fuzzy sets and pattern recognition,” 2004, retrieved March 24, 2014, from <http://www.cs.princeton.edu/courses/archive/fall07/cos436/HIDDEN/Knapp/fuzzy004.htm>.
- [70] S. W. Smith, *The scientist and engineer’s guide to digital signal processing*. California Technical Pub. San Diego, 1997.
- [71] A. Serrani and G. Conte, “Robust nonlinear motion control for AUVs,” *Robotics & Automation Magazine, IEEE*, vol. 6, no. 2, pp. 33–38, 1999.